sous le n° d'ordre NNT : 2021LYSEC04

THESE

pour obtenir le grade de
DOCTEUR DE L'ECOLE CENTRALE DE LYON
Spécialisté: Informatique

dans le cadre de l'Ecole Doctorale InfoMaths

Human Skin Characterization and Analysis based on Hyperspectral Reflectance using Machine Learning

présentée par
Shiwei LI
3 février 2021

Directeur de thèse: DR.Mohsen ARDABILIAN École Centrale de Lyon
Directeur de thèse: Liming CHEN École Centrale de Lyon
Co-directeur de thèse: Abdelmalek ZINE École Centrale de Lyon

Prof. Fabrice Meriaudeau	Université de Bourgogne - ImViA	Président
Prof. Alice Caplier	Grenoble-INP-GIPSA Lab	Rapporteur
Dr. HDR Sylvie Treuillet	Université d'Orléans - PRISME	Rapporteur
Prof. Peter Sturm	Inria Grenoble - Lab.J.Kuntzmann	Examinateur
Dr. Mohsen Ardabilian	École Centrale de Lyon - LIRIS	Directeur de thèse
Prof. Liming Chen	École Centrale de Lyon - LIRIS	Directeur de thèse
Dr. HDR Abdelmalek Zine	École Centrale de Lyon - ICJ	Co-directeur de thèse

Abstract

Skin, the largest and multi-functional organ of human body, has always been an important research object in many fields, such as cosmetics and computer graphics. Its appearance especially color can reflect certain diseases, such as melanoma and vitiligo, which has been widely investigated. In the past, we obtain the skin physiological information by biopsy. This method is usually invasive and takes long time. Recently, the inner information can be derived non-invasively benefiting from skin hyperspectral diffuse reflectance. However, it is still a challenging task since the accuracy and the efficiency can not be ensured at the same time in applications. For example, the gold standard Monte Carlo method gives favorable estimations but costs much time. This thesis aims to build a detailed skin model and apply it for faster non-invasive determination of skin components. Moreover, an auxiliary method based on this model can identify the presentation attacks at high precision.

Our skin model is composed of three sub-layers: the epidermis, the dermis and the subcutis. We first implement a GPU-based Monte Carlo method to reconstruct a skin diffuse reflectance database based on our skin model. The wavelength is randomly taken in the visible light range from 450 to 700 nm. Then, this database is used for training a forward artificial neural network to map optical parameters calculated from our skin model and skin diffuse reflectance. We compare the skin diffuse reflectance reconstructing capacity of forward network and Monte Carlo method, and find that they match well each other. It takes 19 ms for the forward network to reconstruct a reflectance spectrum for 450 to 700 nm with 1 nm interval. However, it takes 337 s for Monte Carlo method. Besides this, we analyze the impact of each skin parameters on reconstructed reflectance and then apply this forward network combined with a curve-fitting algorithm to extract skin parameters using NIST skin database. The results show that the forward network has acceptable accuracy for melanin, blood and oxygen saturation without limitations to fix the thickness of skin sub-layers. And the forward network method costs an average of 17 seconds to finish the extraction process. An inverse network, random forest and support

vector regression are also studied. As shown in previous research, inverse networks have large errors in extracting skin parameters but at extremely high speed. In our research, we generate a skin diffuse reflectance database using proposed forward network instead of Monte Carlo method to reduce time cost. Two types of dimensionality reduction methods: low variance filter and principal component analysis are applied for further speeding up. The experiments show that the inverse network works better in extracting melanin content than random forest and support vector regression and has similar results to inverse Monte Carlo. Moreover, it only takes around 10 min to train the inverse network after having used dimensionality reduction methods and 12 ms to extract melanin content for one spectrum.

As for the presentation attacks detection, we use two metrics RMSE and STD of fitting performance to classify if the object diffuse reflectance belongs to skin. By selecting the appropriate wavelength range, it has promising classification results. The vulnerability of face recognition system has been discussed a lot while detecting presentation attacks, especially the silicon face masks. Our method uses hyperpspectral reflectance to identify the non-skin objects because the absorption coefficients of several skin pigments are unique. We will collect more hyperspectral skin images and generalize our method for practical applications.

Résumé

La peau, organe le plus large et multifonctionnel du corps humain, a toujours fait l'objet d'importante recherche dans de nombreux domaines, tels que les cosmétiques et l'infographie. Son aspect et en particulier sa couleur peut indiquer certaines pathologies, comme le mélanome et le vitiligo qui ont été largement étudiées. Jusqu'à présent les informations physiologiques cutanées étaient uniquement obtenues par la biopsie. Cette méthode généralement invasive qui est loin d'être instantanée. Récemment, cette caractérisation peut être faite de manière non invasive à partir de la réflectance diffuse hyperspectrale de la peau. Néanmoins, la difficulté reste toujours d'allier la précision et la complexité temporelle dans les applications. Par exemple la méthode de référence, Monte Carlo, qui donne des estimations précises coûte cher en temps de calcul. Cette thèse vise à construire un modèle détaillé de peau et à l'appliquer pour une estimation non invasive et plus rapide de ses constituants. En outre, une méthode auxiliaire basée sur ce modèle permet d'identifier les attaques de présentation avec une grande précision. Notre modèle de peau est composé de trois sous-couches : l'épiderme, le derme et l'hypoderme. Nous avons d'abord implanté une méthode de Monte Carlo basée GPU pour reconstruire un corpus de données de réflectance diffuse de la peau à partir de notre modèle de peau. La longueur d'onde est prise au hasard dans la gamme de lumière visible de 450 à 700 nm. Ensuite, ces données sont utilisées pour entraîner un réseau de neurones artificiels afin de correspondre aux paramètres optiques calculés à partir de notre modèle de peau la réflectance diffuse de la peau. La comparaison des performances montre que les deux approches, la nôtre et la méthode Monte Carlo, donnent des résultats très voisins. En outre, il faut seulement 19 ms à notre réseau pour reconstruire un spectre de réflectance de 450 à 700 nm avec un intervalle de 1 nm. Alors qu'il faut 337 s pour la méthode Monte Carlo. Nous avons aussi analysé l'impact de chaque paramètre de peau sur la réflectance reconstruite, puis avons appliqué ce réseau, combiné à un algorithme d'ajustement de courbe, pour extraire les paramètres de la peau à l'aide de la base de données NIST. Les résultats mon-

trent que notre approche a une précision acceptable pour la saturation en mélanine, en sang et en oxygène sans limitation d'épaisseur des sous-couches cutanées. Le coût moyen de notre méthode d'extraction est de 17 secondes. Aussi, un réseau de neurones, une forêt aléatoire et une machine à vecteurs de support pour la régression sont également étudiés. Les réseaux neuronaux utilisés dans une configuration inversée produisent de grandes erreurs dans l'extraction des paramètres de la peau mais à une vitesse extrêmement élevée. Dans notre recherche, nous générons une base de données de réflectance diffuse de la peau en utilisant le réseau direct proposé au lieu de la méthode de Monte Carlo pour réduire le coût en temps. Deux types de méthodes de réduction de dimensionnalité : un filtre à faible variance et une analyse en composantes principales sont appliqués pour l'accélérer davantage. Les expériences montrent qu'en extraction de la teneur en mélanine, ce réseau surclasse la forêt aléatoire et la machine à vecteurs de support pour la régression, mais obtient des résultats similaires à ceux de la méthode Monte Carlo. De plus, une dizaine de minutes suffisent pour former le réseau inverse, après avoir utilisé des méthodes de réduction de dimensionnalité et 12 ms pour extraire la teneur en mélanine pour un spectre donné. Finalement, quant à la détection des attaques de présentation en reconnaissance faciale, nous utilisons deux métriques, RMSE et STD, l'ajustement de courbe de réflectance et notre réseau neuronal Skin-Net pour décider si la réflectance diffuse enregistrée appartient à la peau. Des résultats de classification prometteurs sont obtenus en sélectionnant la gamme de longueurs d'onde appropriée. La vulnérabilité des systèmes de reconnaissance faciale face à l'évolution des attaques de présentation, en particulier les masques en silicone, a suscité un vif intérêt au cours de la dernière décennie. Notre approche qui utilise la spécificité des pigmentations cutanées et de leurs coefficients d'absorption pour identifier les objets non cutanés à partir de leur réflectance s'inscrit dans ce contexte. Une généralisation de notre approche visant des applications pratiques s'appuiera sur une collection plus large d'images hyperspectrales de peau.

Acknowledgements

Contents

List of Figures

List of Tables

Introduction

Contents

1.1   Research Topic

Skin, the soft layer that covers vertebrates, is the largest and multi-functional organ in the human body. The skin blocks external intrusions and retains moisture. It acts mainly as a protective barrier for keeping warm, blocking, feeling etc. Moreover, skin appearance is also a concern in people's daily life. Research on skin modeling is inevitable and important. In the past, the Fitzpatrick scale was developed based on skin color to evaluate the response of different skin types to the ultraviolet ray (UV)[1]. Then, it has been developed and extended to include more skin types[2]. Until now, it is still widely used as a numerical classification schema for skin color. There are 6 types in this schema. The formation of skin color is predominantly influenced by skin pigments, such as melanin, hemoglobin etc. And skin color is the comprehensive result of multiple pigments. The volume fraction of melanin is influenced by the sunlight intensity and human body's own regulation. In an area where sunlight is strong, human skin produces a large amount of melanin to resist UV damage. This may also lead to skin cancers, such as melanoma. And in an area where sunlight is weak, the volume fraction of melanin tends to decrease. Besides, there are two indispensable nutrients for human body: vitamin D and vitamin B9. Vitamin D is the key to the formation and maintenance of bones and vitamin B9

is an important catalyst involved in DNA replication. The synthesis of vitamin D requires UV, however, vitamin B9 is broken down by UV. Hence, human body attempts to find a balance for maintaining normal operation of these two nutrients. This is a result of long-term evolution for adapting the local environment. And that's why humans with the same origin[3] have formed different skin color for different ethnicity.

In cosmetics, people use sunscreen lotions to prevent the skin from overexposing to the sun, apply concealer on the skin to hide spots, and use cleanser to clean skin surface debris. In biomedicine, many skin diseases are researched to find causes and abnormalities. In computer graphics, rendering more realistic skin in games is the ultimate goal. In recent years, face recognition has developed very well and rapidly. Many applications based on face recognition come out. Mobile payment using faces is a well-known example. The security of mobile payment is one of the most important issues so far. With the development of presentation attacks, it's hard to identify which is the authorized user. The vulnerability to presentation attacks limits the implementation of face recognition systems. All kinds of problems make skin characterization and analysis more important.

So far various methods have been put forward to analyze skin appearance in different kinds of color spaces, such as RGB, CIE1931XYZ, YUV etc. In computer graphics, RGB color space is very convenient because the principle of RGB color space is similar to that of the human visual system. Three channels: Red, Green and Blue are included. However, this is not precise since the wavelength of light usually differs in a large range. The intensity of light with different wavelengths are combined in different proportions and finally expressed in R,G,B channels. This process may lose some important spectral information. Benefiting from the birth of hyperspectral sensors, we can now collect spectral signatures in high resolution. In our research, the hyperspectral diffuse reflectance of human skin is the main subject to analyze. Figure.1.1 shows a hyperspectral skin image, and each pixel contains spectral signatures in the visible light range. It can be considered that hyperspectral image uses more channels than RGB, and gives more details since the information of each wavelength is displayed. The absorption and scattering coefficients of skin

depend on the wavelength and are decided under the effects of many pigments. Moreover, the absorption coefficient of various pigments are also different from each other. This is the key to quantitatively and non-invasively analyze skin components. Generally, if we want to know the volume fraction of blood or other components in skin, we have to apply the biopsy method. It takes long time and is invasive. Based on hyperspectral skin image, we can obtain directly the information of skin components with low cost. Although the biopsy method is usually more accurate, this non-invasive method can quickly obtain volume fractions of melanin and the like with acceptable accuracy. There existed a good deal of research on this direction and various methods have been applied to explain the relation between hyperspectral diffuse reflectance spectra and skin components. Classical methods are Monte Carlo simulation, diffusion approximation, Kubelka-Munk theory, etc.[4, 5, 6]. However, they are plagued by calculation time, accuracy or limitations. Recently, machine learning and deep learning methods have been used and achieved good results, but they were trained and tested in a small database, which may lead to over-fitting[7].
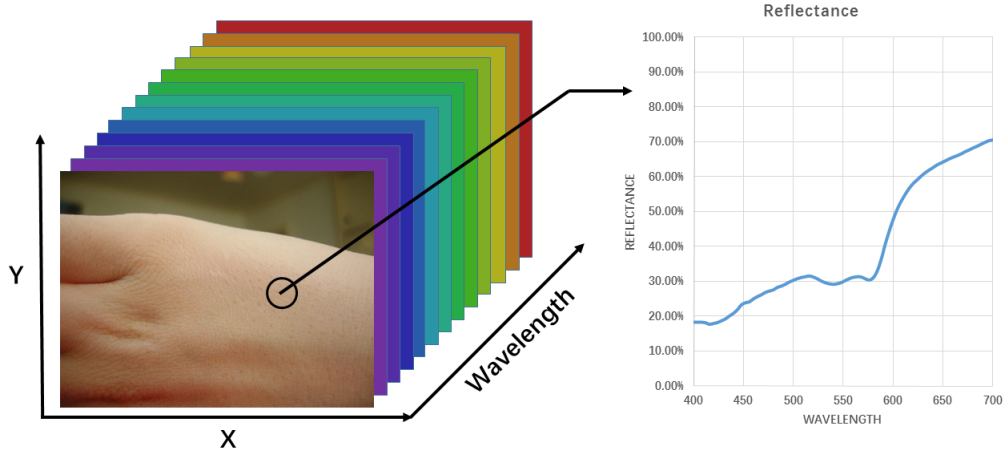
Figure 1.1: Hyperspectral skin image in the visible light range

In this thesis, we have built skin models from the perspective of bio-optics to characterize and analyze skin. In proposed skin models, we have defined the volume

fractions of pigments, the refractive index, the anisotropy factors and the thickness for skin sub-layers. Then, a quantitative analysis of skin is studied for reconstructing the hyperspectral skin diffuse reflectance and extracting the inner information from the measured skin diffuse reflectance. Moreover, a fast determination method of melanin content has been proposed with acceptable accuracy. And we also studied on skin and non-skin classification as an auxiliary method for presentation attacks detection based on proposed skin model.

1.2 Organization of the thesis

The rest of this thesis is organized as follows:

In Chapter 2, we first introduce the structure of the skin from an anatomical perspective since our research involves the cross-field of both biology and informatics. Moreover, we elaborate the interaction between light and skin and present several state-of-the-art theories which describe this interaction and give analytical or numerical solutions. Lastly, a brief introduction to hyperspectral imaging techniques is given.

In Chapter 3, we elaborate a quantitative skin analysis based on diffuse reflectance. Two detailed skin modes which contain the volume fraction of several pigments and other physiological skin parameters are proposed and analyzed. Feed forward neural networks are applied to finish the regression task between skin models and skin diffuse reflectance. The performances of reconstructing reflectance spectra and extracting physiological skin parameters are evaluated separately.

In Chapter 4, a fast determination of melanin content based on diffuse reflectance is introduced. A large diffuse reflectance database is generated by forward networks based on three-layered skin model to avoid over-fitting. Inverse networks, random forest and support vector regression are then trained to map the reflectance and melanin content. Low variance filter and principal components analysis are used for speeding up the training time.

In Chapter 5, we present an auxiliary method for presentation attacks detection based on proposed skin model and hyperspectral reflectance. We generate a network

which fits well skin reflectance and use the values of RMSE and STD to identify if each pixel in the image is skin or non-skin.

In Chapter 6, we draw conclusions and propose some perspectives for future research directions and improvements.

Background

Contents

In this chapter, we present the biological structure of human skin, the computational models that describe the interaction between light and human skin, and hyperspectral techniques. Human skin is a complex multi-layered translucent tissue from the biological point of view and clearly it is the largest organ that covers almost all parts outside human body. The surface area of the skin on an average adult is about 1.8 m^2 and counts 16% of the total body weight[8]. Skin could provide a barrier against the damage from the environment, such as bacteria, injuries, heat and light. At the same time, it helps us to avoid water loss, regulate the temperature inside body, perceive the environment and produce vitamin D[9, 10]. Skin appearance which means the color, the thickness and the texture, varies not only over the individuals but also over the body positions. For example, the skin around the eyelids is the thinnest, about 0.5 mm thick, compared with other parts. The

skin of palms and soles is the thickest, about $4\ mm$ thick. Generally speaking, body parts that are frequently used and subjected to a large amount of friction become thick and hairless.

On the other hand, the inner components of the skin dominate the appearance, especially the color. The biological pigmentations deposited inside the skin show different absorption spectra, which means light is absorbed in different proportions. The skin is commonly considered as homogeneous multi-layers when simulating the light propagation. The two main events related are the absorption event and the scattering event. The absorption event describes a light energy loss. The two biological pigmentations that dominate the absorption within the visible light region in skin are hemoglobin and melanin. The latter pigmentation involves the diagnosis of melanoma, which is a common skin cancer. The scattering event describes a deflection in light direction, such as reflection and refraction. It is mainly attributed to an interaction with small particles or structures due to the Mie scattering or the Rayleigh scattering[11]. Collagen fibres and other filamentous proteins play an important role in the scattering event[12]. Besides this, the scattering events mainly point in forward direction, in other words, light that can return to the surface undergoes a large amount of scattering events.

In the following sections, we present firstly the details of skin sub-layers, and then the two types of light events: the absorption and the scattering. Next the mainstream methods (state of the art) to explain or describe the interaction between light and skin are introduced. And then the acquisition of reflectance spectra using hyperspectral techniques is presented. Lastly, we summarize this chapter by evaluating the performances of the existing methods.

2.1 Skin Anatomy

Skin is the largest and multifunctional organ which is composed of several sub-layers as we mentioned above. It arises by the combination of three elements: the prospective epidermis, the prospective mesoderm, and the neural crest[13]. These three elements then develop into the diverse components of skin over ages. Compared

with other mammalian lines, human skin has similar anatomical, physiological, optical and immunological properties. The pigmentations, such as melanin provided by melanocytes, play an main role in the formation of skin appearance. The ultraviolet radiation (UV) in sunlight is partially absorbed by melanin, which could protect us from the UV damage. And people who lack melanin suffer high possibility of skin cancer. One of these skin cancers particularly caused by UV is malignant melanoma, which spreads quickly and can be deadly. This leads to the urgent demand for detecting the volume fraction of pigmentations. As shown in figure.2.1, we can see the detailed components for both hairy and non-hairy skin. Basically, skin is comprised of three layers: the epidermis, the dermis and the subcutis also called the hypodermis. And there are many specialized cells inside skin, such as basket cells, Langerhans cells, melanocytes, and Merkel cells. The epidermis is the outermost layer that contains the melanocytes. This layer is the main research object related to melanoma. The dermis is under and adjacent to the epidermis. Plenty of blood vessels, which contain the another important pigmentation: hemoglobin, deposit in this layer. These two layers cover the third fatty layer: the subcutis.

The description for three layers will be given in the following sections to provide a further understanding in terms of optical viewpoint.

2.1.1 Epidermis

As the outermost layer of skin, the epidermis forms a barrier against microbial pathogens. It can be divided into 5 sub-layers: stratum corneum, stratum lucidum, stratum granulosum, stratum spinosum, and stratum basale, as illustrated in figure.2.2. Upon the base layer (stratum basale), there are a large amount of flatten cells. The primary cell, accounting for 95% of the total, is the keratinocyte. It moves gradually towards the skin surface from the base layer, and then forms other sub-layers. This base layer consists of columnar cells arranged perpendicularly and generally is only one cell thick. Merkel cells, which are highly relative to nerves, are found in the stratum basale. The stratum corneum serves dominantly for holding water, which is significant for maintaining healthy skin. The stratum lucidum only appears on the palms and soles, which is also known as the cause of thick skin.
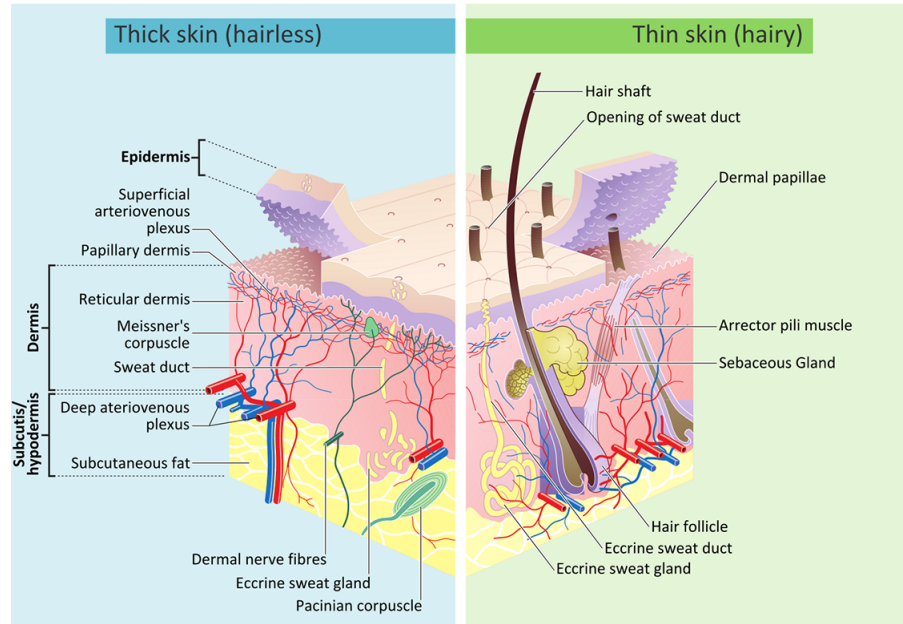
Figure 2.1: Detailed cross section of skin biological structure: Right is for hairless skin; Left is for hairy skin. (image from Wikipedia: Human skin)

In the stratum granulosum, keratinocytes become larger, dehydrated, and finally inactive. This morph leads to a tough sub-layer. Cells in stratum spinosum enlarge and are reshaped to polygons. The thickness of the epidermis is generally ranged from 0.027-0.15 mm[14].

Skin appearance is mainly expressed according to the epidermis due to the fact that it is the outermost layer of skin and melanin is mostly located in the stratum basale. As skin color is decided by a combination of the absorption of biological pigments in the visible light range, melanin is the most important absorber and it can dissipate most of absorbed ultraviolet radiation. By exposure to ultraviolet radiation, melanin is generated to protect us from the radiation damage. However, it comes with an increased risk of malignant melanoma, which is highly lethal. As of 2015, there were in total 3 million cases with melanoma all over the world, and almost 59,800 deaths[15, 16]. This leads to the growing demand for quantitative determination of melanin volume fraction.
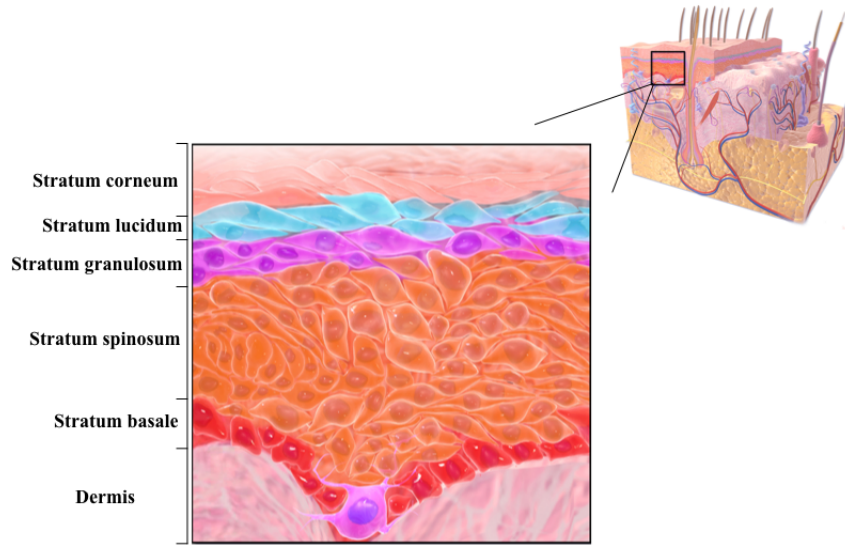
Figure 2.2: Cross section of the epidermis: stratum corneum, stratum lucidum, stratum granulosum, stratum spinosum, and stratum basale from top to bottom. (image from Wikipedia: Epidermis)

2.1.2   Dermis

The dermis is beneath the epidermis, which is primarily composed of dense irregular connective tissue and is usually the thickest of the three layers (0.6-3 mm)[14, 17]. It contains large amounts of collagen fibers and vessels. Additionally, the dermis can be divided into two sub-layers: the papillary and the reticular dermis. As we can see from figure.2.3, the papillary dermis is adjacent to the overlying epidermis and it interdigitates with the base of the epidermis through a basement membrane and supports the epidermis metabolically and mechanically and it can nourish the epidermis. The reticular dermis is the lower part of the dermis and is generally thicker than the papillary dermis. The collagen fibers within the reticular dermis is oriented and called Langer's lines, which are relevant to surgery and wound healing[18].

As we mentioned above, the epidermis provides us a barrier against pathogens in vitro, helps us regulate water level released in vivo and is the main factor to form skin appearance. The dermis also has its unique functions. It contains both mechanoreceptors and thermoreceptors that help us to perceive the outer world by the sense of touch and heat. In addition, the large amounts of collagen fibers
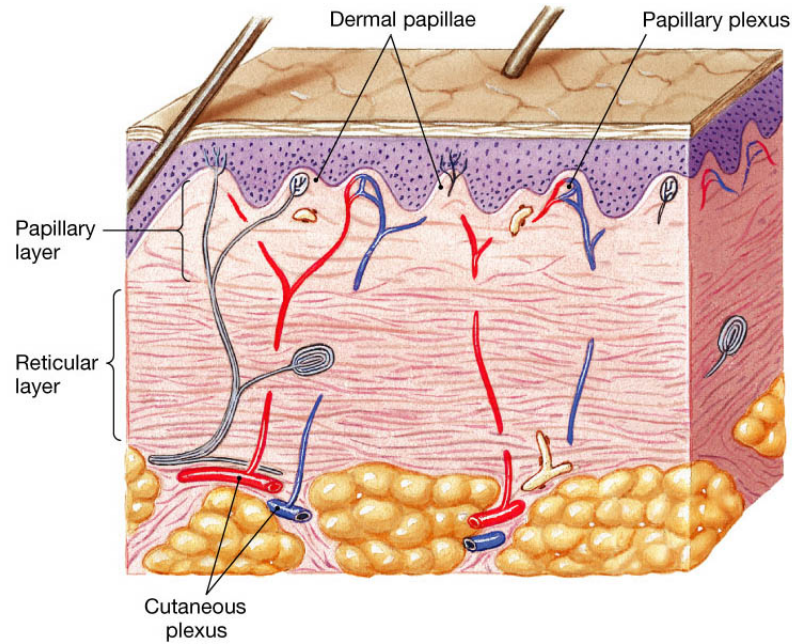
Figure 2.3: Structure of the dermis (image from Integumentary System)

within the dermis are highly related to our ages. With the skin aging, it comes with the loss of skin flexibility, laxity and wrinkles at the same time due to the loss of collagen fibers. This may also lead that the skin is more vulnerable to be damaged[19]. Moreover, the fingerprints are caused by the dermal papillae within the papillary dermis. The ridges they produce in hands and feet can remain substantially unaltered throughout life and hence the fingerprints are widely used in personal identification for security systems[20].

Additionally, another important biological pigments located in the dermis is hemoglobin. As we know, the dermis is rich in blood vessels. Hemoglobin has an unique absorption spectra from 500 to 600 nm, which is also called "W" pattern[21]. It's also the reason why human skin looks reddish and yellowish. We will discuss this in detail in later chapter.

2.1.3   Subcutis

The subcutis (also called subcutaneous tissue, hypodermis or superficial fascia) is the innermost layer of human skin[22]. The main types of cells deposited in the subcutis

are fibroblasts, adipose cells, and macrophages. The thickness of the subcutis varies throughout the body and individuals, which is from 1.65 to 14.65 mm in males, whereas it is from 3.3 to 18.2 mm in females in Indian[23]. This layer serves to support dense vessels and nerves network in the tissue, absorb and reduce shock, and protect underlying tissues from external temperature[24]. Subcutaneous fat is the main layer of the subcutis that is widely distributed within human body. It functions as padding and as energy store[25]. Most of the fat involved in that people try to control weight is located here. Another significant usage of the subcutis is subcutaneous injection because a limited blood network locates here and medications injected will be absorbed gradually. The ideal injection sites are: the outer part of the upper arm, the middle part of the abdomen, the front of the thigh, the upper back and the upper part of the buttocks[26].

2.2   Interaction between Light and Skin Tissue

In this section, we start with some fundamental optics concepts. Then, state-of-the-art approaches, which explain the relationship between light and skin, are introduced. So far, the most widely used method, which is also considered as the gold in this domain is Monte Carlo simulations. A large amount of research validates their approaches compared with Monte Carlo simulations. Other approaches like Diffusion Approximation, Kubelka-Munk theory etc. are also used very frequently. And in computer graphics domain, there are another two approaches called Bidirectional Reflectance Distribution Function (BRDF) and Bidirectional Subsurface Scattering Reflectance Distribution Function (BSSRDF), which are mainly used to calculate the results of light effects. To introduce and understand these approaches, we firstly need to figure out the main two light propagation events (the absorption and scattering) and the optical properties of human skin.

Light is a form of energy, which is expressed as electromagnetic radiation. That is to say, not only the visible light but also microwaves, ultraviolet-rays, infrared-rays etc. are included. Generally, light is divided based on the wavelength, λ (measured in nanometers[nm] in our research). Figure.2.4 illustrates the visible light spectrum.

The spectral range of visible light is not strictly limited because it varies among individuals[27]. Several researches has defined various visible light range from 420-680 nm to 380-800 nm[28, 29, 30, 31]. The sunlight was firstly discovered to be split by a prism into several colors by Isaac Newton. Then, some behavior of light was considered like waves and the classical electromagnetic theory was published by Maxwell. However, some other behavior of light was found like particles. This wave-particle duality was then put forward and based on previous research results, Einstein postulated that the energy of light can be quantized as photons[32]. This concept of photons is the basis of geometrical optics[33], which involves the study of the properties of light particles. In this domain, the large-scale behavior of light, such as reflection and transmission, is described by assuming that light is composed of non-interactive rays, each of which carries a certain amount of energy[14]. Then the radiative transfer theory was established by combining principles of geometrical optics and thermodynamics. This theory aims to explain and characterize how the radiation propagates.

Figure 2.4: Visible light spectrum: V (violet), B (blue), G (green), Y (yellow), O (orange), R (red) (image from Wikipedia: Light)

2.2.1   Absorption

When light propagates in vacuum, there is no doubt that no interactions with particles happen. However, when light propagates in human skin, there is a series of complicated interactions with particles. The absorption is the main event during light propagation in skin.

The absorption can be considered as how the electrons (subatomic particle) bound in the atoms take up the energy of photons. From the perspective of micro physics, the atoms and molecules make up matter contain electrons. These electrons

14

act like wave or have a tendency to vibrate at specific frequencies, which can be described by an atomic orbital. Each orbital has its unique state such as energy, and these orbitals are discrete. Electrons can also be transferred from one orbital to another orbital by emitting or absorbing photons with energy matching the potential difference. When light with the same specific frequencies enters into medium, these electrons will absorb the energy of light and jump from ground state to excited state. This is why different matter has its own selective absorption of light. Moreover, these electrons at excited state are unstable and will interact with neighboring atoms. As results, they decay back to ground state and the vibrational energy is converted to the thermal energy.

Figure.2.5 describes how the selective absorption happens. From beam source, an incident light is emitted towards a sample. This incident light contains several lights with different wavelengths (noted here six different colors), and only green part of light matches the potential difference between two orbitals which excites electrons to a higher state. Finally, the outgoing light detected shows a decrease in the green part of light as we can see from spectra.
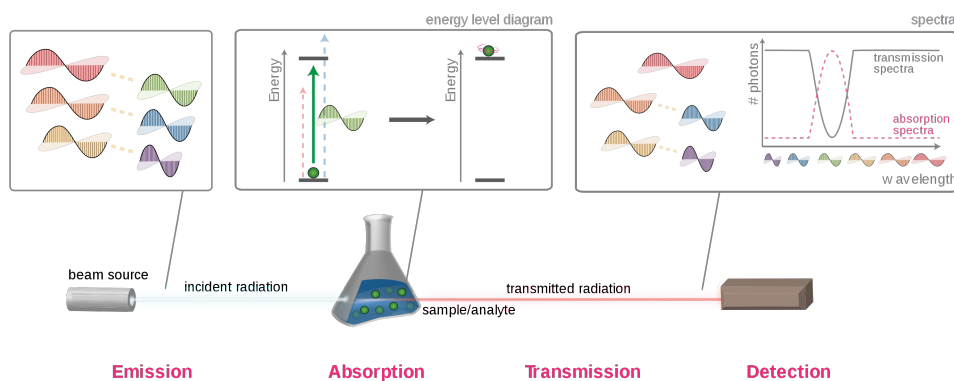
Figure 2.5: An overview of selective absorption (image from Wikipedia: Absorption)

To quantify this absorption capacity of matter, the Beer-Lambert law (also called the Beer-Lambert-Bouguer law) is discovered. Pierre Bouguer and Johann Heinrich Lambert clarified the relationship between the absorption of light and the thickness of the absorbing substances in 1729 and 1760 respectively[34, 35]. In 1852, August Beer proposed that the absorption of light and the concentration of the absorbing

substances also have a similar relationship[36]. Combining the two laws, the Beer-Lambert law is derived as below:

$$A = -\log_{10} \frac{I_t}{I_0} = Klc = l \sum_{i=1}^{N} K_i c_i \tag{2.1}$$

where A is the absorbance and equals to the negative common logarithm of the ratio of transmitted light intensity to incident light; I_t and I_0 are the intensity of transmitted light and incident light respectively; K is the molar attenuation coefficient (also known as the molar extinction coefficient and molar absorptivity); l is the thickness of medium; c is the concentration of the absorbing substance; When it comes to N absorbing substances, the overall absorbance is the sum of absorbances for N substances.

2.2.2   Scattering

When passing through an medium, light or other forms of radiation have to change or deviate from their linear trajectory due to the effect of localized inhomogeneity. This physical phenomenon is called scattering. The scattering can be divided into three types according to a dimensionless size parameter α, which is defined as:

$$\alpha = \frac{2\pi r}{\lambda} \tag{2.2}$$

where $2\pi r$ is the circumference of particles; λ is the wavelength of incident light.

When $\alpha \ll 1$, it's Rayleigh scattering. It was first discovered and refined by Lord Rayleigh[37, 38]. Note that the upper limit of α is $1/10$, which means the size of particles need to be much smaller than the wavelength of light. The intensity I_s of light scattered by particles with diameter d and refractive index n is defined by[39]:

$$I_s = I_0 \frac{1 + \cos^2 \theta}{2R^2} (\frac{2\pi}{\lambda})^4 (\frac{n^2 - 1}{n^2 + 2})^2 (\frac{d}{2})^6 \tag{2.3}$$

where I_0 is the intensity of incident light at wavelength λ; θ is the angle scattered and R is the distance to particles. Rayleigh scattering is first used to explain why the sky is blue. When sunlight passes through the atmosphere, Rayleigh scattering occurs

with air molecules whose radius is much smaller than the wavelength of visible light. Blue light has a shorter wavelength than red light, in this case, Rayleigh scattering happens more intensely for blue light. Consequently, the scattered blue light covers the sky, making the sky blue.

When $\alpha \approx 1$, it's Mie scattering. The size of particles is close to or greater than the wavelength of light. Figure.2.6 shows the difference between Rayleigh scattering and Mie scattering. Most of light is scattered forward for Mie scattering, whereas light is scattered both forward and backward for Rayleigh scattering since cosine is an even function. It's much more complicated to quantify Mie scattering and generally we use the spherical functions to approximate solutions. The scattering efficiency can be calculated with amplitudes of the scattered field a_j and b_j (can be approximately considered as electric and magnetic fields) given by[40, 41]:

$$\begin{cases} a_j = \frac{m^2 \psi_j{}'(mx)[x\psi_j(x)]' - \psi_j(x)[mx\psi_j(mx)]'}{m^2 \psi_j(mx)[x\xi_j(x)]' - \xi_j(x)[mx\psi_j(mx)]'} \\ b_j = \frac{\psi_j{}'(mx)[x\psi_j(x)]' - \psi_j(x)[mx\psi_j(mx)]'}{\psi_j(mx)[x\xi_j(x)]' - \xi_j(x)[mx\psi_j(mx)]'} \end{cases} \tag{2.4}$$

where j is integer that spans the range 1,2,...; m is the relative refractive index of particles to surrounding medium; $x = ka$, the size parameter with k the wave number of light and a the radius of particles; ψ_j and ξ_j are the spherical Bessel functions.
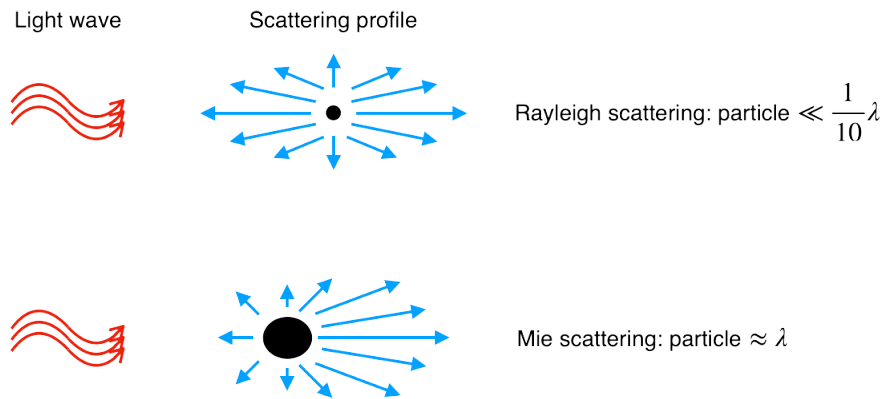
Figure 2.6: Comparison of the scattering profile for Rayleigh scattering and Mie scattering

When $\alpha \gg 1$, it's geometric scattering. The size of particles is usually 10 times

larger than the wavelength of light. In this case, the laws of geometric optics are satisfied enough to explain the interactions between light and particles.

Inside human skin, there are various compositions with different absorption and scattering profiles. In the following section, we will focus on presenting the optical properties of human skin and give a brief summary for several important compositions chosen for skin modeling.

2.2.3 Optical Properties of Human Skin

Talking about the optical properties of human skin, we first have to mention light effects on skin. One of the most important effects is the photoaging, which describes the characteristic changes to skin caused by ultraviolet. Skin aging can be categorized in two types: endogenous aging led by genes and exogenous aging. Among exogenous aging, photoaging is the most powerful and ubiquitous, which counts 90% of skin aging. Figure.2.7 is a photo published in The NEW ENGLAND JOURNAL of MEDICINE in 2012[42]. During the journey, the sunlight passed through the window and shone on the driver's left face for many years, causing his left face is visibly more photodamaged than his right face. This is an example of skin aging caused by ultraviolet. Depending on different wavelengths, ultraviolet can be divided into three groups: UVA (315-400 nm), UVB (280-315 nm) and UVC (100-280 nm)[43].

UVA, UVB and UVC all damage collagen. Both UVA and UVB also destroy the skin's vitamin A[44]. As we can see from figure.2.8, UVC with the shortest wavelength and the worst penetration among three types has been filtered out in the ozone layer. Only less than 5% of UVC can reach the earth surface. UVB with the middle penetration can reach the epidermis and dermal papilla of human skin, however, most of it has been blocked by glass or debris in skin surface. It can induce the skin to produce vitamin D, while at the same time it can cause the direct damage to the cutaneous cells including the DNA of keratinocytes. Long-term exposure to UVB may cause sunburn and skin redness, swelling, heat and pain. In severe cases, blisters or peeling may occur. UVA with the longest wavelength can reach the dermis. Compared to UVB, the damage caused by UVA is silent, slow but

Figure 2.7: The face of a 69-year-old truck driver who has spent almost three decades on the road. The left of his face has been exposed to sunlight.

serious. UVA can cause the production of reactive oxide species (ROS), destroy the oxidation-antioxidant balance, cause DNA damage and even necrosis of skin cells, and destroy collagen fibers and elastic fibers, causing skin darkening, dullness, and wrinkles.
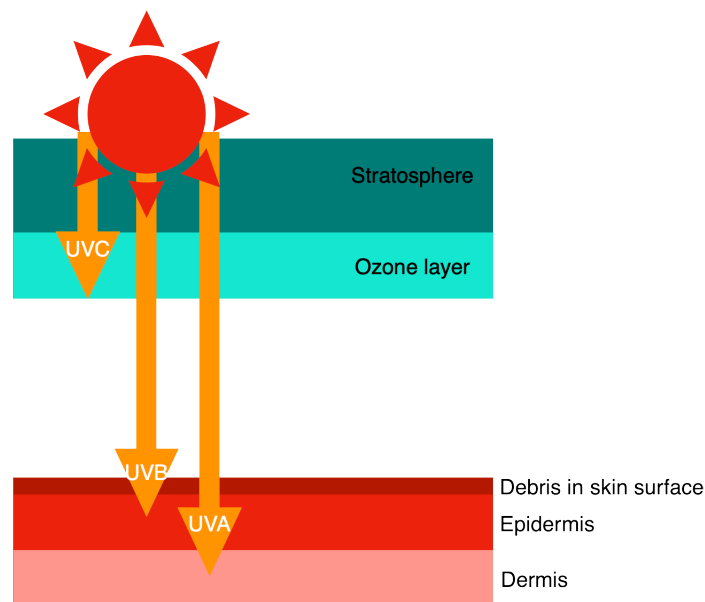
Figure 2.8: Penetration of three types ultraviolet.

Besides ultraviolet, recent research has proved that infrared in sunlight can also

lead to photoaging and denaturation of fibers[45]. We have talked about light effects on skin above, then we will introduce the optical properties of skin for skin modeling.

As we mentioned above, the main events that describes the interaction between light and skin are the absorption and scattering. In our research, we use the absorption coefficient μ_a and the scattering coefficient μ_s to quantify these two events. First, we must make clear the absorbers in human skin to calculate the absorption. Several pigments that dominate the absorption are tabulated as below:

- **Melanin** is the most important pigments or absorbers in human skin. There are two types: eumelanin and pheomelanin, which have different absorption spectra. And that is why eumelanin looks black and pheomelanin looks red-brown. Melanin is mainly located in the basal layer in the epidermis. Most of ultraviolet is absorbed by melanin, while long-term exposure to ultraviolet causes an increase of melanin content, which may result in skin cancer. Melanin is highly related to melanomas and 92% of melanomas have genetic mutations caused by ultraviolet.

- **Hemoglobin** also counts for the absorption. It exists in blood and can be divided into two main types as well depending on if it is oxygenated. The two main types occupy over 95% of hemoglobin. Because of the unique absorption spectrum of oxy-hemoglobin, it's usually studied and analyzed to recognize skin from other materials. And the oxygen saturation varies in veins and in arteries.

- **β-carotene** belongs to natural chemicals. This pigment cannot be synthesized inside human body but can be acquired from fruits and vegetables, such as carrots, spinach, lettuce, potatoes, broccoli and cantaloupe. It makes plants look orange and yellow. It exists both in the epidermis and blood in the dermis. It can be converted into vitamin A after entering human body, and its conversion process is adjustable.

- **Bilirubin** exists in blood in the dermis. It is toxic and can cause irreversible damage to the brain and nervous system. The high level of bilirubin in blood

may cause diseases like jaundice, which makes the skin and other tissues yellowish. This often happens in newborns. And it also indicates if liver is healthy or not.

- **Fat** exists mainly in the subcutaneous tissue. It has less absorption than melanin and hemoglobin. It's also an important component of living organisms. Fat is the energy provider of living organisms. More important, it's closely related to cell recognition, species specificity, and tissue immunity.

The above pigments affect the absorption for light in human skin and together contribute to skin color. Moreover, water is also an important absorber. However, compared to the above pigments, the absorption capacity of water in visible light range is too weak. Given that water takes up a big part of human skin, we still take water into consideration when calculating the absorption. Another component, which need to be counted, is called the absorption of skin baseline. It is the absorption due to the remaining dry depigmented tissues, generally considered as collagen fibers.

The scattering of human skin is caused by the structure of collagen fibers. There are two types of scattering that undergo inside human skin: Rayleigh scattering and Mie scattering, as we mentioned above. Since the size of the structure of collagen fibers varies from micro to macro, both two types of scattering exist. If the radiation is only scattered by a local scatterer, it is called single scattering. If many scatterers are gathered together, the radiation may be scattered many times, which is called multiple scattering. Single scattering can be regarded to be random, however, multiple scattering is usually more deterministic. There exists many researches that study on the continuum scattering theory in tissues and adjust descriptions to match experimental data[46, 47, 48, 49].

Other optical properties of human skin, which need to be taken into account, are refractive index and anisotropy factor. Refractive index can be regarded as the factor that reduces the speed and wavelength of radiation relative to their vacuum value. And anisotropy factor reflects the distribution of the deflection angle for multiple scattering. To summarize, we introduce light effects on skin especially
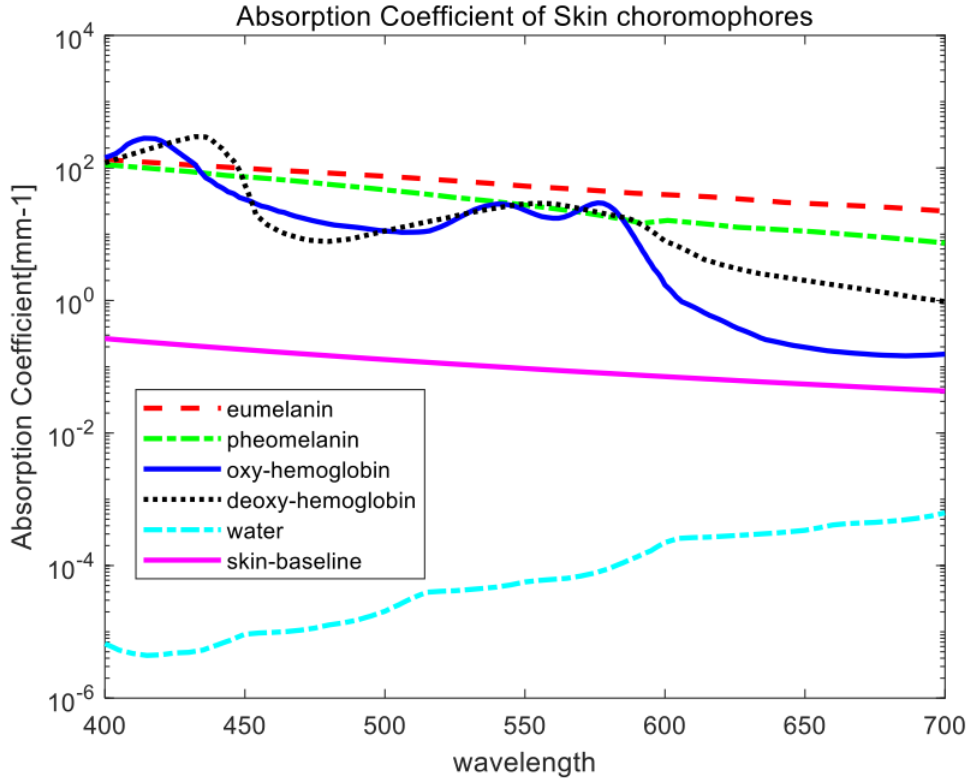
Figure 2.9: Absorption coefficient of pigments along wavelength in the visible light range

photoaging and main optical properties in this subsection. More details like how to apply these optical properties in our skin model will be discussed later.

2.2.4 The State of the Art

In this part, state-of-the-art approaches that describe light-skin interaction will be presented. Some of them are derived analytically from radiative transfer equation, some of them regard light as an ensemble of enormous photons and simulate the propagating process for each photon, and some of them directly fit the distribution profile of light with the optical properties of tissues using equations or other methods. We first introduce the radiative transfer theory, which is fundamental to expand some other approaches, for example, diffusion approximations.

2.2.4.1 Radiative Transfer Equation

Radiation propagating through the medium is influenced by the absorption, emission and scattering, so the energy is also transferred in the form of electromagnetic radiation. A beam of radiation loses energy due to the absorption, gains energy during the emission, and redistributes energy due to the scattering while propagating. To describes these interactions and the distribution of radiance mathematically, the radiative transfer equation (RTE) comes out[50, 51]. This equation is widely used in several fields, such as optics, astrophysics, atmospheric science and remote sensing. The radiance is a physical quantity denoted as L in radiometry that describes the radiant flux per unit solid angle in a specified direction and a unit area perpendicular to this direction.

$$L = \frac{\partial^2 \Phi}{\cos\theta \partial A \partial \Omega} \tag{2.5}$$

where Φ is the radiant flux; $\cos\theta \partial A$ is the unit projected area; Ω is the solid angle. The SI unit of the radiance is the watt per steradian per square meter ($W{\cdot}sr^{-1}{\cdot}m^{-2}$).

The absorption in RTE is described by the absorption cross section, σ_a. Cross section is a term used to express the possibility of interaction between particles in physics. So σ_a indicates the probability density that light is absorbed per unit distance while travelling in the medium. And the variation of the radiance after being absorbed is given by:

$$dL_0(x, \vec{\omega_0}) = -\sigma_a(x, \vec{\omega_0}) L_i(x, \vec{\omega_i}) dt \tag{2.6}$$

where $L_0(x, \vec{\omega_0})$ is the outgoing radiance with the position x and the direction $\vec{\omega_0}$; $L_i(x, \vec{\omega_i})$ is the incident radiance; t is the ray length.

The emission in RTE describes an increase for the radiance along the trajectory. The electrons absorb the energy of the radiation and jump to the excited state which is not stable. Then they decay back to the ground state and emit photons. Generally the emitted radiation has longer wavelength and thus lower energy. Fluorescence is a typical example of the emission. The variation of the radiance after the emission

is given by:

$$dL_0(x, \vec{\omega_0}) = q(x, \vec{\omega_0})dt \qquad (2.7)$$

where $q(x, \vec{\omega_0})$ is the volume emission function.

The scattering in RTE is divided into two types based on the direction: the in-scattering and the out-scattering. The in-scattering means the radiation is scattered inside the medium. The energy of this part can be regarded as an increase for the outgoing radiance. Here, we need to introduce the scattering cross section, σ_s and the phase function $p(x, \vec{\omega_0}, \vec{\omega_i})$. The phase function describes the probability density of the deflection angle scattered. And the variation of the radiance for both two types scattering is given by:

$$\begin{cases} dL_0(x, \vec{\omega_0}) = \int_\Omega \sigma_s(x, \vec{\omega_0})p(x, \vec{\omega_0}, \vec{\omega_i})L_i(x, \vec{\omega_i})d\omega_i dt \\ dL_0(x, \vec{\omega_0}) = -\sigma_s(x, \vec{\omega_0})L_i(x, \vec{\omega_i})dt \end{cases} \qquad (2.8)$$

We sum up all the interactions in RTE, and finally we get:

$$\begin{aligned} dL_0(x, \vec{\omega_0}) = &-\sigma_t(x, \vec{\omega_0})L_i(x, \vec{\omega_i})dt + q(x, \vec{\omega_0})dt \\ &+ \int_\Omega \sigma_s(x, \vec{\omega_0})p(x, \vec{\omega_0}, \vec{\omega_i})L_i(x, \vec{\omega_i})d\omega_i dt \end{aligned} \qquad (2.9)$$

where σ_t is the extinction coefficient, which equals $\sigma_a + \sigma_s$. Figure.2.10 illustrates all three interactions. The red line stands for the in-scattering part, the green line is the out-scattering part, the blue points are absorbers, and the yellow points are the particles that can emit photons. If the medium is nearly non-scattering, it would be much simple to solve the RTE and get the analytical solution with help of spherical harmonics. However, light is highly scattered inside human skin, in that case, we have to do approximations or directly get the numerical solutions via experimentation and make a look-up table to apply[52, 53].

In the following parts, we will present some approaches derived from RTE and acquire the approximate solutions based on some assumptions.
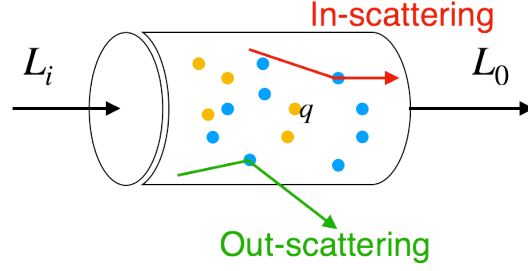
Figure 2.10: Three interactions: absorption, emission and scattering in radiative transfer theory.

2.2.4.2 Kubelka-Munk Theory

Kubleka-Munk theory (KM) was first invented for the simulations of painting film, assuming that only two flux exist inside tissues with opposite directions: forward and backward[54]. It's a one-dimensional approximation of the RTE that describes the optical behavior of a system containing tiny particles that can scatter and absorb incident light. And RTE is thus simplified as two coupled differential equations which describing the forward flux F^+ and the backward flux F^-. KM is widely used in pigment color matching, especially in computer color matching, and used to describe the optical properties of pigments such as hiding power[55].

Based on only two directions for flux, it's convenient to find the relations between F^+ and F^-. We suppose a two-layered structure and explain how KM works in details. Figure.2.11 illustrates how light flux propagates in the two-layered structure according to KM. I_i, I_r and I_t are the incident flux, the reflected flux and the transmitted flux respectively. When I_i reaches the interface 01, part of I_i is reflected back. Note that this theory usually does not consider the surface reflection, however, since the discontinuity of the refractive index at the interface, there exists certainly the reflection. The essence of light propagation is scattering, which means we can also consider the reflection part as the results of the scattering. Inside layer 1 and layer 2, it exists the absorption and the scattering (the emission is not taken into consideration for human skin generally) represented by σ_a and σ_s. Along the axis
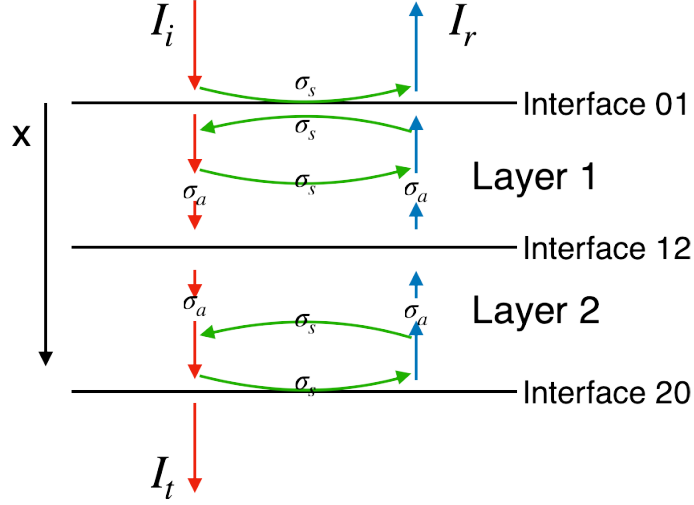
Figure 2.11: Schematic diagram of Kubelka-Munk theory.

X, we can define the variations of F^+ and F^- as:

$$\frac{dF^+}{dx} = -(K+S)F^+ + SF^-$$
$$\frac{-dF^-}{dx} = -(K+S)F^- + SF^+$$

(2.10)

where K and S are related to the effects of the absorption and the scattering respectively. Note that the forward flux and the backward flux are scalar, so it's important to make clear the signs for equations. These equations focus on the variations per dx, and then we must integrate all variations in one layer, which leads to the conclusions of KM. In the condition that the layer is thick enough, the equations can be derived as:

$$\frac{K}{S} = \frac{(1-R_\infty)^2}{2R_\infty}$$

(2.11)

where R_∞ is the reflectance for a layer with sufficient thickness so that the reflectance won't change anymore while increasing this thickness. The general solution derived by Wyszecki and Stiles[56] is given below:

$$R = \frac{1 - R_g(a - b\coth bSd)}{a - R_g + b\coth bSd}$$

(2.12)

where R_g is the background reflectance; $\coth bSd$ is the hyperbolic cotangent of bSd;

d is the thicnkess of one layer; $a = 1 + K/S$ and $b = (a^2 - 1)^{0.5}$. Human skin is a multi-layered tissue as we mentioned before, to calculate the total reflectance of skin, we still need to figure out how to combine the results of every sublayer. This part will be discussed in the next section of diffusion approximation theory due to its similarity.

In summary, KM is an simplified solution to the RTE. It assumes only two directions of flux exists inside the medium. And this leads to some limitations of KM[57]:

- The optical properties inside one layer need to be homogeneous, which means the absorption and scattering coefficient stay the same.

- The effect of refractive index is neglected at the interfaces. This leads to that the measured reflectance is usually larger than the reflectance obtained by KM. This part can be corrected by adding the surface reflection into KM equations, shown below:

$$\frac{K}{S} = \frac{[1 - (R_\infty - R_{surface})]^2}{2(R_\infty - R_{surface})} \tag{2.13}$$

- The medium should be highly scattering and the light should be diffused perfectly although many applications doesn't obey this rule.

- The layer should be thick enough (larger than the optical depth) so that light can be scattered but not pass through the layer.

Despite of so many restrictions, KM is still very popular due to its simplicity. Several extension methods has been put forward to improve its performance. The multi-flux methods increase more channels compared to two-flux in KM. Figure.2.12 shows the channels used in multi-flux methods. Instead of only considering the direction perpendicular to the interface, multi-flux methods define other channels with specified angles. The flux in these channels is calculated by combining Mie scattering theory[58]. In fact, when the channels take up the entire sphere, KM will be like the same theory as RTE. Moreover, converging double spherical harmonics method can make KM generalized and reliable in more applications fields[59].
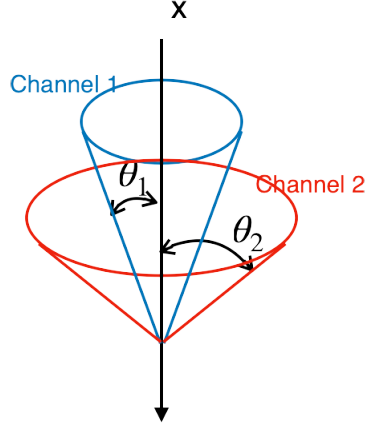
Figure 2.12: Multi-flux methods applied in KM with more channels.

2.2.4.3 Diffusion Approximation Theory

The diffusion approximation theory (DA) makes two appropriate assumptions about the propagating process of light in the medium. The first one is that the scattering events happen much more frequently than the absorption events. The second one is that the energy only changes after having traveled one mean free path. With these two assumptions, we can obtain the approximate solutions from the RTE.

In the RTE, there are six variables (or dimensions), which define the radiance. The position information is decided by x, y, z coordinates in the Cartesian coordinate system, the direction information is given by the polar angle θ and the azimuthal angle ϕ (or the solid angle $\widehat{s}$), and the time information is given by t. The phase function is assumed to be normalized:

$$\int_{4\pi} p(\vec{\omega}, \vec{\omega}')d\omega' = 1 \tag{2.14}$$

The anisotropy factor, g, which is defined as the mean cosine of the scattering angle, is given by:

$$g = \int_{4\pi} (\vec{\omega} \cdot \vec{\omega}')p(\vec{\omega} \cdot \vec{\omega}')d\omega' \tag{2.15}$$

It's apparent that $g > 0$ indicates the scattering is primarily forward; $g < 0$ means the scattering is predominantly backward; $g = 0$ means the scattering is isotropic. When the phase function is a constant, it also results in $g = 0$. Based on DA, the

medium is assumed to be highly scattering, which results in the isotropic distribution of radiation. Then we can integrate the RTE over the sphere at a point x:

$$\vec{\nabla} \cdot \vec{E}(x) = -\sigma_a \phi(x) + Q_0(x) \tag{2.16}$$

where ϕ, $\vec{E}$ are called the scalar and vector irradiance; Q_0 is the 0-th order source term; the time information is neglected due to the second assumption of DA. And the above three terms are given by:

$$\begin{cases} \phi(x) = \int_\Omega L(x, \vec{\omega}) d\omega \\ \vec{E}(x) = \int_\Omega L(x, \vec{\omega}) \vec{\omega} d\omega \\ Q_0(x) = \int_\Omega q(x, \vec{\omega}) d\omega \end{cases} \tag{2.17}$$

The SI unit of the irradiance is the watt per square meter $(W \cdot m^{-2})$. Then the radiance is expanded on a basis set of spherical harmonics $Y_{n,m}$. n, m is the order and the integer respectively, and $|m| \le n$. Due to that the radiance can be regarded nearly isotropic, only the isotropic terms of $Y_{n,m}$ are used. Besides, the 1-st order terms are also included. All terms are given below:

$$L_{0,0}(x) Y_{0,0}(\vec{\omega}) = \frac{1}{4\pi} \phi(x) \tag{2.18}$$

$$\sum_{m=-1}^{1} L_{1,m}(x) Y_{1,m}(\vec{\omega}) = \frac{3}{4\pi} \vec{E}(x) \cdot \vec{\omega} \tag{2.19}$$

And the radiance is the sum of the 0-th order and the 1-st order terms, defined as:

$$L(x, \vec{\omega}) = \frac{1}{4\pi} \phi(x) + \frac{3}{4\pi} \vec{E}(x) \cdot \vec{\omega} \tag{2.20}$$

Note that this equation can not only be applied for isotropic medium but also for highly scattering medium. Because even the phase function is anisotropic, the distribution of light becomes isotropic after numerous scattering events. We substitute the radiance into RTE, and we can get:

$$\vec{\nabla} \phi(x) = -3\sigma_t' \vec{E}(x) + \vec{Q}_1(x) \tag{2.21}$$

where $\sigma_t{'}$ is the reduced extinction coefficient, which is the sum of the absorption coefficient and the reduced scattering coefficient; $\vec{Q_1}(x)$ is the 1-st order source term, given by:

$$\vec{Q_1}(x) = \int_\Omega q(x)\vec{\omega}d\omega \tag{2.22}$$

Here the Fick's law of diffusion is adopted to calculate the diffusion coefficient. This law postulates that the flux propagates from high concentration regions to low concentration regions with a velocity that is proportional to the concentration gradient. The equation is given by:

$$\vec{E}(x) = -D\vec{\nabla}\phi(x) \tag{2.23}$$

$D = \frac{1}{3\sigma_t'}$ is the diffusion coefficient. Then we can derive the integral form of the RTE and get:

$$D\vec{\nabla}^2\phi(x) = \sigma_a\phi(x) - Q_0(x) + 3D\vec{\nabla} \cdot \vec{Q_1}(x) \tag{2.24}$$

Equation2.24 is the classic diffusion equation. In the case of isotropic point source in an infinite medium, the diffusion equation can be simplified as the Helmholtz equation:

$$\sigma_a\phi(x) - \vec{\nabla} \cdot [D\vec{\nabla}\phi(x)] = \delta(x) \tag{2.25}$$

If the medium is homogeneous, then we get:

$$\sigma_a\phi(x) - D\vec{\nabla}^2\phi(x) = \delta(x) \tag{2.26}$$

This is another form of the classic diffusion equation. Here, $\delta(x)$ is an isotropic source term, named the dirac delta function:

$$\delta(x) = \begin{cases} +\infty, & x = 0, \\ 0, & x \neq 0 \end{cases} \tag{2.27}$$

The diffusion equation has a simple solution in an infinite medium with an isotropic

point light source, named Green's function:

$$\phi(x) = \frac{\Phi}{4\pi D} \frac{e^{-\sigma_{tr} r(x)}}{r(x)} \tag{2.28}$$

where Φ is the power of light source; $r(x)$ is the distance to the position of light source; σ_{tr} is the effective transport coefficient:

$$\sigma_{tr} = \sqrt{3\sigma_a \sigma_t'} \tag{2.29}$$

We have discussed the condition that the medium is infinite above. Then we will talk about the finite medium. In this case, the diffusion equation is mostly subjected to the boundary conditions. We take skin as an example. At the interface air-skin, the net inward diffusive flux equals zero, which means:

$$\int_{\Omega-} L(x, \vec{\omega})(\vec{\omega} \cdot \vec{n}_-) d\omega - F_{dr} \int_{\Omega+} L(x, \vec{\omega})(\vec{\omega} \cdot \vec{n}_+) d\omega = 0 \tag{2.30}$$

where the first component represent the inward diffusive flux and the second component represent the outward diffusive flux. $\Omega+$ and $\Omega-$ indicate the outward and inward hemisphere. F_{dr} is the Fresnel diffuse reflectance. By substituting the definitions of $\phi(x)$ and $\vec{E}(x)$, we can yield:

$$\phi(x) - 2D(\vec{n} \cdot \vec{\nabla})\phi(x) = F_{dr}[\phi(x) + 2D(\vec{n} \cdot \vec{\nabla})\phi(x)] \tag{2.31}$$

When the refractive index stay the same between two media, F_{dr} is zero. However, in most cases, the refractive index shows the discontinuity and we have to calculate F_{dr} by:

$$F_{dr} = \int_{2\pi} F_r(\eta, \vec{n} \cdot \vec{\omega}')(\vec{n} \cdot \vec{\omega}') \tag{2.32}$$

where F_r is the Fresnel formula[60]; η is the relative refractive index of the medium with the reflected light to the medium with the transmitted light. Then, we can yield:

$$\phi(x) = 2AD(\vec{n} \cdot \vec{\nabla})\phi(x) \tag{2.33}$$

where A is decided by:

$$A = \frac{1 + F_{dr}}{1 - F_{dr}} \tag{2.34}$$

When the relative refractive index equals 1, AD can be replaced by D. Note that there exists the approximation for F_{dr} acquired from the experimentation data[61]:

$$F_{dr} = -\frac{1.440}{\eta} + \frac{0.710}{\eta} + 0.668 + 0.0636\eta \tag{2.35}$$

Finally, we can yield the diffuse reflectance R_d step by step, given by:

$$R_d(r) = -D\frac{(\vec{n} \cdot \vec{\nabla})\phi(x_o)}{d\Phi(x_i)} \tag{2.36}$$

where the diffuse reflectance at the point x_0 equals the outgoing irradiance divided by the incident flux, and $r = ||x_o - x_i||$.

This analytical solution of the diffuse reflectance is also called Bidirectional Subsurface Scattering Reflectance Distribution Function (BSSRDF), which is widely used in computer graphics. To describe the outgoing radiance, there exists another Bidirectional Reflectance Distribution Function (BRDF). The difference between these two functions is the outgoing position.

$$S(x_i, \vec{\omega}_i; x_0, \vec{\omega}_0) = \frac{1}{\pi}F_t(\eta, \vec{\omega}_i)R_d(||x_i - x_0||)F_t(\eta, \vec{\omega}_0) \tag{2.37}$$

This is a generalized function for both BRDF and BSSRDF, which is defined as the ratio of the outgoing radiance to the incident radiance[62]. x_0, x_i represent the outgoing and incoming positions respectively. $\vec{\omega}_0$, $\vec{\omega}_i$ are the outgoing and incident angles. F_t, R_d are the Fresnel terms and the diffusion profile.

In BRDF, $x_0 = x_i$ leads to simpler calculations. The total reflectance usually is composed of the specular and diffuse reflectance. In BSSRDF, $x_0 \neq x_i$ makes the computation more complicated, and we have to take the interactions inside the medium into account. This is why it's called Subsurface Scattering. Figure.2.13 illustrates the situation for both BRDF and BSSRDF. We can see from (b) that the incident light enters into the medium and is scattered multiple times, finally part of

the incident light returns back. BRDF is usually applied for the opaque material, and the Frensnel equations are used to calculate the reflectance without the need to take account of the subsurface scattering. However, BSSRDF is more generalized and better when dealing with the semi-translucent material.
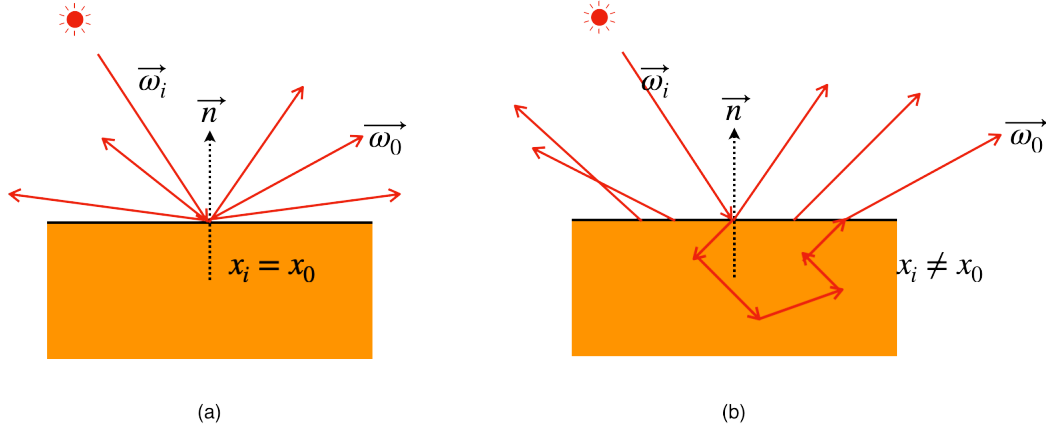
Figure 2.13: Scatttering of light using BRDF (a), and BSSRDF (b).

Back to DA, it was then developed to approximate the light source distribution using two point sources[63, 64]. This is the origin of the dipole approximation. The true light source distribution ϕ is replaced by a dipole source distribution so that it can satisfy the boundary conditions. The dipole is composed of the positive real point source and the negative virtual light source. The details of the dipole is shown in Figure.2.14. The distance $z_v = z_r + 4AD$ and $z_r = \frac{1}{\sigma_t'}$ are for the virtual source and real source respectively. Then the irradiance approximated is defined as:

$$\phi(x) = \frac{\Phi}{4\pi D}(\frac{e^{-\sigma_{tr}d_r}}{d_r} - \frac{e^{-\sigma_{tr}d_v}}{d_v}) \qquad (2.38)$$

where $d_r = ||x - x_r||$ is the distance from the position x to the position of real source; $d_v = ||x - x_v||$ is the distance from the position x to the position of virtual source.

Lastly, the diffuse profile R_d can be obtained by substituting Equation.2.38 to
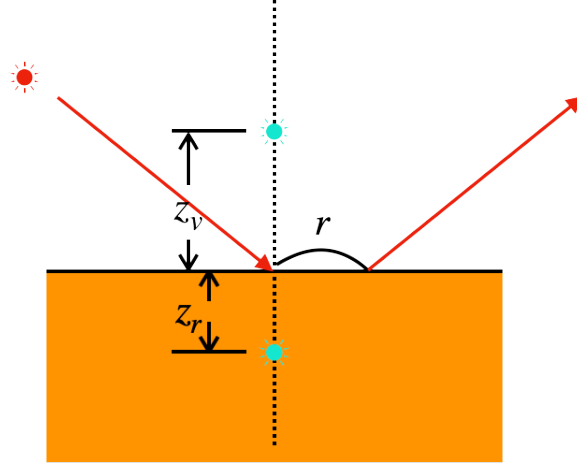
Figure 2.14: Dipole approximation: using two point source (blue) instead of the true light source (red).

Equation.2.36:

$$R_d(r) = \frac{\alpha'}{4\pi}[(\sigma_{tr}d_r + 1)\frac{e^{-\sigma_{tr}d_r}}{\sigma_t'd_r^3} + z_v(\sigma_{tr}d_v + 1)\frac{e^{-\sigma_{tr}d_v}}{\sigma_t'd_v^3}] \tag{2.39}$$

where $\alpha' = \frac{\sigma_s'}{\sigma_t'}$ is the reduced albedo. Then BRDF or BSSRDF can be calculated with three terms known[65]. Despite that the dipole approximation is accurate and satisfy the boundary condition, it is limited and only available for semi-infinite medium, Donner *et al.*[66] extended the dipole to the multipole model. The multipole model takes into account the more strict boundary condition and is designed for the finite medium. The diffuse reflectance and the transmittance of one layer is given by:

$$R(r) = \frac{\alpha'}{4\pi}\sum_{i=-\infty}^{+\infty}[\frac{z_{r,i}(1 + \sigma_{tr}d_{r,i}e^{-\sigma_{tr}d_{r,i}})}{d_{r,i}^3} - \frac{z_{v,i}(1 + \sigma_{tr}d_{v,i}e^{-\sigma_{tr}d_{v,i}})}{d_{v,i}^3}] \tag{2.40}$$

$$T(r) = \frac{\alpha'}{4\pi}\sum_{i=-\infty}^{+\infty}[\frac{(d - z_{r,i})(1 + \sigma_{tr}d_{r,i}e^{-\sigma_{tr}d_{r,i}})}{d_{r,i}^3} - \frac{(d - z_{v,i})(1 + \sigma_{tr}d_{v,i}e^{-\sigma_{tr}d_{v,i}})}{d_{v,i}^3}]$$

$$\tag{2.41}$$

where $d_{r,i}$, $d_{v,i}$ are the distances to the position of the i-th dipole source:

$$\begin{cases} d_{r,i} = \sqrt{r^2 + z_{r,i}^2} \\ d_{v,i} = \sqrt{r^2 + z_{v,i}^2} \end{cases} \tag{2.42}$$

$z_{r,i}$, $z_{v,i}$ are respectively the z-coordinate of the i-th dipole source and are given by:

$$\begin{cases} z_{r,i} = 2i(d + z_{ed,bot} + z_{ed,top}) + l \\ z_{v,i} = 2i(d + z_{ed,bot} + z_{ed,top}) - l - 2z_{ed,top} \end{cases} \tag{2.43}$$

where d is the thickness of the layer; $z_{ed,bot}$, $z_{ed,top}$ are the extrapolation distances to the bottom and top boundary of the layer; l is the mean free path. They are defined as:

$$\begin{cases} l = \frac{1}{\sigma_{t'}} \\ z_{ed,bot} = 2A_{bot}D \\ z_{ed,top} = 2A_{top}D \end{cases} \tag{2.44}$$

After having the analytical solutions of the reflectance and transmittance of one layer, we can yield the total reflectance and transmittance by convolution operations in case of multi-layered structure. Under the assumptions of DA and multipole theory, the medium is regarded to be plane-parallel. We take a two-layered tissue for example as shown in Figure.2.15. Based on the assumptions of DA, the tissue should be highly scattering and homogeneous for each layer. Thus, we consider the reflectance and transmittance for each layer tend to be isotropic. Then we convolve all the interactions to acquire the total reflectance and transmittance, given by:

$$\begin{cases} R_{12} = R_1 + T_1 * R_2 * T_1 + T_1 * R_2 * R_1 * R_2 * T_1 \cdots \\ T_{12} = T_1 * T_2 + T_1 * R_2 * R_1 * T_2 + T_1 * R_2 * R_1 * R_2 * R_1 * T_2 \end{cases} \tag{2.45}$$

where the sign "*" means the convolution operator, and $R_i * T_i$ is defined as:

$$R_i * T_i = \int_{interface} R_i(r)T_i(r')dxdy \tag{2.46}$$

where r, $r' = \sqrt{x^2 + y^2}$ are the radial distances.
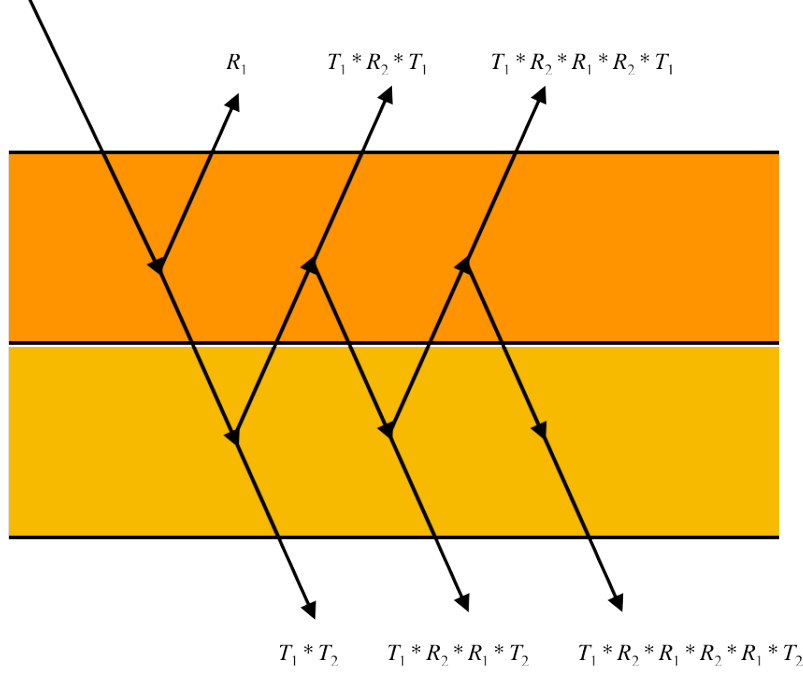
Figure 2.15: Schema of convolutional operation for a two-layered tissue.

When the light reaches layer 1, the R_1 part of light is reflected back. Then, the light that transmits layer 1, is reflected by layer 2, and transmits layer 1 again is also included in R_{12}, denoted as $T_1 * R_2 * T_1$. Furthermore, we can sum up all interactions and finally obtain the total diffuse reflectance as we listed above. It's similar to calculate the total transmittance. This method that sum up all interactions for every layer is learnt from the KM. The difference between them is that KM cares the scalar calculations due to only two directions of flux, so the convolution operator is replaced by the multiplication operator.

Both KM and DA have made remarkable progress in accelerating the computational time to reconstruct the total diffuse reflectance. The simplicity of analytical solutions is easy to implement for biomedical applications. However, there exists some drawbacks that the medium must be highly scattering to get favorable performance and the near-interface light source will increase errors in reconstructing the distribution of light. In the next part we will introduce a totally different method, which doesn't deal with the analytical or numerical solutions from the RTE. And

it is the most widely used and golden method in bioinformatic domain to analyze light-skin interaction.

2.2.4.4 Monte Carlo Simulations

The Monte Carlo (MC) method was first proposed in mid-1940s[67]. This method is a non-deterministic algorithm and aims to calculate numerical solutions based on repeating random sampling process. It's widely used in financial engineering, macroeconomics, biomedicine, computational physics, machine learning and other fields[68]. Basically, all problems that are inherently stochastic can be solved as long as the computational capacity is sufficient. The MC modeling of light transport in multi-layered tissues was proposed and coded in C programming language by Wang and Jacques[69]. The propagating process of light inside tissue can be regarded as an ensemble of numerous random propagating process of energy packets or photons. Based on this assumption, the MC simulations focus on studying the complete movements of one photon and obtain the distribution of light by repeating a large amount of photons. In the following paragraph, we will elaborate how the MC simulations work.
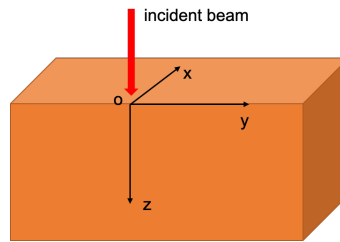
Figure 2.16: The Cartesian coordinates system in Monte Carlo

The rules set for photons in the MC simulations are listed below:

- **Launching a photon** This step is used to inject the photon into the tissue at the origin with the direction perpendicular to the interface. The photon is assumed to carry a weight, W, which represents the energy and is initialized as 1. So the initial information about this photon is defined in the Cartesian

coordinate system as:

$$\begin{cases} x = 0 \\ y = 0 \\ z = 0 \\ u_x = 0 \\ u_y = 0 \\ u_z = 1 \end{cases} \tag{2.47}$$

where x, y, z stand for the position along the axis XYZ shown in Figure. 2.16; u_x, u_y, u_z together build up the incident direction vector which has been normalized. Note that if there is a mismatched boundary at the interface where the photon is injected, we must account for the specular reflectance, R_{sp}, given by[70]:

$$R_{sp} = \frac{(n_1 - n_2)^2}{(n_1 + n_2)^2} \tag{2.48}$$

n_1, n_2 are the refractive index of the surrounding and tissue respectively. Then the weight of the photon is updated as:

$$W = 1 - R_{sp} \tag{2.49}$$

- **Determining the step size** The step size s is decided by randomly sampling based on the probability density function of photon's free path. According to the definition of the extinction coefficient μ_t and the Beer-Lambert's law, we can define s by:

$$s = -\frac{ln\xi}{\mu_t} \tag{2.50}$$

where ξ is taken randomly from the range $]0, 1[$. Note that the logarithm function is time-consuming, which is one of major reasons why the speed of MC simulations is much slower than DA and KM.

- **Moving the photon** After having obtained the step size, we need to move the photon. While moving the photon, some conditions should be taken into

account. Firstly, we must check the boundary condition. This means the step size may be beyond the boundary. In that case, the photon is decided to be reflected or transmitted based on a random number and a threshold. Here, we have two decisions:

$$\begin{cases} if \quad su_z \geqslant z_b - z: \quad s_{temp} = \frac{(z_b-z)}{u_z}; s = s - s_{temp} \\ if \quad su_z < z_b - z: \quad s_{temp} = s; s = 0 \end{cases} \tag{2.51}$$

$$\begin{cases} if \quad \xi \leq R_i: \quad \text{then reflected back;} \\ if \quad \xi > R_i: \quad \text{then transmitted} \end{cases} \tag{2.52}$$

This first decision is used for checking if the photon reaches the interface. The temporary variable s_{temp} is used for storing the path values of the moving action. In the case that the photon reaches the interface, the step size s will be updated by the remaining step size $s - s_{temp}$. The second decision is used for checking if the photon is reflected or transmitted. Here, we again generate a random number ξ to be compared with the threshold, which is set as the internal reflectance R_i. According to the Fresnel's equations, R_i can be calculated as:

$$\begin{aligned} R_i &= \frac{1}{2} \left[(\frac{n_i \cos\theta_i - n_e \cos\theta_t}{n_i \cos\theta_i + n_e \cos\theta_t})^2 + (\frac{n_e \cos\theta_i - n_i \cos\theta_t}{n_e \cos\theta_i + n_i \cos\theta_t})^2 \right] \\ &= \frac{1}{2}(R_s + R_p) \end{aligned} \tag{2.53}$$

where θ_i, θ_t are the incident angle and the exitant angle respectively. n_i, n_e are the refractive index. In fact, this R_i equals to the average of two directions: s-polarization and p-polarization. By substituting the Snell's law, we can get:

$$R_i = \frac{1}{2} \left[\frac{\sin^2(\theta_i - \theta_t)}{\sin^2(\theta_i + \theta_t)} + \frac{\tan^2(\theta_i - \theta_t)}{\tan^2(\theta_i + \theta_t)} \right] \tag{2.54}$$

The Snell's law is shown below:

$$n_i \sin\theta_i = n_e \sin\theta_t \tag{2.55}$$

Secondly, we will update the position of the photon as:

$$\begin{cases} x = x + s_{temp}u_x \\ y = y + s_{temp}u_y \\ z = z + s_{temp}u_z \end{cases} \tag{2.56}$$

where the step size is projected along the axis XYZ and added in the current position. While dealing with the situation that photons reach the interface, we have the results of two decisions and then if reflected back, the direction along the axis Z will be changed: $u_z = -u_z$ and photons will continue the remaining step size. If transmitted, we can calculate the refraction angle based on the Snell's law, update the direction and go on the remaining step size. Figure.2.17 shows the principles of the Snell's law and the reflection. In
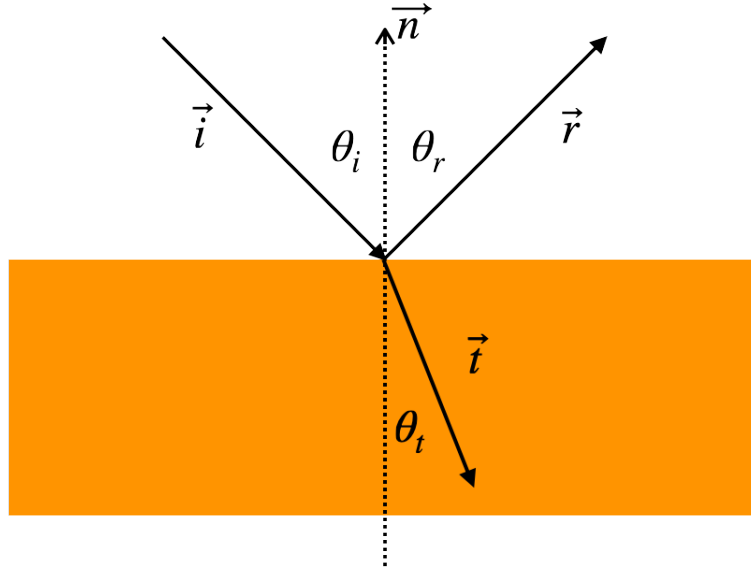
Figure 2.17: Light refraction and reflection at the interface

the case that photons do not reach the interface, the absorption and scattering will be directly discussed.

- **Absorption** The absorption is calculated after the photon has completed one

step. It manifests as an decrease of the photon weight. W will be updated as:

$$W = W(1 - \frac{\mu_a}{\mu_t}) \tag{2.57}$$

This is the only part related to the energy loss in MC simulations and the loss $W \cdot \frac{\mu_a}{\mu_t}$ is added in $A(x, y, z)$, which is the absorption distribution. The photon with the updated weight is scattered then. More important, we must know that all the interactions are calculated at the end of moving a step.

- **Scattering** The scattering is universal inside tissue. The energy of the photon does not change during the scattering, and only the direction is updated. The incident angle can be acquired by (u_x, u_y, u_z). Then the direction scattered will be calculated according to the scattering function. Here, Henyey Greenstein phase function is used for determine the deflection angle, θ. This function describes the probability distribution for the cosine of the deflection angle and is given by[71, 72]:

$$p(\cos\theta) = \frac{1 - g^2}{4\pi(1 + g^2 - 2g\cos\theta)^{3/2}} \tag{2.58}$$

  where g is the anisotropy factor as we mentioned before. g varies from -1 to 1, which is also known as from the backward scattering through the isotropic scattering to the forward scattering. Figure.2.18 illustrates this function under the polar coordinate system. Apparently, $g = 1$ stands for totally forward scattering and $g = -1$ stands for totally backward scattering. It has been proved that Henyey Greenstein phase function matches very well with the single scattering in tissue[73]. g is valued usually from 0.3 to 0.98 for tissues. We integrate $p(\cos\theta)$ to get the probability $P(\cos\theta)$:

$$P(\cos\theta) = \frac{1 - g^2}{2g}\left[(1 + g^2 - 2g\cos\theta)^{-1/2} - \frac{1}{1 + g}\right] \tag{2.59}$$

Then $\cos\theta$ can be derived as a function of P:

$$\cos\theta = \frac{1}{2g}\left[1 + g^2 - (\frac{1-g^2}{1+2Pg-g})^2\right] \tag{2.60}$$

As we know, P is the probability and can be replaced by a random number, ξ. Note that $g = 0$ should also be taken into consideration with $\cos\theta = 2\xi - 1$. Except for the deflection angle θ, another angle named azimuthal angle, denoted as ψ, is simply considered to be distributed uniformly from 0 to π:

$$\psi = 2\pi\xi \tag{2.61}$$

Both two angles are defined with help of random number, then the direction vector $(u_x,\ u_y,\ u_z)$ can be updated by:

$$\begin{cases} u_x = \frac{\sin\theta}{\sqrt{1-u_z^2}}(u_x u_z \cos\psi - u_y \sin\psi) + u_x \cos\theta \\ u_y = \frac{\sin\theta}{\sqrt{1-u_z^2}}(u_y u_z \cos\psi + u_x \sin\psi) + u_y \cos\theta \\ u_z = -\sin\theta \cos\psi \sqrt{1-u_z^2} + u_z \cos\theta \end{cases} \tag{2.62}$$

Note that the trigonometric operations are time-consuming, and this is another factor that slows down the MC simulations.
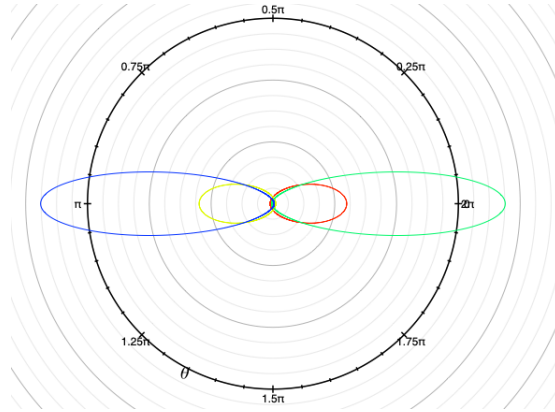
Figure 2.18: Polar plot of $p(\theta)$ for $g = -0.7$, blue; $g = -0.5$, yellow; $g = 0.5$, red; $g = 0.7$, green

• **Weight checking and roulette surviving** Once the photon has suffered

both the absorption and scattering, there exists a step for checking the current weight to ensure that the simulation doesn't iterate endlessly. Here, we must set a threshold, k, as the lower limit of weight (e.g., $0.001W$). Note that this lower limit affects the speed of the MC simulations. If it's too small, that's a disaster for computational time. On the contrary, the errors will increase if the threshold is too large. It's better to find out the acceptable threshold by experimentation. Moreover, the photon with $W \leq k$ need to do a roulette surviving game.

$$W = \begin{cases} aW & \text{if} \quad \xi \leq 1/a \\ 0 & \text{if} \quad \xi > 1/a \end{cases} \tag{2.63}$$

where a is the surviving coefficient that gives a chance for photons to increase their weights. Note that a should not be too large to avoid the situation that the simulated distribution of light is abnormally larger then the measured one. $W = 0$ stands for the termination, then the next photon packet will be injected until there is no more photon packets.

In summary, the MC simulations do not derive the analytical solutions from the RTE but simulate the movements of photons, which is more intuitive to understand the principles compared to the DA and KM. Figure.2.19 shows the concrete flowchart of the MC simulations. What's more, it is regarded as the golden method in biomedicine and bioinformatic fields to obtain the reflectance spectrum of human skin. Thus, it is usually used as the benchmark to evaluate other light-skin interaction methods. The accuracy of MC simulations depends on many aspects, such as the number of photon packets, the lower limit of photon weight. Figure.2.20 describes the fluence rate inside a three-layered tissue using the MC simulations. However, this method suffers from the unbelievable computational costs. This is the only main drawback. Recently, many researches has been done to solve the problem. Benefiting from the advance of computational capacity, MC simulations have been accelerated a lot. For example, Fang *et al.*[74] takes advantage of graphics processing units to accelerate MC simulations with the speed being improved almost 1000 times faster. There exists great potential for MC simulations!
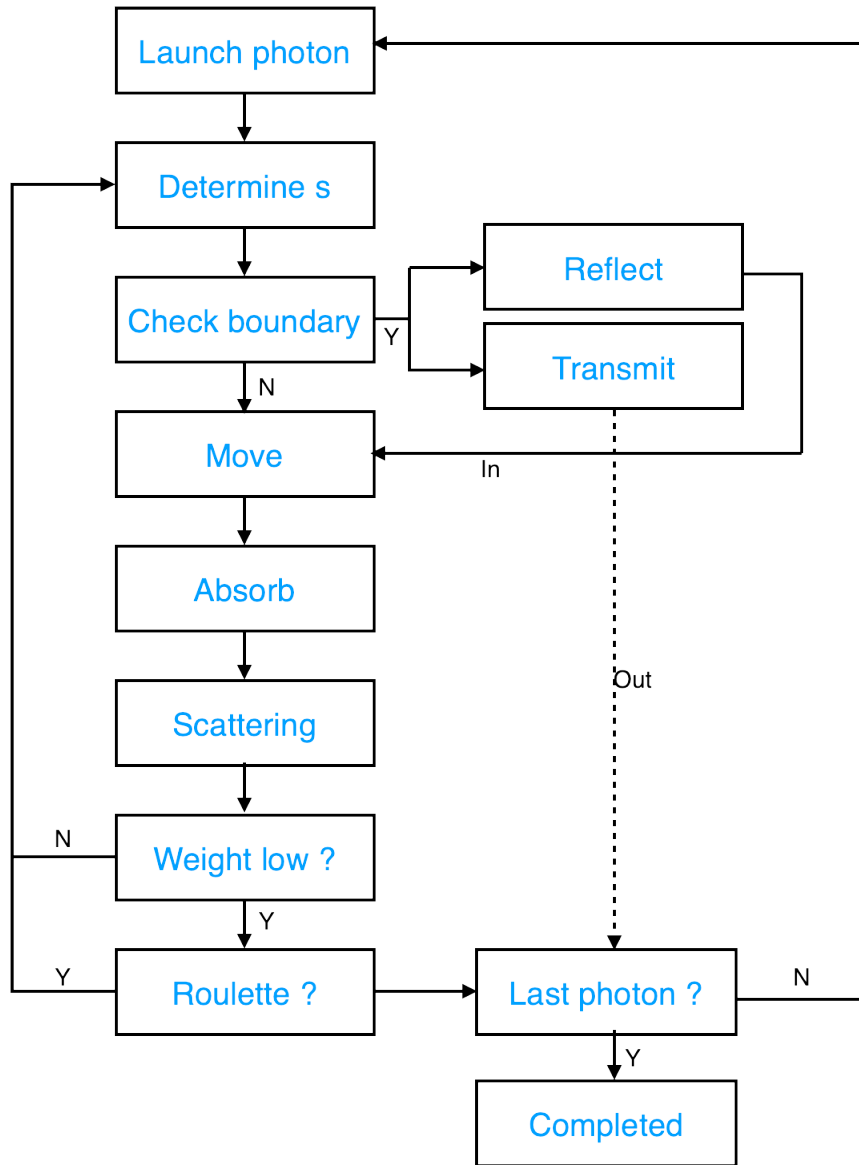
Figure 2.19: Flowchart of Monte Carlo simulations

We have introduced skin structure and enough approaches to accomplish light-skin interaction tasks in above sections. And our research aims to analyze and characterize skin based on skin model and light-skin interaction approaches. This requires the skin reflectance data. In this section, we mainly focus on introducing how to obtain the hyperspectral reflectance (HR) from skin.

One of the most important components to acquire HR is the sensor in camera that receive light. Generally, cameras in smartphones are RGB based. The light
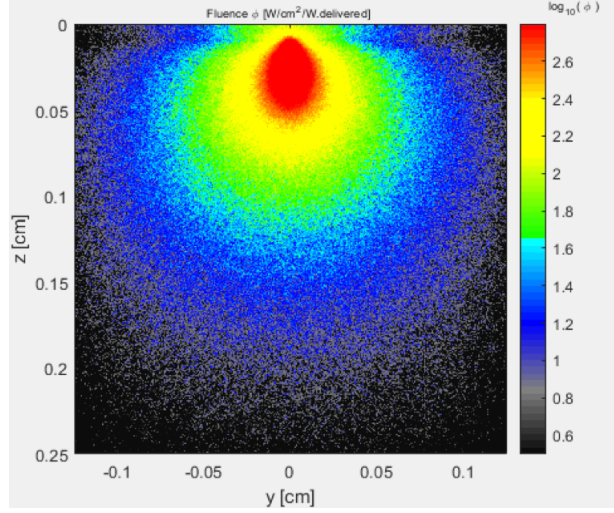
Figure 2.20: Fluence rate map of a three-layered tissue obtained by the MC simulations

information over wavelengths are rearranged and processed into three channels: red, blue and green. There three colors are also the best region for our eyes. To acquire detailed information, we need sensors that contain narrow band spectral filters. These spectral filters usually have a narrow spectral response with full width at half maximum (FWHM) around 2-10 nm. Figure.2.21 shows a snapscan hyperspectral imaging (HSI) sensor made by imec[75]. While detecting HR, sensors are moved and all spectral filters integrated in sensors will scan objects and store the information. Then all information is fused together, and we can get the hyperspectral information.
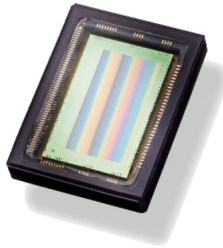
Figure 2.21: Snapscan HSI sensor from imec

Except for sensors, several instruments have been invented for multiple functions. For example, the integrating sphere is designed to acquire the total diffuse

reflectance or transmittance. And the source-detector separations are designed to acquire the spatial-resolved reflectance. Here, we will give an introduction of the integrating sphere. The integrating sphere was first published in 1900[76] and is a cavity sphere coated with a white diffuse reflection material on the inner surface. One or more holes are opened, which are used for light emitting devices and light receiving devices. The inner surface is designed to be uniformly scattering so that the incident light at any positions on the inner surface is distributed equally to all other positions. The spectral reflectance of the diffuse white reflective coating in the visible spectrum is above 99%. In this way, the light entering the integrating sphere is reflected multiple times to form a uniform illuminance on the inner surface. To acquire the total diffuse reflectance or transmittance, we can install as shown in Figure.2.22.
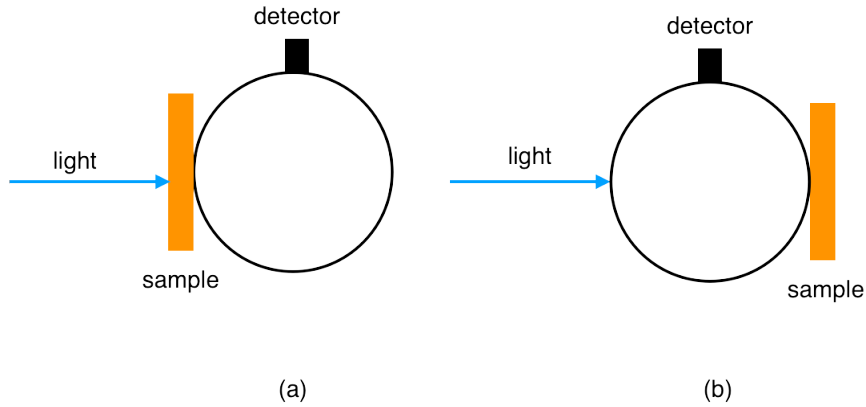
Figure 2.22: Measurement of (a) the total transmittance; (b) the total diffuse reflectance using integrating sphere.

Despite of the great performance of the integrating sphere, it is much expensive and even small commercial integrating sphere cost thousand of dollars. Recently with help of 3D printing, low cost DIY spheres can be produced and have been proved with favorable accuracy[77]. All in all, not only sensors but also optical instruments are required for measuring HR. And sensors that can perceive hyperspectral information are the core of HSI techniques.

2.3 Conclusion

In this chapter, we introduced separately skin anatomical structure, state-of-the-art approaches that describe light-skin interaction and HSI techniques. To characterize and analyze human skin, firstly, we must build a proper skin model. Our research aims to obtain the useful information from skin based on diffuse reflectance. That's why we mainly focus on exploring the optical properties. Secondly, after having understood the primary absorbers and scatterers, we explain the light-skin interaction based on the RTE, and list several widely used approaches. Then we introduce how to acquire the diffuse reflectance from hyperspectral sensors. So the diffuse reflectance calculated or simulated by light-skin interaction approaches and measured by optical instruments can be analyzed and compared together. Overall, skin model provides us the optical properties of every layer, then the diffuse reflectance is derived based on the optical properties, finally the diffuse reflectance can be analyzed inversely to extract the information of skin structure. And in the next chapter, we will present a quantitative analysis of skin biological parameters based on diffuse reflectance.

Quantitative Analysis of Skin based on Diffuse Reflectance

Contents

3.1 Introduction

Skin, which is the largest organ and the soft outer tissue of human body since many conditions or symptoms of diseases are indicated by skin appearance, has become a significant part of research topics in biomedicine and bioinformatic fields, for instance, the detection of pigments deposited inside skin (*e.g.*, melanin, hemoglobin, etc.) based on diffuse reflectance. Benefiting from the development of diffuse reflectance spectroscopy (DRS) techniques, diffuse reflectance can be acquired in the simpler way. Additionally, DRS is widely used because it's non-invasive and cost-effective. Combined with skin models, light-skin interaction approaches are applied to analyze diffuse reflectance monitored by DRS instruments. These approaches

describe how photons transport inside tissue, and derive diffuse reflectance based on the optical parameters of skin models, which generally are formed as a function of volume fractions of biological parameters. This technique has been applied to diagnose diseases, etc. [78, 79, 80, 81].

In the past two decades, the extraction of skin inner parameters based on diffuse reflectance has progressed rapidly. Light-skin interaction approaches, such as diffuse approximation (DA), Kubelka-Munk (KM), and Monte Carlo (MC) simulations as we mentioned in Chapter 2, have been improved a lot. Moreover, machine learning methods have also been applied more commonly to map diffuse reflectance and the optical properties of skin. Among them, MC is usually used to validate other methods as the first verification because it simulates the movement of energy packets which obey the rules of radiance transport and has a good fitting performance with the measured data [82]. Fredriksson *et al.*[83] proposed a three-layered skin model based on inverse MC in two source-detector system, which is able to estimate the bio-optical parameters of tissue from diffuse reflectance. Despite that MC did a great job in reconstructing diffuse reflectance, it suffers from enormous computational time. To overcome this drawback, Sharma *et al.* proposed a look-up table based on a two-layered skin model using inverse MC, which is then generalized for a wide variety of probe-geometries with the error of absorption properties varying from 12-25 %[84]. A look-up table is a data structure such as an array or associative array where runtime computation is replaced a simple query operation. Since extracting values from memory is usually much faster than complex calculations in MC, the speed increase in this way is very significant. Besides that, with help of GPU, MC performs a massive speedup nearly 1000 times over the traditional CPU mode[85]. However, inverse MC needs to iterate many times during the reflectance curve-fitting process. The overall time cost is still too large. DA is well-known by applying dipole or multipole source pairs instead of true light source to obtain the analytical solutions of radiative transfer equation (RTE). DA assumes that the scattering dominates the light-skin interaction over the absorption. And it's not appropriate when light source is near the interface of skin tissue [86] or the tissue is highly anisotropic and lowly scattering[87]. Naglič *et al.* tested the suitability

of DA for fitting the diffuse reflectance spectra and extracting bio-parameters from human skin in vivo [88]. KM is similar to DA, which also derives the analytical solutions from RTE. It assumes only two flux directions exist in tissue, which simplifies computational complexity. A hybrid KM model was developed to assess the absorption of skin[89]. Then, this hybrid KM model was applied to extract physiological skin parameters[90]. However, KM is not accurate as DA or MC. It's more suitable for computer graphics. Other approaches, like designing empirical equations to fit the diffuse reflectance, are also widely adopted. These empirical equations using polynomial equations based on exponential functions, Gaussian functions or in other forms have no worries about the computational speed but the accuracy limits them[91, 92, 93, 94, 95]. Recently, with the development of deep learning, artificial neural networks (ANN) have been applied in this domain more and more frequently. Yudovsky, Nguyen and Durkin simulated spatial frequency domain reflectance of skin for multiple wavelength with a forward neural network (FANN) and found that the optical properties could be determined independently with minimal coupling [96, 97]. This modelling method is not only precise but also robust [98] when dealing with the diffuse reflectance collected by separated source-detectors. Overall, compared to the traditional skin analysis method, biopsy, quantitative skin analysis based on diffuse reflectance is non-invasive and fast. In our research, we replaced MC with FANN. The reflectance for training in [99] is simulated using the source detector separations, which is less robust than the total diffuse reflectance that we used. And the skin models are also different, in [99], it is a 2-layered structure and we studied both 2-layered and 3-layered structure. Also, the wavelength range varies from 450-700 nm. Besides, we introduced a Residual Volume Fraction method to calculate the absorption coefficients.

Our research aims to apply FANN in extracting physiological skin parameters based on the total diffuse reflectance. Different from the existing researches, we have studied both two-layered and three layered skin model with more physiological parameters, such as, β−carotene. And in total 50000 reflectance curves are generated for the training database to avoid over-fitting. Firstly, a skin model is built to map physiological and optical skin parameters. Secondly, MC simulations are used

for generating diffuse reflectance spectra database to train FANN. Thirdly, a reflectance curve-fitting method is fused with FANN for estimating physiological skin parameters. Finally, FANN is validated and analyzed in terms of three pigmented skin types.

3.2   Skin Model

Human skin is a multi-layered biological tissue, which generally is divided into three layers: the epidermis, the dermis and the subcutis. Moreover, these three layers can be detailed with many sub-layers as we mentioned in Chapter 2. A maximum 9-layered skin model has been researched by refining the epidermis and the dermis which consists of stratum corneum, stratum granulosum, stratum basale, papillary dermis, subpapillary dermis, upper blood net dermis, recticular dermis, deep blood net dermis, and subcutis[100]. Although a complex skin structure contains more information, it increases the computational time especially using MC simulations. In our research, a two-layered model including the epidermis and the dermis and a three-layered model including additionally the subcutis were considered.

Skin appearance is mainly influenced by the optical properties of skin layer. Following this, we defined each layer with the thickness, absorption coefficient, scattering coefficient, refractive index and anisotropic factor. The thickness of the epidermis varies from 0.027 to 0.15 mm[101, 102, 103]. Light propagating in this layer was absorbed mostly by melanin, which is a common natural biological pigment. Moreover, there are two types of melanin, of which the absorption spectra in the visible light range are not the same. So eumelanin and pheomelanin exhibit differences in color. The absorption coefficient of the epidermis can be defined as a linear wavelength-dependent function as:

$$
\begin{aligned}
\mu_{a\_epi} = & \, C_m * (\mu_{a\_pheo} * ratio_{pheo\_eu} + \mu_{a\_eu} * (1 - ratio_{pheo\_eu})) \\
& + (1 - C_m) * C_{\beta\_epi} * \mu_{a\_\beta} \\
& + (1 - C_m) * (1 - C_{\beta\_epi}) * C_{w\_epi} * \mu_{a\_w} \\
& + (1 - C_m) * ((1 - C_{\beta\_epi})) * (1 - C_{w\_epi}) * \mu_{a\_baseline}
\end{aligned}
\tag{3.1}
$$

where $C_m, C_{\beta\_epi}, C_{w\_epi}$ represent the volume fraction of melanin, $\beta-$carotene and water in the epidermis respectively; $ratio_{pheo\_eu}$ is the ratio of pheomelanin to eumelanin; $\mu_{a\_pheo}, \mu_{a\_eu}, \mu_{a\_beta}, \mu_{a\_w}$ stand for the absorption coefficient of pheomelanin, melanin, $\beta-$carotene and water; the absorption coefficient of skin baseline $\mu_{a\_baseline}$ is an approximation given by [82] and it can be considered as the absorption of collagen fibers inside skin without any other biological pigments.

The dermis is composed of dense, irregular connective tissue and blood vessels. The thickness of the dermis is between 0.6-3 mm[101, 102, 103]. The dominant biological pigment in this layer is hemoglobin in the blood. Hemoglobin can also be divided into two types based on if it's oxygenated or not. The absorption spectra of oxy-hemoglobin and deoxy-hemoglobin differ clearly in the visible light range. And the absorption coefficient of the dermis is a weighted combination of the primary hemoglobin absorption, and the minor absorption of skin baseline, $\beta-$carotene, bilirubin and water, and is given by

$$
\begin{aligned}
\mu_{a\_der} = &\, C_{bl\_der} * (\mu_{a\_oxy-hemo} * S + \mu_{a\_deoxy-hemo} * (1-S)) \\
&+ (1 - C_{bl\_der}) * C_{\beta\_der} * \mu_{a\_\beta} \\
&+ (1 - C_{bl\_der}) * (1 - C_{\beta\_der}) * C_{bili} * \mu_{a\_bili} \\
&+ (1 - C_{bl\_der}) * (1 - C_{\beta\_der}) * (1 - C_{bili}) * C_{w\_der} * \mu_{a\_w} \\
&+ (1 - C_{bl\_der}) * (1 - C_{\beta\_der}) * (1 - C_{bili}) * (1 - C_{w\_der}) * \mu_{a\_baseline}
\end{aligned}
$$

$$(3.2)$$

where $C_{bl\_der}, C_{\beta\_der}, C_{bili}, C_{w\_der}$ are the volume fraction of blood, $\beta-$carotene, bilirubin and water in the dermis; S indicates the oxygen saturation in the blood; $\mu_{a\_oxy-hemo}, \mu_{a\_deoxy-hemo}$ stand for the absorption coefficient of oxy-hemoglobin and deoxy-hemoglobin respectively considering the concentration of hemoglobin in the blood[104].

Lastly, the subcutis is set as an up to 5 mm thick tissue in our research. The absorbers in the subcutis include blood, fat, water, and skin baseline. The absorption coefficient of this layer is similar to the dermis by adding the extra absorption

of fat and is given by

$$
\begin{aligned}
\mu_{a\_sub} = {} & C_{bl\_sub} * (\mu_{a\_oxy-hemo} * S + \mu_{a\_deoxy-hemo} * (1 - S)) \\
& + (1 - C_{bl\_sub}) * C_{w\_sub} * \mu_{a\_w} \\
& + (1 - C_{bl\_sub}) * (1 - C_{w\_sub}) * C_{fat} * \mu_{a\_fat} \\
& + (1 - C_{bl\_sub}) * (1 - C_{w\_sub}) * (1 - C_{fat}) * \mu_{a\_baseline}
\end{aligned}
\tag{3.3}
$$

where $C_{bl\_sub}, C_{w\_sub}, C_{fat}$ represent the volume fraction of blood, water and fat in the subcutis; μ_{a_fat} is the absorption coefficient of fat.

All absorption coefficients are taken from in vivo experimentation[105]. Here, a mathematical method called residual volume fraction is used for dealing with the situation that the sum of the volume fraction of all pigments surpasses 1. This is a common problem when adding too many types of pigments in skin model. We assume that μ_a^i is the absorption coefficient of the i-th pigment with the volume fraction C_i in one layer. Then, the absorption coefficient of this layer μ_{a_layer} is generally defined as a linear form:

$$
\begin{aligned}
\mu_{a\_layer} &= \sum_{i=1}^{n} \mu_a^i C_i + (1 - \sum_{i=1}^{n} C_i)\mu_{a\_baseline} \\
\text{s.t.} \quad & \sum_{i=1}^{n} C_i < 100\%
\end{aligned}
\tag{3.4}
$$

where n is the total number of pigments types in this layer. However, when n is too large, it's quite normal that the condition can not be satisfied. That's why we introduce residual volume fraction. And the modified equation is shown as:

$$
\mu_{a\_layer} = \sum_{i=1}^{n} \left[\prod_{j=1}^{i-1}(1 - C_j) \right] C_i \mu_a^i + \prod_{i=1}^{n}(1 - C_i)\mu_{a\_baseline}
\tag{3.5}
$$

Note that this method may reduce the weight of pigments. The wavelength-dependent absorption coefficients of all pigments involved in our skin model is shown in Figure.3.1 using data from[105]. It's apparent that melanin and hemoglobin show stronger absorption capacity than other pigments in the visible light range. And an
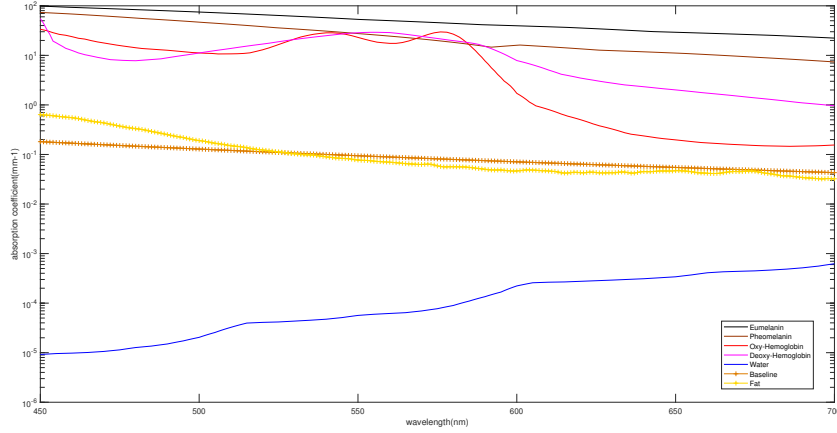
Figure 3.1: Absorption coefficient of pigments along wavelength in the visible light range

inverse "W" shape has been observed for oxy-hemoglobin from 500 to 600 nm, which is an important pattern to be distinguished from non-skin and will be discussed in Chapter 5.

Besides the absorption, the scattering events occur massively inside the skin. To define this interaction, Rayleigh scattering and Mie scattering are commonly used in skin optics. The scattering coefficient is fitted with an equation to match those experimentation results according to[106]:

$$\mu_s = \mu_{s_{500(nm)}} * (f_{Ray} * (\frac{\lambda}{500(nm)})^{-4} + (1 - f_{Ray}) * (\frac{\lambda}{500(nm)})^{-b_{Mie}}) \qquad (3.6)$$

where $\mu_{s_{500(nm)}}$ is the scattering coefficient measured at 500 nm; f_{Ray} indicates the fraction of Rayleigh scattering, and clearly $1 - f_{Ray}$ is the fraction of Mie scattering; b_{Mie} is called the scattering power which is acquired by fitting the measured data.

To summarize, both the absorption and scattering coefficients of each layer are defined as functions of physiological parameters in our skin model. Table 3.1 shows the symbols, descriptions and ranges of parameters in proposed skin model. Note that the oxygen saturation varies much in the arteries and veins. Generally, 90-95% of hemoglobin is oxygenated, but in the veins, only more than 47% of hemoglobin is oxygenated. Moreover, the anisotropic factors g, refractive indexes n and thickness

Table 3.1: Symbols, descriptions and ranges of parameters in skin model

Layer	Symbol	Description	range
Epidermis	C_m	volume fraction of melanin	1.3-43%[82]
	C_{β_epi}	volume fraction of $\beta-$carotene	0.1-10%
	C_{w_epi}	volume fraction of water	10-20%
	$ratio_{pheo\_eu}$	ratio of pheomelanin to eumelanin	4.9-36%[107]
	d_{epi}	thickness	0.027-0.15 mm[103]
Dermis	C_{bl_der}	volume fraction of blood	0.2-7%[108]
	S	oxygen saturation	50-95%[109]
	C_{β_der}	volume fraction of $\beta-$carotene	0.1-10%
	C_{bili}	volume fraction of bilirubin	0.1-10%
	C_{w_der}	volume fraction of water	40-90%
	d_{der}	thickness	0.6-3 mm[102]
Subcutis	C_{bl_sub}	volume fraction of blood	5-20%
	C_{w_sub}	volume fraction of water	40-90%
	C_{fat}	volume fraction of fat	40-70%
	d_{sub}	thickness	1-5 mm

d of each layer are also predefined before performing MC simulations.

3.3   Implementation of MC simulations

In this section, we design a customized MC simulations in Python v3.6.4 (Python Software Foundation). Firstly, three classes are coded as Photon, Material and Skin-Struct. The class Photon is composed of several attributes including: the position (x, y, z, l), the direction (u_x, u_y, u_z), the weight (w), the status (sta) and the step size (s). The status (sta) indicates if the photon packet is still alive. The l describes the layer which the photon packet currently locates in. And the movements of photon packet in MC are coded in functions: hop, spin and drop. The function hop means that the photon packet takes a step size and changes its coordinates. Before executing function hop, it needs to determine the step size and analyze the boundary condition which is elaborated in Chapter 2. The function drop means energy loss in the propagating process. Note that the absorption and scattering coefficients are

---

Algorithm 1 Hop

Input: position x, y, z; direction u_x, u_y, u_z; step size s;
Output: position x, y, z; step size s;

  1: **if** $s > 0$ **then**
  2:    $x \Leftarrow x + u_x \cdot s$
  3:    $y \Leftarrow y + u_y \cdot s$
  4:    $z \Leftarrow z + u_z \cdot s$
  5:    $s \Leftarrow 0$

Algorithm 2 Drop

Input: position x, y, z, l; weight w; status sta; threshold DEADWEIGHT;
Output: weight w;

  1: **if** $w >$ DEADWEIGHT **AND** $sta \neq$ FALSE **then**
  2:    Finding the absorption coefficient from $\mu_a \Leftarrow$ SkinStruct.layer[l].mua
  3:    Finding the scattering coefficient from $\mu_s \Leftarrow$ SkinStruct.layer[l].mus
  4:    $w \Leftarrow w \cdot \frac{\mu_s}{\mu_s + \mu_a}$
  5: **else**
  6:    go to: roulette()

---

predefined in the class SkinStruct and can be acquired quickly by the variable l. The function Spin means the photon packet changes its direction during the propagating process and it has nothing to do with the energy loss. When u_z is approximate to 1, the calculations can be simplified. Moreover, we can speed up the computational time using temporary values instead of trigonometry operations. The class Material stores the information of different kinds of media. Here, we have recorded the optical properties, such as the anisotropy factor, the absorption coefficients, for three skin sublayers. The class SkinStruct is an ordered structure by combining skin sublayers from the class Material. And we can query quickly the layer information from the attribute l in the class Photon.

To validate this MC simulations code, we compare it to the measured data[110] and other MC simulations by Prahl *et al.*[111] and Wang *et al.*[69]. MC simulations are tested on a slab of turbid medium with the absorption coefficient $\mu_a = 10cm^{-1}$, the scattering coefficient $\mu_s = 90cm^{-1}$, the refractive index $n = 1$, the anisotropy factor $g = 0.75$ and the thickness $d = 0.02cm$. In total 1E07 photon packets are injected ten times with the perpendicular direction to the interface. The average total diffuse reflectance R_d and total transmittance T_t and the standard deviations

Algorithm 3 Spin

Input: position x, y, z, l; direction u_x, u_y, u_z;
Output: direction u_x, u_y, u_z;

1: Deciding the cosine of the deflection angle θ from Henyey Greenstein function:
$\cos\theta \Leftarrow \mathrm{HGEq}(\mathrm{SkinStruct.layer[l].g})$
2: Deciding the azimuthal angle ψ by random number:
$\psi \Leftarrow 2\pi\cdot\mathrm{random.sample()}$
3: **if** $|u_z| > 0.999999$ **then**
4:   $u_x \Leftarrow \sin\theta \cdot \cos\psi$
5:   $u_y \Leftarrow \sin\theta \cdot \sin\psi$
6:   $u_z \Leftarrow \mathrm{sign}(u_z) \cdot \cos\theta$
7: **else**
8:   $u_x \Leftarrow \frac{\sin\theta}{\sqrt{1-u_z^2}}(u_x u_z \cos\psi - u_y \sin\psi) + u_x \cos\theta$
9:   $u_y \Leftarrow \frac{\sin\theta}{\sqrt{1-u_z^2}}(u_y u_z \cos\psi + u_x \sin\psi) + u_y \cos\theta$
10:   $u_z \Leftarrow -\sin\theta \cos\psi \sqrt{1-u_z^2} + u_z \cos\theta$

Table 3.2: Validation results of proposed MC with other methods in a homogeneous slab.

Method	R_d average	R_d error	T_t average	T_t error
van de Hulst[110]	0.09739		0.66096	
Prahl*et al.*[111]	0.09711	0.00033	0.66159	0.00049
Wang *et al.*[69]	0.09734	0.00035	0.66096	0.00020
Proposed MC	0.09732	0.00035	0.66092	0.00021

are calculated. Table 3.2 shows the validations results and we can see that they are well matched. Then we continue to test on a three-layered structure with different optical properties. The results are shown in Table 3.3. Overall, our proposed MC simulations have a good performance in reconstructing the diffuse reflectance spectra. It takes 63 seconds to simulate 1E07 photon packets for the original version, and 49 seconds for the multi-process version using 8-core CPU (Intel i7-7700HQ). To further speed up, a GPU-CUDA based MC is deployed.

3.4   Experimentation and Results

In the following section, we first generate a diffuse reflectance database and train two FANNs for skin models. Then, FANNs are used to reconstruct diffuse reflectance

Table 3.3: Validation results of proposed MC with other methods in a three-layered structure.

Method	R_d	T_t
Gardner *et al.*[112]	0.2381	0.0974
Wang *et al.*[69]	0.2375	0.0965
Proposed MC	0.2380	0.0962

spectrum compared to MC simulations. And we analyze how every physiological parameter affects the reconstructed diffuse reflectance. Both two FANNs are combined with a reflectance curve-fitting method to extract inversely physiological parameters from diffuse reflectance spectra generated by MC simulations afterwards. Finally, we apply two FANNs to the measured diffuse reflectance spectra from database NIST[113]. This database includes in total 100 reference diffuse reflectance spectra of human skin, with the wavelength ranging from 250 to 2500 nm. The spectra were obtained with a commercial spectrophotometer and are directly traceable to the national scale for directional-hemispherical reflectance factor.

3.4.1   Database Generation and FANN training

We have built skin model and implemented MC simulations in Python in above parts. Then the diffuse reflectance database will be generated for ANN training. The refractive indexes (n_{epi}, n_{der}, n_{sub}) and the anisotropic factors (g_{epi}, g_{der}, g_{sub}) of each layer are set as 1.44, 1.37, 1.37, and 0.8, 0.86, 0.75 respectively. For both two-layered and three-layered skin models, firstly, physiological parameters are input to obtain the optical properties of skin. Secondly, the optical properties are input in MC simulations. Finally, the diffuse reflectance at the specified wavelength is acquired. This process iterates 50000 times to form a sufficient database. Note that at the beginning, all physiological parameters are randomly taken from the ranges listed in Table 3.1. At the same time, the wavelength is also selected randomly to acquire the optical properties based on Equations (3.1)-(3.4). It takes 15 hours for a two-layered database and 18.2 hours for a three-layered database. Monte Carlo simulations were accelerated using CUDA by GPU (Nvidia GeForce GTX1060).

For ANN training, we have built FANNs, which are fully-connected networks, using the Deep Learning Toolbox in MATLAB R2018a with 2 hidden layers, 1 input layer and 1 output layer, and 55 neurons deposit in each hidden layer according to [98]. The input layer has six dimensions: μ_{a_epi}, μ_{a_der}, μ_{s_epi}, μ_{s_der}, d_{epi} and d_{der} for two-layered model, and nine dimensions for three-layered model by adding μ_{a_sub}, μ_{s_sub} and d_{sub}. The output layer is one-dimensional: the total diffuse reflectance. The training function is set as the scaled conjugate gradient method. Besides this, normalization and random data division are applied to the database. 70% are used for training, 15% for test and validation separately. And two networks are denoted as 2L-FANN and 3L-FANN for two-layered and three-layered skin models respectively. Figure.3.2 shows the performance which is the mean squared error during the training process. For these two networks, the error decreases dramatically at the start, then it tends to fall smoothly after 5000 epochs, and eventually, it holds steady. Then we will test the performance of two FANNs in reconstructing the diffuse reflectance.

3.4.2   Reconstructing the Diffuse Reflectance using FANN

To validate proposed FANNs, we reconstruct the diffuse reflectance based on same parameters using FANNs and MC simulations. In our research, the spectral bands are set from 450 to 700 nm with 1 nm interval in the visible light range. Three groups are separated in terms of the pigmented degrees: lightly ($C_m \in [1.3\% \quad 3\%]$) , moderately ($C_m \in [11\% \quad 16\%]$) and darkly ($C_M \in [18\% \quad 43\%]$) pigmented. Figure.3.3 illustrates the flowchart of reconstructing diffuse reflectance. Firstly, physiological skin parameters and wavelength λ are input in skin models to calculate the optical parameters. The absorption and scattering coefficients, the thickness of every layer, the refractive index and the anisotropy factor are input then in FANNs. Finally, the wavelength-dependent diffuse reflectance are acquired. For MC simulations, it's the same flowchart, replacing the part of FANNs by MC simulations. Furthermore, to speed up the calculations, we use vector variables instead of scalar variables. This reduces the number of iterations. For every set of physiological skin parameters, we get four diffuse reflectance spectra for 2L-FANN, 2layered-MC, 3L-FANN and
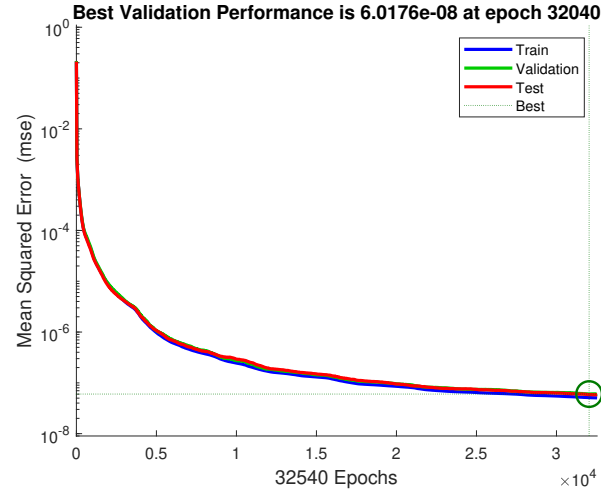
(a) 2L-FANN
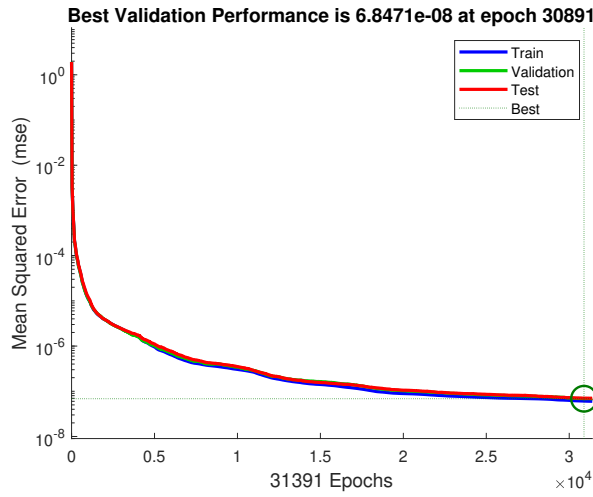
(b) 3L-ANN

Figure 3.2: Performance of (a) 2L-FANN and (b) 3L-FANN
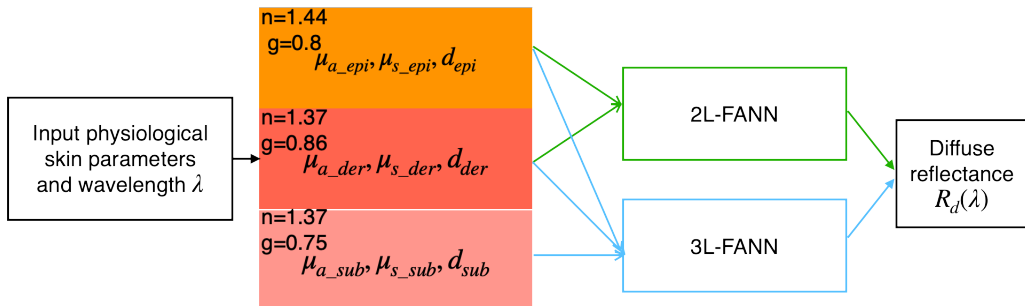
Figure 3.3: Flowchart of reconstructing diffuse reflectance

3layered-MC respectively. The diffuse reflectance spectra of three sets of physiological skin parameters are shown in Figure.3.4. The diffuse reflectance spectra gradually increases from 450 to 500 nm. This is predominantly due to that the absorption coefficients of all pigments except water decrease from 450 to 500 nm. Then, we can see a "W" shape from 500 to 600 nm for (a), (b), showing in high accordance with the absorption coefficient of oxy-hemoglobin. In lightly and moderately pigmented group, "W" shape is very apparent. However, in darkly pigmented group, "W" shape nearly disappears due to the weight of melanin increases and the weight of oxy-hemoglobin decreases correspondingly. Moreover, "W" shape is also highly-related to the oxygen saturation S, which means the ratio of oxy-hemoglobin to deoxy-hemoglobin in blood. The diffuse reflectance continue to increase from 600 to 700 nm, more sharply than 450-500 nm. Besides these characteristics, we also find that the three-layered skin model always shows larger values slightly or significantly than the two-layered skin model from 600 to 700 nm. As we known, light with longer wavelength has better penetrating capacity. The reconstructed diffuse reflectance proves that in the visible light range, light flux can reach the subcutis. So the third layer subcutis is veritably important when simulating light-skin interaction especially when dealing with lightly, moderately pigmented group. The errors between MC simulations and proposed FANNs at each wavelength are recorded in Figure.3.5. For top graph, the absolute errors at each wavelength are almost within 0.0013, and for bottom graph, the absolute errors at each wavelength are nearly within 0.0018. It turns out that our proposed FANNs matches well MC simulations in computing the diffuse reflectance. Before doing the extraction of physiological parameters, we would like to first analyze the effects of every parameter on reconstructing the diffuse reflectance. One parameter is studied by varying its value and fixing all other parameters at the same time. Note that the optical parameters of our skin model are derived using residual volume fraction method. This may lead to that some pigments of which the absorption coefficient is less than the skin baseline doesn't affects the diffuse reflectance correctly. All values are initialized as the lower limit in Table 3.1 and the analysis is carried out based on three-layered skin model.

(a) lightly pigmented skin type

(b) Moderately pigmented skin type

(c) Darkly pigmented skin type
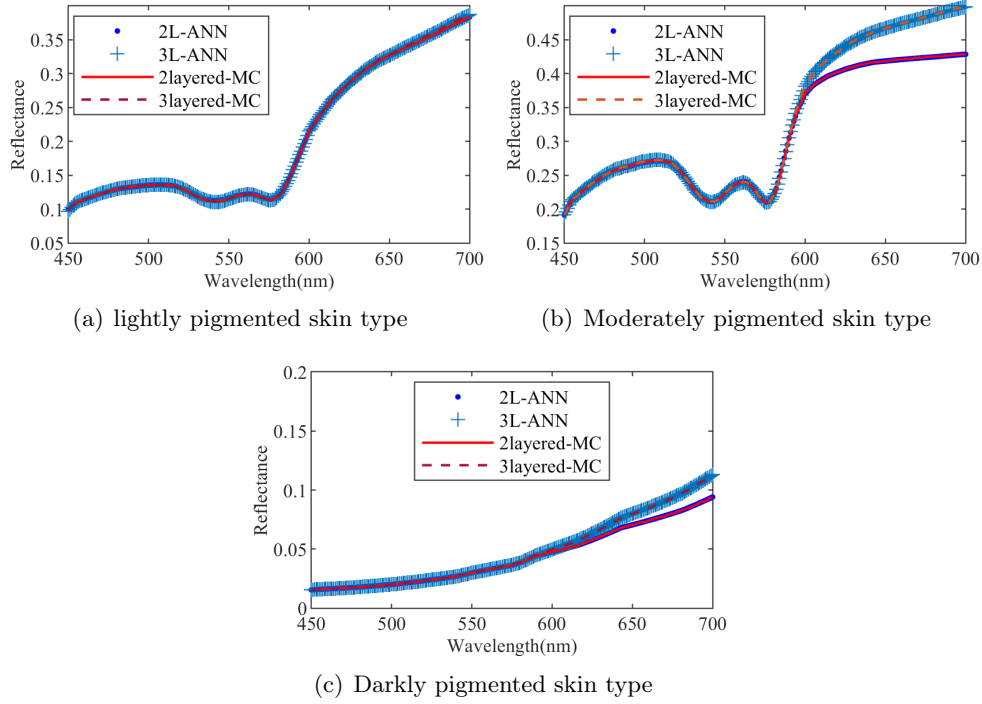
Figure 3.4: Reconstructed diffuse reflectance spectra in three groups: lightly, moderately and darkly pigmented skin types.

- **Melanin** The volume fraction of melanin C_m is set from 1.3 to 43% with 2% increment. Figure.3.6 shows the results of diffuse reflectance from 450 to 700 nm. We find that the diffuse reflectance decreases when C_m increases. The reflectance curve becomes more flattened, and typical "W" shape becomes less evident. The absorption coefficient of melanin decreases gradually and steadily over 450-700 nm. Accordingly, the diffuse reflectance increases gradually and steadily while C_m is too large and melanin dominates the absorption.

- **Ratio of Pheomelanin to Eumelanin** The ratio of pheomelanin to eumelanin, $ratio_{pheo\_eu}$, influences the diffuse reflectance slightly because the absorption coefficients of pheomelanin and eumelanin are similar in the visible light range, and μ_{a_pheo} is slightly smaller than μ_{a_eu}. When $ratio_{pheo\_eu}$ increases, the proportion of pheomelanin increases, thus, the total absorption caused by melanin decreases a little. Correspondingly, the diffuse reflectance grows. The difference between μ_{a_pheo} and μ_{a_eu} becomes larger in long wave-
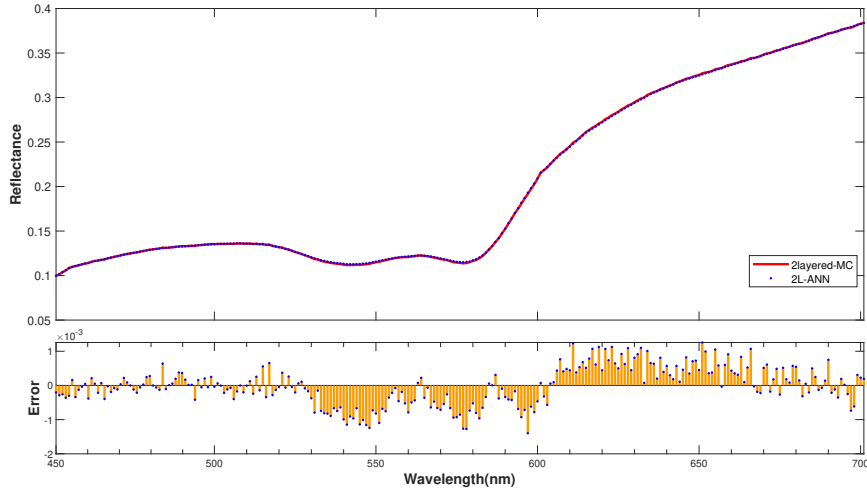
(a) 2L-FANN and MC
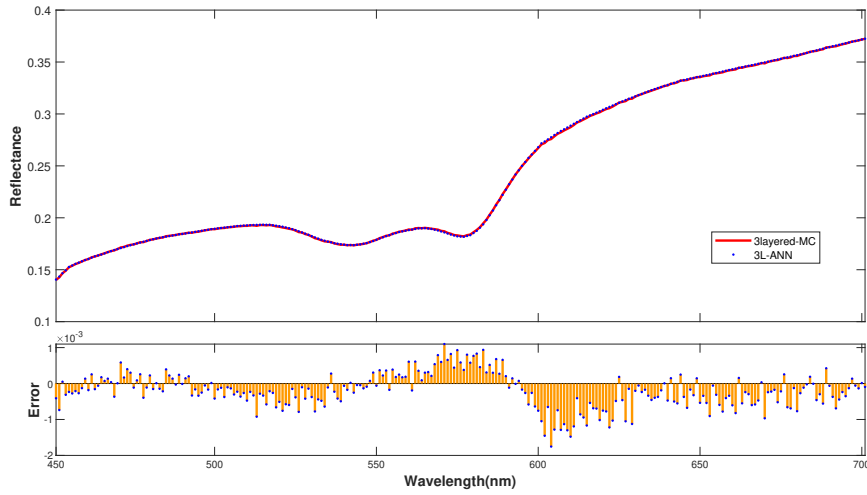
(b) 3L-FANN and MC

Figure 3.5: The errors between FANNs and MC simulations: (a) two-layered and (b) three-layered.

length range. This is also reflected in the reconstructed diffuse reflectance, where the difference in long wavelength range is more apparent as shown in Figure.3.7.

- **Blood and Oxygen Saturation** The absorption coefficient of blood is mainly expressed as hemoglobin, thus, oxygen saturation is also involved.

The volume fraction of blood varies from 0.2 to 7%. Figure.3.8 illustrates the effects of blood in the dermis and subcutis, and oxygen saturation. With the volume fraction of blood increasing both in the dermis and subcutis, the diffuse reflectance decreases. Moreover, the volume fraction of blood in the dermis affects diffuse reflectance more significantly than in the subcutis even that the range of blood variation in dermis is smaller than in subcutis. And "W" shape becomes more evident. On the other hand, the effects of blood in the subcutis mainly locate in the range 600-700 nm, which differs from the former. The effects of oxygen saturation are not uniform from 450 to 700 nm. When it increases, the diffuse reflectance decrease from 450 to nearly 500 nm, increases from about 550 to 575 nm, and increases significantly from 600 to 700 nm. This can be explained according to the absorption coefficients of oxy- and deoxy-hemoglobin. From 450 to 500 nm, the absorption coefficient of oxy-hemoglobin is larger than deoxy-hemoglobin. The absorption is enhanced while the proportion of oxy-hemoglobin increases, that is, S increases. From 550 to 575 nm and above 600 nm, the absorption coefficient of oxy-hemoglobin is smaller than deoxy-hemoglobin. Then, we can see that the diffuse reflectance increases when S increases. Note that all parameters are initialized as the lower limit, and the situation may change if primary pigments, such as melanin, are set as a large value.

- **Thickness of skin layers** Three thickness d_{epi}, d_{der} and d_{sub} are involved in our skin model. The effects of the thickness of every layer is not the same. We start to explain the effects of d_{epi}. The reconstructed diffuse reflectance decreases while d_{epi} grows. The mean free path, denoted as l, is more likely to be less than d_{epi}, resulting in that more parts of light flux transport in the epidermis and is then absorbed. Consequently, the diffuse reflectance drops. However, for d_{der} and d_{sub}, the situation changes. When d_{der} grows, the diffuse reflectance increases in full range. This may be caused by a decrease of transmitted light. More parts of light flux cannot transmit into the next layer, the subcutis, and stay in the dermis. Then light flux is reflected back to the

upper layer. Note that when the volume fraction of blood is large enough, the diffuse reflectance may decrease due to that a large amount of light is absorbed but not reflected back. As for d_{sub}, we can see a significant increase in long wavelength range since light with longer wavelength has better penetrating capacity as we mentioned above. When d_{sub} grows, the light with long wavelength is less likely to transmit, thus, the reflection part increases. Figure.3.9 shows the reconstructed diffuse reflectance by increasing the thickness of each layer.

- **Water, Fat, $\beta-$carotene and bilirubin** These four pigments are put together to discuss since the absorption coefficients of them are usually smaller than skin baseline. As shown in Figure.3.10, the volume fractions of water in three layers have the same effect, causing an increases of the diffuse reflectance. Among them, it's the most apparent in the dermis due to its large values from 40-90%. This leads to a smaller weight of skin baseline. Finally, it is manifested as an increase in diffuse reflectance. The situation is quite similar for fat, $\beta-$carotene and bilirubin. Thus, the extraction of these parameters are the most inaccurate as proved in the next section.
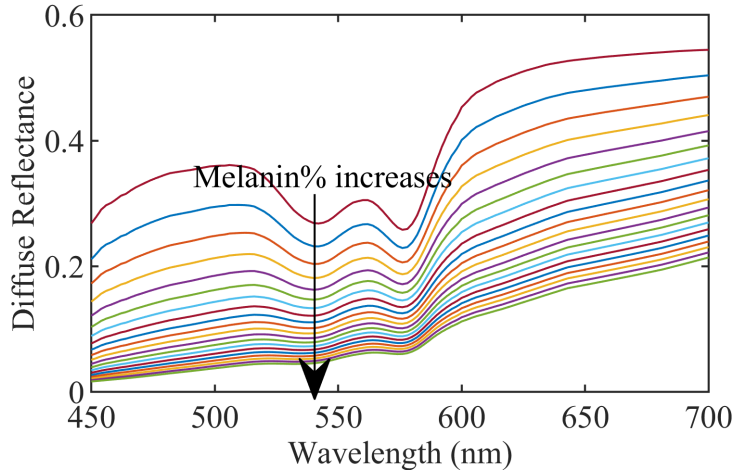
Figure 3.6: Diffuse reflectance reconstructed by increasing the volume fraction of melanin.

In this part, we mainly study on the performance in reconstructing the diffuse re-
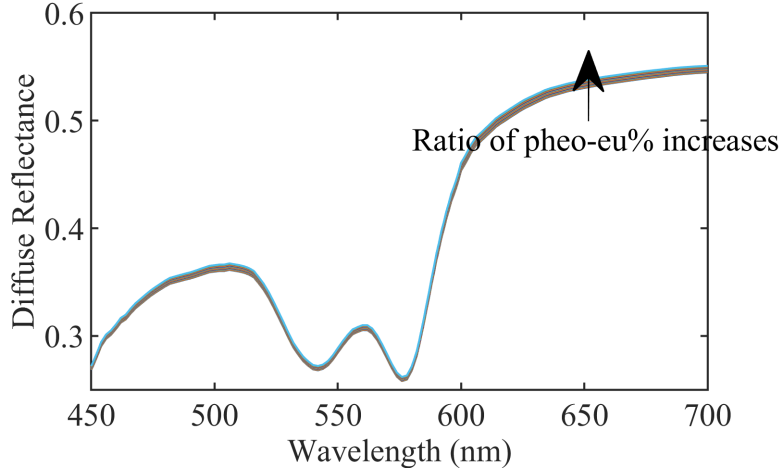
Figure 3.7: Diffuse reflectance reconstructed by increasing the ratio of pheomelanin to eumelanin.

flectance using proposed FANNs and analyze how every physiological parameter affects the diffuse reflectance reconstructed. Our proposed two FANNs have very acceptable performances compared to MC simulations. We will apply them to extract physiological skin parameters in the following part. On the other hand, two pigments (melanin and blood) affects the reconstructed diffuse reflectance significantly. The rest pigments, such as fat and bilirubin, only influence the results slightly. Thus, the inaccuracy of extracting these pigments is predictable.

3.4.3 Extracting physiological skin parameters

Extracting non-invasively physiological skin parameters is our ultimate goal. We have designed skin models and FANNs approaches. The metric used for evaluating the extracting performance is defined as root mean squared relative error (RMSE), ε:

$$\varepsilon = \sqrt{\frac{\sum_{\lambda=450nm}^{700nm}(\frac{R_d(\lambda)-R_t(\lambda)}{R_t(\lambda)})^2}{Nb_\lambda = 251}} \tag{3.7}$$

where $R_d(\lambda)$, $R_t(\lambda)$ are the diffuse reflectance reconstructed and targeted at wavelength λ; Nb_λ is the number of spectral bands, and equals 251 when considering the range 450-700 nm with 1 nm interval.
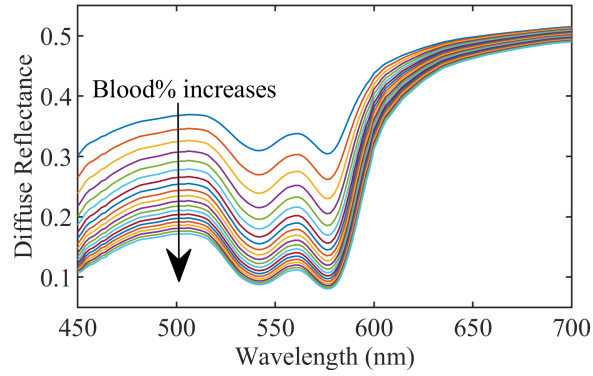
(a) blood in the dermis
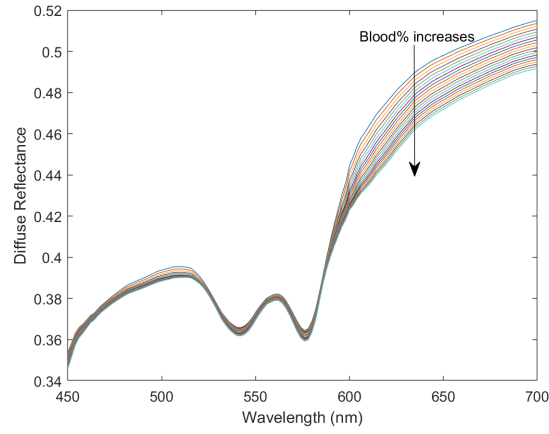
(b) blood in the subcutis
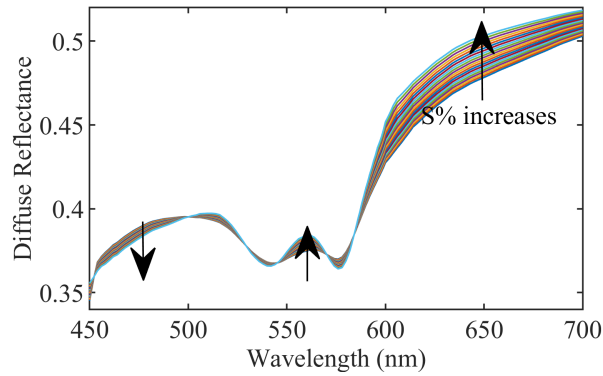
(c) oxygen saturation

Figure 3.8: Diffuse reflectance reconstructed by increasing the volume fraction of blood and oxygen saturation.
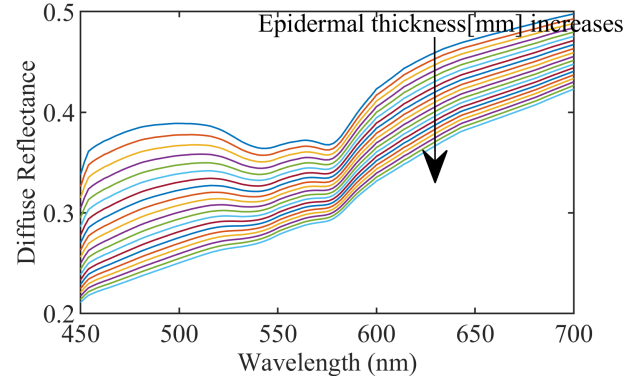
(a) thickness of the epidermis
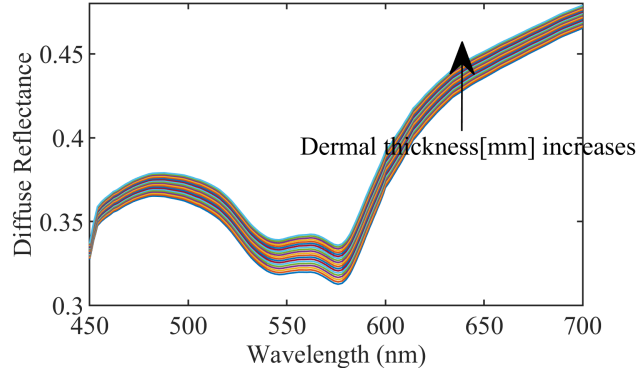
(b) thickness of the dermis
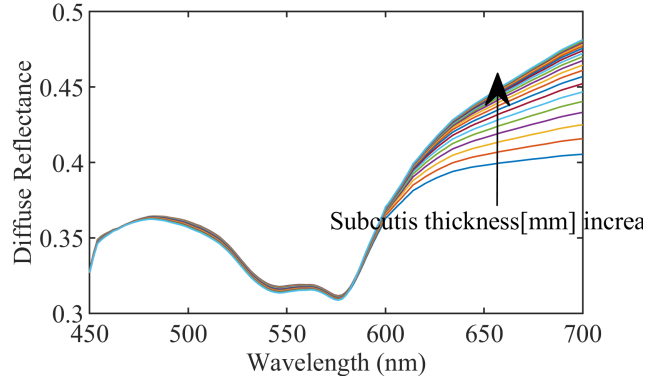
(c) thickness of the subcutis

Figure 3.9: Diffuse reflectance reconstructed by increasing the thickness of the epidermis, dermis and subcutis.
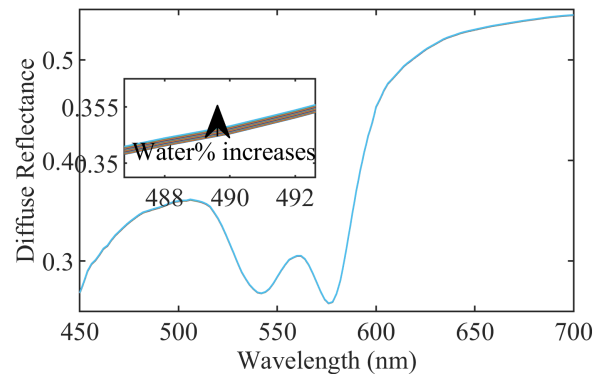
(a) water in the epidermis
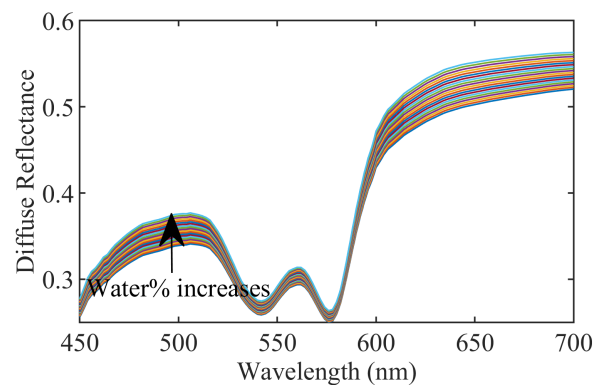
(b) water in the dermis

(c) water in the subcutis

(d) fat in the subcutis
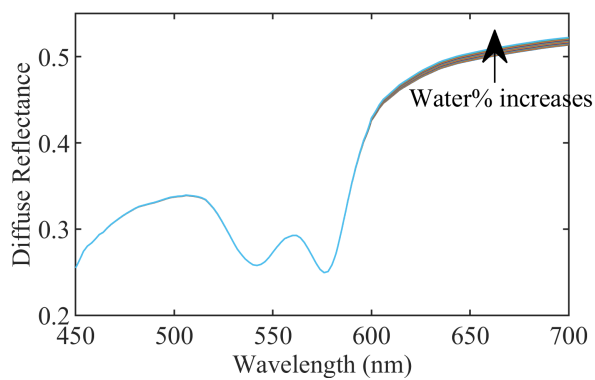
(e) $\beta-$carotene and bilirubin
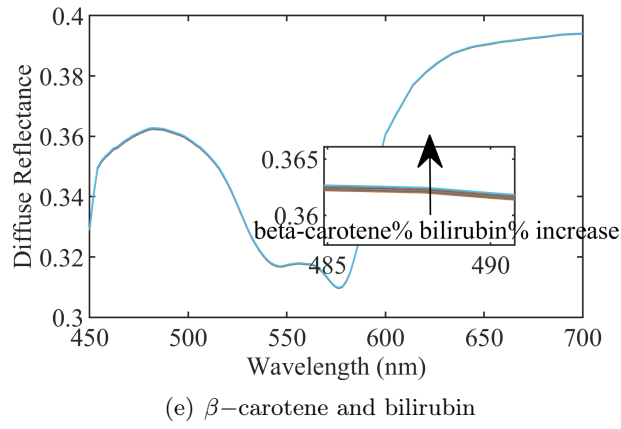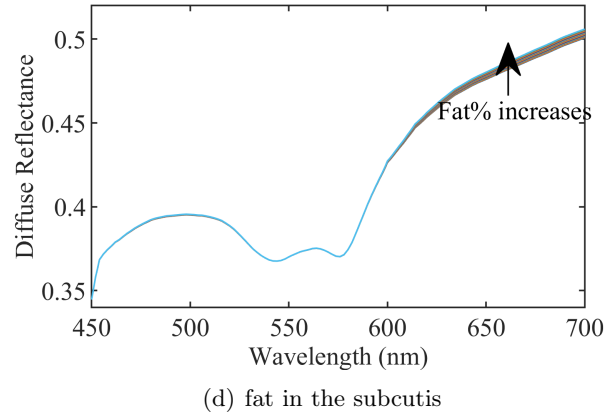
Figure 3.10: Diffuse reflectance reconstructed by increasing water, fat, $\beta-$carotene and bilirubin concentrations.

3.4.3.1   Validation using Data Generated by MC Simulations

To validate our methods, we first use the total diffuse reflectance spectra generated by MC simulations. There three groups: (1) lightly, (2) moderately and (3) darkly pigmented groups for experiments. For each group, we have generated 10 samples which contain the diffuse reflectance spectra and physiological skin parameters by randomly defining inputs and using MC simulations. The average values of RMSE for three groups using 2L-FANN are 0.0027, 0.0036, and 0.0062 for group1, group2, and group3 respectively. And 3L-FANN has almost the same performance. Its average values of RMSE are 0.0033, 0.0037, and 0.0061.

Although our methods give favorable results in regression, in order to extract or quantify physiological parameters, the inverse problem is undoubtedly more important. In other words, our methods need to fit the diffuse reflectance curve precisely without knowing those parameters. By adjusting the inputs iteratively, the difference between the targeted and reconstructed diffuse reflectance decreases until reaching the limits of the optimization process. In our research, RMSE is adopted as this difference. Besides, the interior-point algorithm is selected to minimize RMSE. The maximum number of iterations is assigned to 1000. The initial physiological parameters are randomly set within the proper range and 5 start points are arranged. This optimization process is carried out for all groups with 5 uniformly assigned start points. Figure.3.11 shows the details of the extracting process.

We firstly focus on the results of 2L-ANN. For group1, it can obtain satisfactory estimations for the volume fraction of melanin and blood, the oxygen saturation, and the thickness of two layers. Yet not every parameter can be predicted precisely. The rest parameters are not estimated with acceptable errors. The prediction error for the volume fraction of water in the dermis reaches a maximum of nearly 30%. The error becomes larger for $\beta-$carotene and bilirubin. In view of the absorption coefficients of these pigments, for example, water is less weighted and has less impact on the diffuse reflectance spectra although its volume fraction is large enough. By contrast, melanin and hemoglobin dominate the light absorption within the skin. The situation is similar in group2 and group3. Another key point to remember is
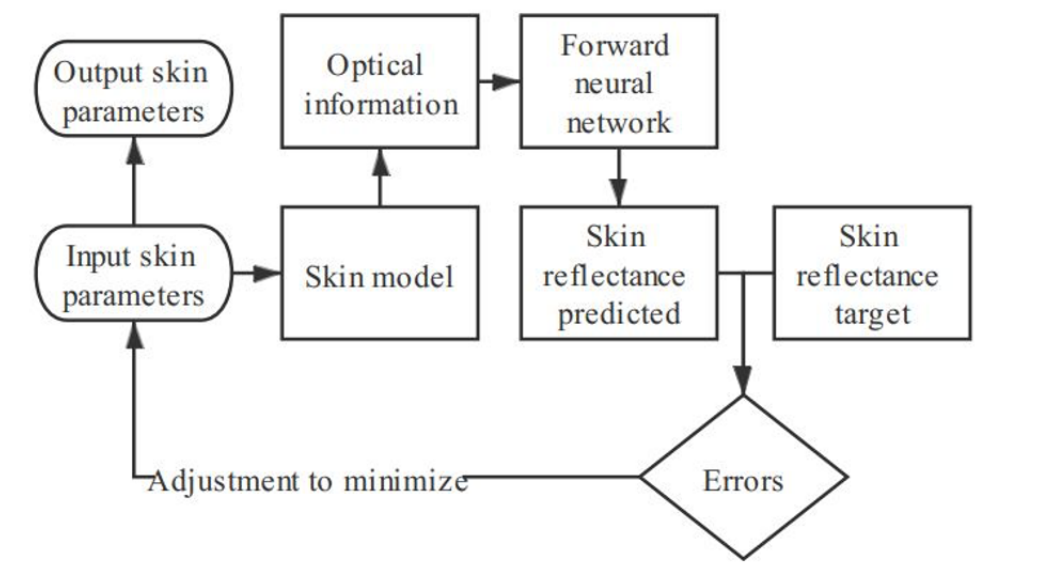
Figure 3.11: Flowchart of the extracting physiological parameters

that the estimation of the ratio between pheomelanin and eumelanin becomes more accurate when the volume fraction of melanin increases. To put it another way, the more dominant melanin volume fraction is, the more difference the reflectance shows due to the ratio. The average relative error of $ratio_{pheo\_eu}$ is reduced to almost 5% for group3. Moreover, the thickness of each layer can be also estimated correctly with the average relative errors 1.11%, 4.80% for d_{epi} and d_{der} respectively. Table 3.4 reveals some estimations results using 2L-FANN. Sample no.1, no.2 and no.3 belong to group1, sample no.11, no.12 and no.13 belong to group2, and the last three samples belong to group3. The average relative errors of C_m, C_{bl_der}, S for the whole group1, 2, 3 are 1.90%, 8.55% and 3.03%. Note that the targeted diffuse reflectance are not the same for 2L-FANN and 3L-FANN since MC simulations are executed based on two-layered and three-layered skin models separately. Additionally, the average RMSE for 30 samples equals 0.0032 using 2L-FANN in the extracting process.

Table 3.5 shows the estimation results using 3L-FANN. As we can see, it has a similar estimation performance to 2L-FANN. The average relative errors of C_m, C_{bl_der}, S for the whole group using 3L-FANN are 1.36%, 8.69% and 3.37%. It is worth noting that the estimation for d_{der} gets even worse. This may be because the

dermis is the middle layer, and the situation is more complicated for the scattering and the absorption. The extra 4 parameters C_{water_sub}, C_{bl_sub}, C_{fat} and d_{sub} can be derived when using three-layered model, however, only C_{bl_sub} and C_{fat} have acceptable estimations with less than 10% errors. The average RMSE for 30 samples equals 0.0078 using 3L-FANN in the extracting process. This inverse extracting process to fit the diffuse reflectance curve and quantify physiological parameters costs an average of 17 seconds to finish. Given that Monte Carlo needs roughly 332 seconds to reconstruct a spectrum and FANN needs only 0.019 seconds in our experimentation, using Inverse Monte Carlo probably needs dozens of hours to finish the task. So it's quite faster using proposed FANNs.

Table 3.4: Fitting results of 2L-FANN for 3 samples in each group.

		C_m	$ratio_{pheo\_eu}$	C_{water_epi}	C_{water_der}	C_{bl_der}	S	d_{epi}	d_{der}
Sample no.1	Optimized	0.0252	0.0937	0.1497	0.5597	0.0637	0.6477	0.0107	0.2601
	Target	0.0251	0.1698	0.1712	0.4724	0.0672	0.6510	0.0108	0.2836
Sample no.2	Optimized	0.0202	0.1774	0.1510	0.6724	0.0201	0.6222	0.0120	0.0813
	Target	0.0202	0.2180	0.1687	0.5456	0.0204	0.6261	0.0121	0.0814
Sample no.3	Optimized	0.0193	0.2535	0.1493	0.7057	0.0168	0.9416	0.0058	0.0755
	Target	0.0176	0.3109	0.1226	0.4197	0.0170	0.9498	0.0057	0.0765
Sample no.11	Optimized	0.1558	0.1125	0.1532	0.4422	0.0060	0.6441	0.0128	0.0827
	Target	0.1563	0.0870	0.1337	0.6185	0.0064	0.5362	0.0124	0.0792
Sample no.12	Optimized	0.1248	0.1569	0.1497	0.7914	0.0220	0.6175	0.0093	0.2570
	Target	0.1244	0.1374	0.1265	0.8652	0.0217	0.6136	0.0093	0.2475
Sample no.13	Optimized	0.1222	0.2509	0.1496	0.7791	0.0381	0.8503	0.0130	0.2629
	Target	0.1218	0.2471	0.1420	0.8432	0.0387	0.8658	0.0131	0.2533
Sample no.21	Optimized	0.2839	0.3500	0.1508	0.8518	0.0108	0.8256	0.0118	0.2543
	Target	0.2865	0.3534	0.1607	0.7400	0.0102	0.8854	0.0117	0.2627
Sample no.22	Optimized	0.2441	0.1498	0.1500	0.6494	0.0531	0.7010	0.0146	0.2330
	Target	0.2449	0.1654	0.1839	0.4049	0.0537	0.6209	0.0145	0.2556
Sample no.23	Optimized	0.3109	0.3180	0.1492	0.6154	0.0555	0.8524	0.0080	0.1830
	Target	0.3097	0.3250	0.1175	0.7580	0.0543	0.8727	0.0082	0.1843

Table 3.5: Fitting results of 3L-FANN for one sample in each group.

		C_m	$ratio_{pheo\_eu}$	C_{water_epi}	C_{water_der}	C_{water_sub}	C_{bl_der}
Sample no.1	Optimized	0.0252	0.0670	0.1494	0.5525	0.6657	0.0621
	Target	0.0251	0.1698	0.1712	0.4724	0.8811	0.0672
Sample no.11	Optimized	0.1583	0.1128	0.1500	0.5116	0.6370	0.0062
	Target	0.1563	0.0870	0.1337	0.6185	0.7512	0.0064
Sample no.21	Optimized	0.2866	0.3405	0.1501	0.6675	0.7775	0.0124
	Target	0.2865	0.3534	0.1607	0.7400	0.8396	0.0102
		C_{bl_sub}	S	C_{fat}	d_{epi}	d_{der}	d_{sub}
Sample no.1	Optimized	0.0712	0.6498	0.5518	0.0107	0.2522	0.2077
	Target	0.0955	0.6510	0.4865	0.0108	0.2836	0.2381
Sample no.11	Optimized	0.0901	0.6370	0.5468	0.0122	0.0716	0.3022
	Target	0.0560	0.5362	0.4540	0.0124	0.0792	0.2471
Sample no.21	Optimized	0.0979	0.8249	0.5472	0.0113	0.1658	0.4851
	Target	0.0871	0.8854	0.4995	0.0117	0.2627	0.2153

3.4.3.2   Validation using Data Measured

Our methods extract several physiological skin parameters successfully from the synthetic diffuse reflectance, the next step is to extract these parameters from the measured diffuse reflectance data. NIST skin reflectance database is used in this part [113]. The spectra were acquired with a commercially available spectrophotometer with help of integrating sphere and this database contains 100 samples with spanning the wavelength range from 250 to 2500 nm. These samples were reshaped using the interpolation algorithm and only the range from 450 to 700 nm is saved for further uses. Afterward, the curve-fitting process is applied and the optimization goal is to minimize RMSE. Figure.3.12 depicts the flowchart of the extraction process. First, the measured reflectance is analyzed in two ways. The skin parameters and RMSE are then calculated for both two-layered and three-layered models in order to suit different situations. For example, if the upper two layers are strongly light-absorbed, it is possible that 2-layered model works better. Skin parameters with better fitting performance are selected as final results, in other words, we compared RMSE for two skin models and then output the results with less RMSE. Furthermore, we only take the oxygen saturation and the volume fraction of melanin and blood as the outputs because these three parameters can be estimated more accurately.

Table 3.6 provides the extraction results for three samples from NIST skin reflectance database and Figure.3.13 illustrates the spectra reconstructed by two methods coupled with the raw measured spectra. As we can see, 2L-FANN and 3L-FANN obtain approximate values and fitting performance. For sample a, the volume fraction of melanin reaches nearly 10% which assuredly matches the spectra with low reflectance. For the rest two samples, C_m are estimated as 3.23% and 1.31% respectively, which also matches well the spectra. In this visible light range, the diffuse reflectance of sample c is evenly higher than sample b. What'more, the small RMSE value indicates that the curve-fitting process works properly. In our experimentation, the options of the optimization stay always the same. The networks are robust, and they can obtain similar answers starting from different initial points. Another key point to remember is that the optimization method would also affect accuracy.

Table 3.6: The extractiong results of 2L-FANN and 3L-FANN

Sample	Methods	C_m	C_{bl_der}	S	$RMSE$
a	2L-ANN	9.79%	6.99%	80.02%	8.37%
	3L-ANN	10.09%	7.00%	80.00%	10.76%
b	2L-ANN	3.69%	1.08%	94.91%	5.69%
	3L-ANN	3.23%	1.02%	94.95%	4.27%
c	2L-ANN	2.13%	0.54%	90.45%	3.28%
	3L-ANN	1.31%	0.56%	90.23%	2.08%

It is a potential way by changing the optimization methods because FANNs derive skin parameters in cooperation with the optimization and both may affect the final results.
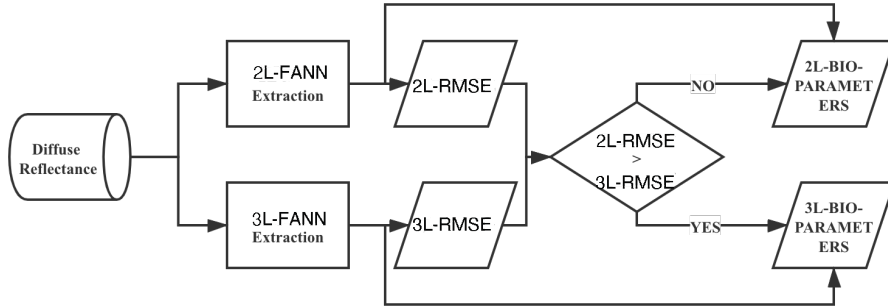
Figure 3.12: The flowchart of the physiological parameters extraction with two skin models

3.5   Discussion and Conclusion

Our research gives a quantitative analysis of skin based on diffuse reflectance. MC method is recoded in Python and tested by comparing the simulation results to other versions. Both two-layered and three-layered skin models are involved. FANNs have been built and trained to solve the extraction problem. The absorption of skin is influenced under the combination of various pigments and the thickness of layers. The effects of skin parameters are analyzed separately. The results present that 2L-FANN and 3L-FANN have indeed excellent fitting performance in synthetic data
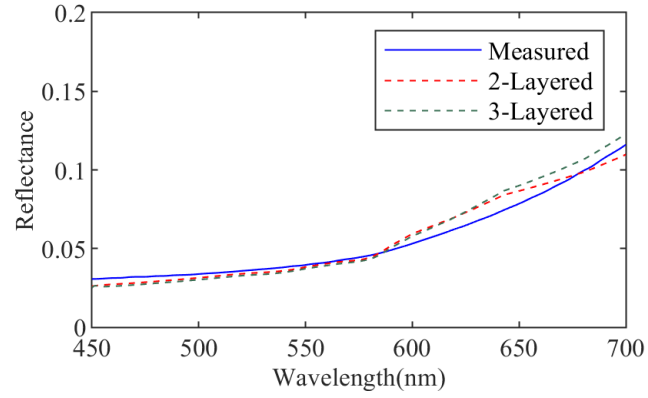
(a) sample a
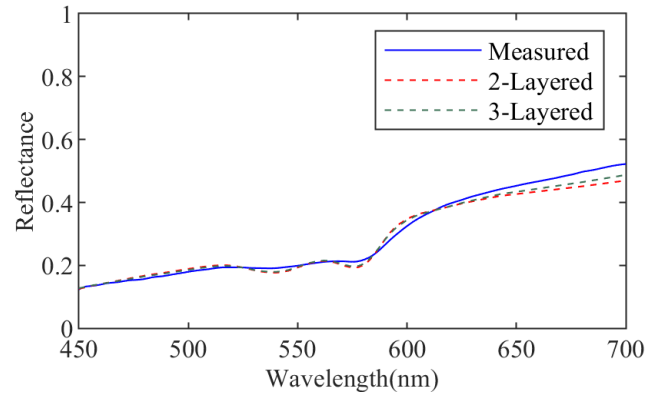
(b) sample b
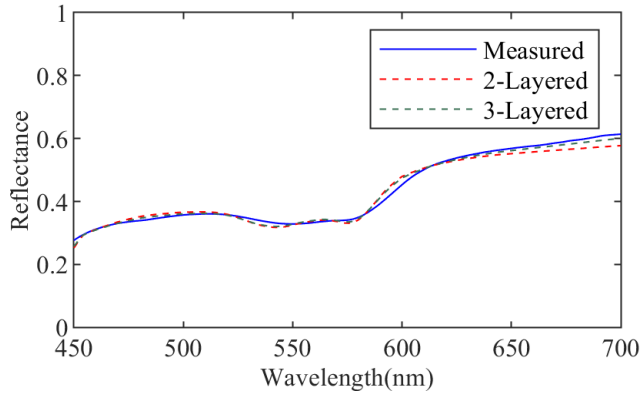
(c) sample c

Figure 3.13: Diffuse reflectance reconstructed compared to the measured one in extracting process.

generated by MC simulations. When it comes to the measured data, the fitting performance is also acceptable. The selection between 2L-FANN and 3L-FANN are evaluated by comparing RMSE values. The visible light range from 450 to 700 nm

are taken into account in our research. As we know, long-wavelength light generally has better penetration capacity[114]. When light penetrates deeper, 3L-FANN usually works better than 2L-FANN. Taking our experimentation as examples, the volume fraction of melanin and blood for sample a are extracted nearly 10% and 7%. The large volume fraction means strong absorption. When light is totally absorbed in the first two layers, this may cause that the RMSE value of 3L-FANN surpasses that of 2L-FANN, in other words, 2L-FANN has a better fitting performance than 3L-FANN at this time. As for sample b and c, 3L-FANN becomes the better method due to the less volume fraction of melanin and blood. Besides this, the thickness of layers should also be considered. The thicker the skin, the less likely light will penetrate.

Our methods prove acceptable extraction results for the volume fraction of melanin, blood and oxygen saturation. A large training database is created by MC simulations to ensure no over-fitting. Compared with the existing research, due to the simplicity of the analytical solutions, DA is widely used in non-invasive detection of biological tissue with help of DRS. However, the relative errors of C_m and C_{bl_der} reaches 17.3% and 13.0% using DA to fit MC simulations [88]. On the other hand, our methods are more accurate with the average relative errors of C_m and C_{bl_der} less than 2.0% and 9.0%. Note that the relative error may become too large when the original values are low, such as C_m in group1. It's necessary to introduce new metrics to address outliers in follow-up work. The extracting process costs much less time than inverse MC once networks have been trained. Two models are carried out parallelly and RMSE is the metric to select the better fitting results. The wavelength range is directly fixed from 450 to 700 nm in our research, which means the selection of wavelength range could be applied in future work. Nowadays many studies apply separated source-detector systems to collect diffuse reflectance, thanks to wearable equipment. However, our research focuses on the total diffuse reflectance, which means less convenient to acquire the measured data. The hyper-spectral imaging system with linescan HSI sensor (imec SNAPSCAN VNIR) will aid to collect raw data. And then these methods will be implemented for detecting physiological skin parameters, and diagnosing skin diseases non-invasively in the

future.

Fast Determination of Melanin Volume Fraction based on Skin Diffuse Reflectance

Contents

A three-layered skin model is built to simulate diffuse reflectance using Monte Carlo simulations based on biological components, which include melanin volume fraction, water level, blood volume fraction, oxygen saturation, etc. A forward neural network is trained for mapping biological components and reflectance. Then a database, which contains 50,000 samples hyperspectral diffuse reflectance spectra from 450 to 750 nm (1 nm interval) with randomly given biological components information, is generated by this forward neural network. Support vector regression, inverse neural network and random forest are applied for the regression analysis of reflectance data and melanin volume fraction. Dimensionality reduction is used to accelerate the training time. The performances of three regression methods are measured and show promising prediction results.

Chapter 4. Fast Determination of Melanin Volume Fraction based on Skin Diffuse Reflectance

4.1 Introduction

Hyperspectral imaging techniques, which collect information from the whole spectra with a narrow interval (generally 1-20 nm), have become more mature and attracted more attention, benefiting from its high resolution and ability to extract the inner information from biological tissues. It is developed originally for mining and geology as hyperspectral remote sensing, and then it is applied to other fields, such as agriculture, astronomy, chemical imaging and surveillance. Due to the acquisition of every spectral band at a single point, it allows us to research on the entire spectrum. However, it suffers from cost and complexity because of expensive specialized monochromatic sensors. With the development of hyperspectral sensors and scanning techniques, low-cost and compact sensors were designed with high-resolution up to 0.8 nm[115].

Human skin, which is the largest organ of the integumentary system, indicates the health of the human body. Skin diseases, such as melanoma, erythema and vitiligo, vary in symptoms and severity. Some of them have minor effects, and others can be dangerous with high death rate[15]. This leads to a fast growing for the determination of biological components within skin tissue. The two most important biological components, which dominant the formation of skin appearance under light-skin interaction, are melanin and hemoglobin. So far, a large amount of research are focusing on analyzing the methods which explain light-skin interaction based on hyperspectral diffuse reflectance. Monte Carlo simulation (MC) among these methods is always considered as the baseline for validation. It exploits random number generator for simulating the movements of photons with probability density functions[69]. Other methods, like diffusion approximation (DA) and Kubelka-Munk theory (KM), give the enclosed analytical solutions of reflectance and transmittance from radiative transfer equation (RTE) or based on the assumption that only two light flux channels traveling in opposite directions exist within skin tissue[116, 117]. Recently, machine learning methods are used for interpreting light-skin interaction because of favorable performance when dealing with data in regression. All these methods applied for the determination of biological components can be divided into

two categories: direct and indirect methods based on the direction of mapping. MC, DA, KM, forward neural networks (FANN) etc. are indirect methods because they calculate reflectance spectra from predefined physiological parameters and then a curve-fitting process is used to find the best diffuse reflectance spectra of which the parameters are estimation results. Fredriksson *et al.* used MC to improve spectral fitting based on spectra from two source-detector distances (0.4 and 1.2 mm) and a multilayered skin model[83]. However, it is still time-consuming for retrieving parameters using MC. DA was analyzed for the inverse analysis of skin reflectance spectra in terms of its suitability and it turns out that this method is simple and robust for monitoring physiological changes in skin. In contrast, it has up to 15% errors in predicting blood and melanin volume fraction[88]. Wang *et al.* replaced MC by FANN to speed up for calculations of reflectance spectra and fitting procedure[99]. The accuracy of this approach concerns the curve-fitting process, such as the selection of start points and the computational time also depends mainly on fitting. Direct methods, like inverse neural networks (IANN), obtain results derived directly from reflectance spectra. These methods are usually efficient once trained. Vyas *et al.* built a computational model based on support vector regression (SVR) to extract physiological parameters[118]. However, the training database generated by KM is based on a simple skin model including only three parameters. An IANN trained with help of MC was put forward by Zhang *et al.*, but there are only 32 samples of MC for training[7]. Besides, direct methods suffer from higher errors and less robustness compared to indirect methods.

In our research, a novel direct scheme based on a three-layered skin model was evaluated. IANN, random forest (RF) and SVR were applied to analyze the reflectance spectra. The first database (D1) including skin optical parameters and the corresponding reflectance at a single wavelength was generated by GPU-based accelerated MC simulations[119] since MC is considered as the gold standard method. Then a FANN was trained by D1 and used for generating the second database (D2) including physiological skin parameters and the corresponding spectra from 450 to 750 nm in the purpose of acceleration due to that GPU-based MC still costs much time in reconstructing the whole spectra while neural work is almost 1000

times faster[98]. Then three direct regression methods as we mentioned above were trained by D2 to extract melanin volume fraction. Given the different pigmented degrees of human skin, our methods were tested and compared in lightly pigmented, moderately pigmented and darkly pigmented skin groups separately[120]. Finally, they were tested on the reflectance spectra measured. The results show that the proposed methods can fast determine melanin volume fraction compared to the existing research and have acceptable errors.

4.2   Skin Model and Database

Skin is considered as a three-layered structure: the epidermis, the dermis and the subcutis as we presented in Chapter 3. And the physiological parameters which are proved to be less important are abandoned, such as $\beta-$carotene and bilirubin. The absorption and scattering coefficients are calculated in the similar way.

In total 50000 samples of skin parameters are taken randomly within their proper ranges to generate D1 using GPU-based MC, and the wavelength is selected also randomly from 450 to 750 nm. It takes 15.6 hours to run MC simulations with 1E07 photons per iteration in order to generate the first database. D1 is composed of 14 elements: 12 skin parameters, wavelength λ and reflectance R_λ. All elements are in size 1×50000. Note that the reason why we expand the wavelength range is because the measured absorption coefficients for $\beta-$carotene and bilirubin are restricted, after abandoning them, we can apply larger ranges.

A FANN is then trained by D1 with its structure: 2 hidden layers including 55 neurons. The inputs are 12 skin parameters and the wavelength, and the output is the corresponding reflectance. MSE is used to evaluate the performance, and it eventually reaches 6.01E-08, which proves that this network can approximate MC well. Figure.4.1 illustrates the reconstructed reflectance spectra derived from the same skin parameters using MC and FANN. To build a database for training our direct methods, it still needs another step, that is to say, we take randomly 50000 samples of skin parameters again. Then, the entire reflectance spectrum from 450 to 750 nm (301 dimensions) for each sample, rather than only one spectral band

in D1, are generated by FANN. This time we obtain the second database within about 4.3 hours. D2 is also composed of 13 elements: 12 skin parameters with size 1×50000 and reflectance over 450-750 nm $R_{450-750nm}$ with size 301×50000. To make it clear, database generation process is illustrated in Figure 4.2. Next IANN, SVR and RF based on LSBoost are trained by D2 and used for fast determination of melanin volume fraction, which is the most dominant pigment in the formation of skin reflectance and related to life-threatening melanoma.
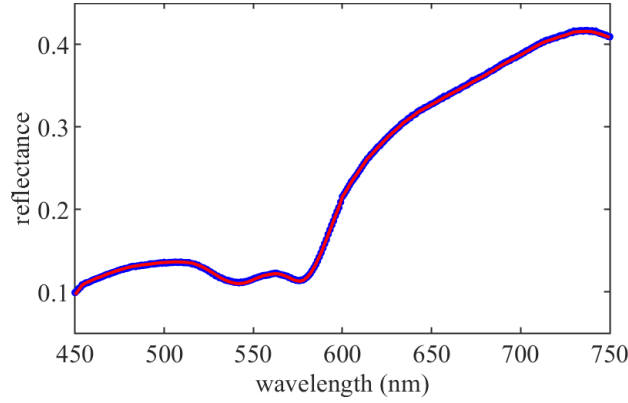
Figure 4.1: Reconstructed reflectance spectra using MC (red line) and FANN (blue line)

4.3 Experimentation and Results

Since IANN, SVR, and RF are used as direct methods, the inputs for training are changed to the reflectance over 450-750 nm, and the output is melanin volume fraction. D2 is divided into three parts: training (70%), test (15%), and validation (%15) for IANN. 10-fold cross validation is adopted for SVR and RF to avoid over-fitting and selection bias. The structure of IANN is also defined as 2 hidden layers with 55 neurons. The kernel function of SVR is set "Gaussian" and the algorithm of RF is set "LSBoost" for regression. The experimentation is carried out in MATLAB R2018a using deep learning and machine learning toolbox with i7-7700HQ CPU (2.80 GHz) and NVIDIA GeForce GTX 1060 GPU (Max-Q Design). Performances of our three methods are 0.0082 for IANN, 0.0189 for SVR, and 0.0174 for RF. Moreover, considering that melanin varies among individuals, lightly pigmented
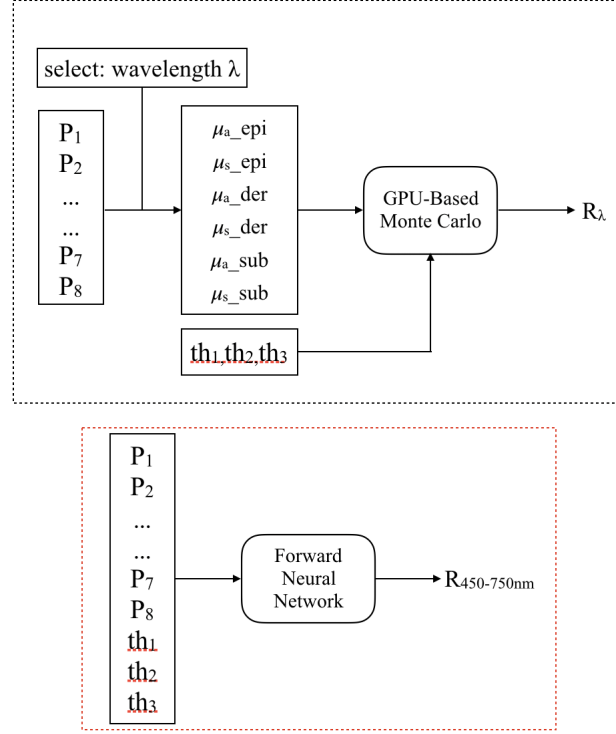
Figure 4.2: Flowchart of database generation process (50000 iterations): R_λ is the reflectance at wavelength λ. All 12 skin parameters, λ and R_λ are stored in D1 (black dotted frame); $R_{450-750nm}$ is a vector, which indicates the reflectance over 450-750 nm, is stored in D2 together with 12 skin parameters (red dotted frame).

$(P_1 \in [1.3\%, 3\%])$, moderately pigmented $(P_1 \in [11\%, 16\%])$, and darkly pigmented $(P_1 \in [18\%, 43\%])$ in total 3 skin types are separately validated for comparisons.

4.3.1 Validation with Synthetic Spectra

We have created 10 samples of reflectance spectra for each skin type using MC simulations, which are used as the first validation data. These 30 samples in total are analyzed respectively by IANN, SVR, and RF for extracting melanin volume fraction. Table 4.3.1 gives determination results of melanin volume fraction for lightly pigmented skin. The root-mean-square errors (RMSE) of RF, IANN, and SVR are 0.48%, 0.30%, and 4.47% respectively. And the standard deviations (STD) of errors are 0.47%, 0.30% and 1.33%. It turns out that IANN is the best method for estimating melanin volume fraction in lightly pigmented skin group among these

three. It has minimum RMSE and STD, which implies more robustness than the other two approaches. RF also performs well in estimating melanin volume fraction, but it takes a longer time than IANN for training especially when using 10-fold cross-validation. SVR cannot extract melanin volume fraction precisely with the largest errors and it needs the longest time for training as well. Given that the melanin volume fraction of lightly pigmented skin varies in a small range from 1.3 to 3%, SVR is not available for this group. As for moderately pigmented skin, results are shown in Table 4.2. RMSE and STD of RF, IANN, and SVR are 1.09%±1.05%, 0.40%±0.39%, 0.99%±0.98% respectively. All methods reach acceptable estimation results considering the range of moderately pigmented skin is from 11% to 16%. Notably, IANN has the best performance again among three methods. For the third group darkly pigmented skin, RMSE and STD of RF, IANN, and SVR are 3.90%±3.85%, 2.00%±1.93%, 2.48%±2.47%. The favorable results confirm that our methods extract accurately melanin volume fraction. And once again, IANN works better than the other two methods. We also evaluate the relative errors among three skin types, and for lightly pigmented skin, they are 21.28% using RF, 12.55% using IANN, and 223.5% using SVR. For moderately pigmented skin, they are 7.40%, 2.52%, and 6.36%. For darkly pigmented skin, they are 5.71%, 3.01%, and 4.54%. Given that the target melanin volume fraction for lightly pigmented skin is too low, this causes the relative errors being extremely large even with a small deviation. Note that these direct methods are trained by a synthetic database, and the relative errors will be further enlarged when dealing with the measured data since noise signals are very common. To sum up, IANN predicts the most accurate results for all three skin types most of the time. RF and SVR provides acceptable results as well. However, SVR is not reliable when extracting melanin volume fraction from lightly pigmented skin.

Table 4.1: Melanin[%] Determination results of proposed direct methods for lightly pigmented skin type

Samples	no.1	no.2	no.3	no.4	no.5	no.6	no.7	no.8	no.9	no.10
Target	2.51	2.02	1.76	1.85	2.26	1.74	1.96	1.88	2.79	1.47
RF	1.98	2.08	1.63	2.33	1.65	1.04	2.65	1.31	3.11	1.63
IANN	2.30	1.78	2.13	1.88	2.41	1.67	1.66	1.30	3.24	1.32
SVR	4.93	7.40	7.85	3.91	6.40	5.97	6.17	7.83	5.87	6.54

Table 4.2: Melanin[%] Determination results of proposed direct methods for moderately pigmented skin type

Samples	no.11	no.12	no.13	no.14	no.15	no.16	no.17	no.18	no.19	no.20
Target	15.63	12.44	12.18	13.01	13.82	13.48	11.24	14.28	14.45	11.43
RF	15.94	11.56	12.92	12.49	12.77	14.93	13.32	14.24	13.61	12.80
IANN	15.72	12.59	12.28	12.60	13.77	13.64	12.10	13.89	14.05	11.98
SVR	15.45	12.76	12.30	11.77	12.86	13.30	12.35	15.96	13.66	9.82

Table 4.3: Melanin[%] Determination results of proposed direct methods for darkly pigmented skin type

Samples	no.21	no.22	no.23	no.24	no.25	no.26	no.27	no.28	no.29	no.30
Target	28.65	24.49	30.97	19.79	36.19	39.78	27.24	28.35	22.17	37.46
RF	28.86	24.67	30.70	19.50	35.68	28.33	27.64	32.53	23.00	38.62
IANN	28.64	24.01	30.73	19.28	36.14	33.88	27.02	30.42	22.02	37.83
SVR	27.37	24.73	30.98	19.36	36.48	33.20	28.43	32.11	22.02	38.24

4.3.2 Dimensionality Reduction

Considering that only melanin volume fraction is extracted in our research, we decide to select the spectral bands where melanin affects the most. Melanin can be divided into two types: the brown-black eumelanin and the yellowish-reddish pheomelanin. Their absorption coefficients are a little different, in other words, the absorption coefficient of eumelanin is a little larger than pheomelanin. The ratio between the concentration of pheomelanin and eumelanin is set randomly in the range from 4.9 to 36%[107]. Generally, the absorption coefficient of melanin is larger than other absorbers and it gradually decreases from 450-750 nm as we mentioned in the Chapter 3. Another important absorber is hemoglobin, which can also be divided into two types: oxy-hemoglobin and deoxy-hemoglobin[14]. We find that the absorption coefficient of hemoglobin surpasses over melanin from nearly 550 to 580 nm. Additionally, the absorption coefficient of oxy-hemoglobin shows an inverse "W" pattern[121], which has been used for skin detection[21]. To avoid the spectral bands where other absorbers affect skin reflectance similarly or more significantly than melanin, a low variance filter (LVF) is then applied to the reflectance spectra in D2. First, the variances of reflectance in D2 is calculated along the spectral bands. That is to say, a 1×301 vector V is returned. Then a threshold is set to filter low-variance variables because the information carried by low-variance variables is generally considered to be very small. The maximum and minimum values of V are 0.0151 and 0.0012. The difference between the maximum and minimum is over one degree of magnitude. A threshold is set 0.01 and all dimensions, of which the variance is below this threshold are removed. Figure.4.3 shows the reflectance filtered and unfiltered. The spectral bands selected locates from nearly 620 to 750 nm. 130 spectral bands are extracted from D2 as new training features. Given that IANN has the best performance in melanin determination validated with MC samples, we apply LVF to speed up the training process of IANN. For the original IANN, it takes 57 min 38 s to complete the training process with 26809 epochs executed. For IANN+LVF, it takes 12 min 12 s to finish the task with 8646 epochs executed. The result shows a significant improvement in computational time. This fusion approach

is also validated by MC samples, and the melanin determination results are shown in Figure 4.4. The RMSE and STD of IANN+LVF are 2.06%±1.51% for lightly pigmented skin, 4.15%±3.60% for moderately pigmented skin, and 4.76%±5.02% for darkly pigmented skin. After applying LVF to IANN, the training speed has been increased by more than 4 times, while the accuracy has been reduced.
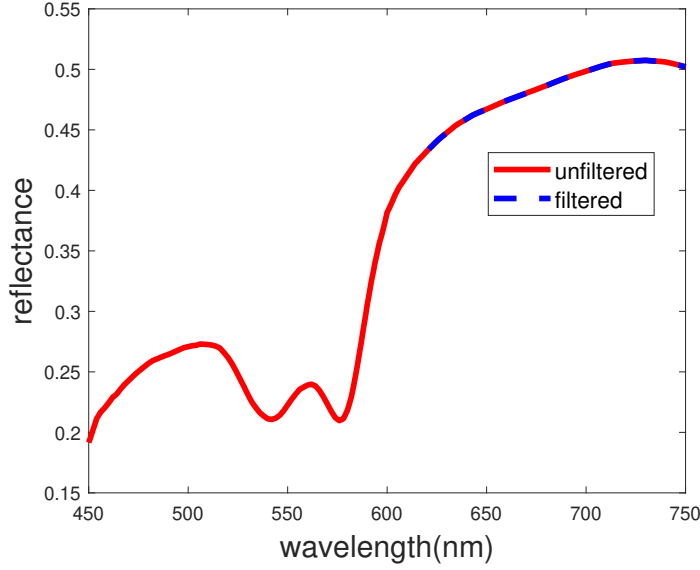
Figure 4.3: Comparison between the reflectance spectra filtered and unfiltered

Except for LVF, principal components analysis (PCA) is also used for reducing dimensionality and speeding up the training. PCA uses orthogonal transformation to linearly transform the observations of a series of possibly related variables, thereby projecting the values of a series of linear unrelated variables. These unrelated variables are called principal components. In our research, we have 50000 observations with 301 variables, represented by a matrix X (301×50000). Then, a principle components matrix Y is defined:

$$
\begin{aligned}
Y^T &= X^T W \\
&= VD^T W^T W \\
&= VD^T
\end{aligned}
\tag{4.1}
$$

where $X = WDV^T$ is the singular value decomposition; W is the eigenvector matrix

92

(a) lightly pigmented

(b) moderately pigmented

(c) darkly pigmented
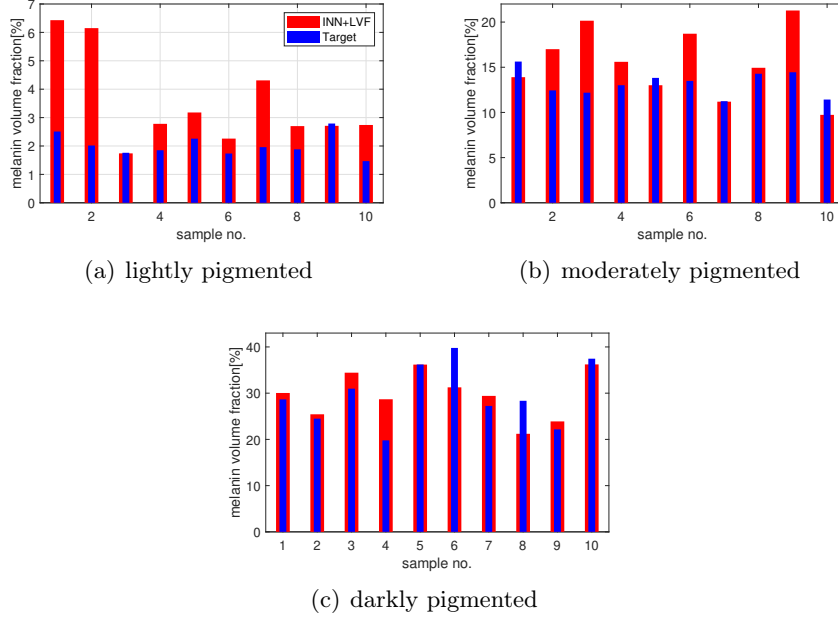
Figure 4.4: Melanin determination results of INN+LVF (histogram).

of 301×301 XX^T; D is a 301×50000 non-negative rectangular diagonal matrix; V is the eigenvector matrix of 50000×50000 $X^T X$. We calculate the influence of every principal component and find that the first seven principal components account for above 99.53%. Then, a data matrix X is transformed to a matrix 7×50000 with reduced dimensionality. Based on this low-dimension matrix, we have retrained IANN again. And the training time, which equals 10 min 35 s, is once again accelerated with better performance than IANN+LVF. The RMSE and STD results are shown in Table 4.3.2. For all skin types, IANN+PCA shows great performance just like original IANN, and is much better than IANN+LVF. And the Pearson product-moment correlation coefficient of the estimated and target melanin volume fraction for IANN+PCA equals 0.99663. While maintaining high accuracy, its training time has also been greatly shortened, five times faster than original IANN.

Table 4.4: RMSE and STD of IANN, IANN+LVF and IANN+PCA in 3 groups

	RMSE(lightly)	STD(lightly)
IANN	0.3%	0.3%
IANN+LVF	2.06%	1.51%
IANN+PCA	0.21%	0.42%
	RMSE(moderately)	STD(moderately)
IANN	0.4%	0.39%
IANN+LVF	4.15%	3.6%
IANN+PCA	0.5%	1.34%
	RMSE(darkly)	STD(darkly)
IANN	2%	1.93%
IANN+LVF	4.76%	5.02%
IANN+PCA	2.33%	5.6%

4.3.3 Validation with Measured Spectra

To our best knowledge, there is not a public database which contains skin reflectance spectra and the corresponding physiological parameters simultaneously. Most of the researchers compare their approaches to MC when dealing with measured spectra. A human skin database from NIST are used in our research[113]. This database contains 100 reference reflectance spectra of human skin, spanning the spectral region from 250 to 2500 nm with 3 nm resolution. For better adaption to our methods, all diffuse reflectance spectra are resized to the spectra region from 450 to 750 nm with 1 nm resolution using the interpolation algorithm. IANN, IANN+LVF and IANN+PCA are used to extract melanin volume fraction compared with MC. Due to that MC is an indirect method, a curve-fitting algorithm is required to help MC obtain results. A global research method with multi-start-points is adopted. Several results are presented in Table 4.5. We can see that melanin volume fractions are quite close with errors less than 5% compared to MC. Figure 4.5 illustrate these 3 spectra used for validation. The estimation results match well the fact: the larger melanin volume fraction is, the lower reflectance becomes. Additionally, the "W" pattern as we mentioned above becomes unnoticeable when melanin volume fraction is large enough. Compared to indirect methods, our methods can fast determine melanin volume fraction, however, it is not flexible because the inputs are restricted to a 301 dimensions spectrum. Indirect methods use the output reflectance to fit

Table 4.5: Melanin volume fraction extracting from 3 diffuse reflectance spectra

	Spectrum 1	Spectrum 2	Spectrum 3
IANN	1.84%	2.90%	10.69%
IANN+LVF	1.90%	4.70%	14.26%
IANN+PCA	1.72%	2.87%	13.40%
MC+Curve-fitting	1.31%	3.78%	10.73%

the measured reflectance spectrum, and iterate this process for the best fitting performance. That is to say, indirect methods are generally more robust than direct methods.
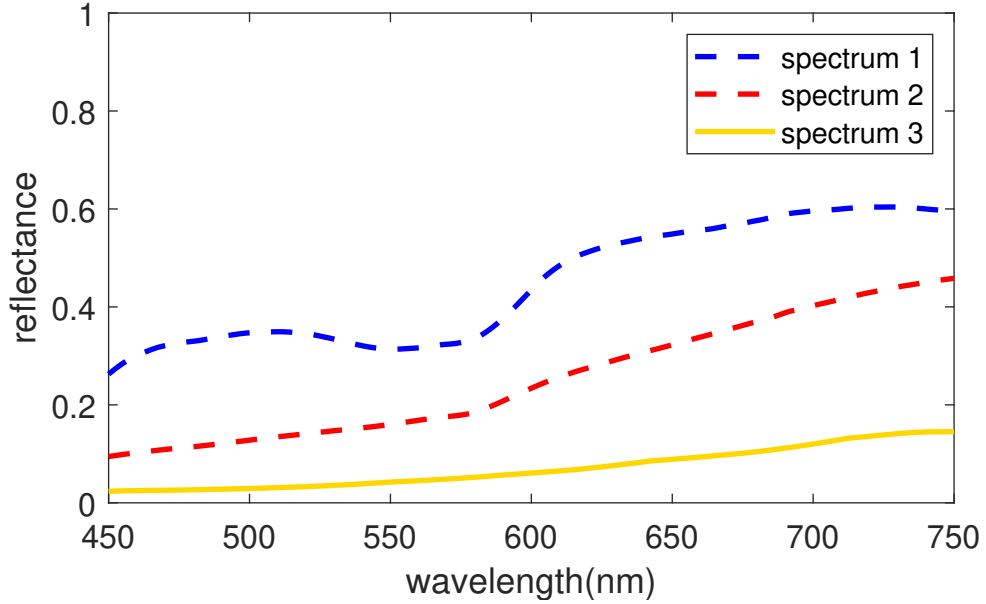
Figure 4.5: Three measured diffuse reflectance spectra in NIST

4.4 Conclusion

Our research focus mainly on fast determination for melanin volume fraction. It is related to several skin diseases, such as melanoma and vitiligo, which seriously affect the normal lifestyle of victims. A synthetic reflectance spectra database based on a 3-layered skin model is generated by FANN instead of MC to speed up because MC is not efficient even that it can be accelerated by GPU technique. Under our experi-

mental conditions, it takes about 37 s to construct a diffuse reflectance spectrum for GPU-based MC, meanwhile, only 19.4 ms for FANN. Three direct methods are evaluated and compared. IANN has the best performance in estimating melanin volume fraction. Due to that RF consists of a large amount of decision trees, which means taking up a huge space to store, it is not suitable for implementation although it has good performance. Moreover, a dimensionality reduction filter and PCA method are applied to further speed up the training process of IANN. All methods are first validated on synthetic spectra samples in three skin types, and then compared to MC using measured spectra samples. The RMSE and STD are favorable and less than 5% compared to MC. IANN+LVF and IANN+PCA can obtain satisfactory results compared to IANN and they are faster for training. Moreover, PCA works better for reducing dimensionality than LVF since it has a similar accuracy to IANN and the least training time. Compared with the indirect methods, our proposed method is faster, and based on previous research results, the database used for training is increased to solve the problem of over-fitting. In addition, since it does not require an iterative curve fitting process, this direct method can quickly extract melanin volume fraction (FANN needs about 20s, IANN only needs 0.012s). Our future work is to collect hyperspectral images of skin and implement IANN to analyze them non-invasively and in real time. Furthermore, we plan to design a weighted fusion of different methods or based on different spectral bands to improve the robustness of our approach.

Auxiliary Method based on Hyperspectral Reflectance for Presentation Attack Detection

Contents

Face recognition has reached a high accuracy in recent years by adopting convolutional neural networks. However, it suffers from presentation attacks such as 2D face photos, and 3D masks. The vulnerability of face recognition and presentation attacks detection (PAD) attract numerous researchers in recent years. Most studies have only focused on PAD algorithms by analyzing texture information, depth information or thermal images. On the other hand, hyperspectral reflectance, which benefits from the development of line-scan HSI sensors, makes it possible to detect information about the inner structure of materials. Our research proposes an auxiliary method to support face recognition by analyzing hyperspectral reflectance. Combined with biological facts of human skin, we trained a neural network with pigmentation fractions inside human skin and corresponding reflectance. The results show high accuracy in identifying skin and non-skin.

5.1   Introduction

Face recognition is widely used in biometric domain considering its nearly perfect performance. This technique brings much convenience to people's daily life, such as entrance authentication, or paying with your face. The earliest study on face recognition started in the 1950s in psychology and the classification method has evolved from PCA, SVM to ANN [122]. Particularly, deep learning techniques are applied like FaceNet [123], VGG-Face [124], and LightCNN [125]. These face recognition systems achieve high recognition accuracy. However, presentation attacks which can spoof face recognition systems have been developed at the same time and become major security issues. To our best knowledge, the main presentation attacks are printed face photos, face videos and 3D masks of authenticated users.

The vulnerability of face recognition against these spoofing attacks makes PAD especially important. In recent years, PAD has gain increasing interest from researchers in order to guarantee the safety and suitability of face recognition systems. Ramachandra and Busch provided a complete review of face PAD techniques, available databases and extensive analysis on state-of-the-art approaches [126]. Generally speaking, PAD algorithms can be divided into two types in terms of data acquisitions: 2D and 3D. 2D-PAD algorithms aim to identify printed face photos or videos from bona-fide presentations and are separated into three main categories based on the information analyzed: motion analysis, texture analysis, and life sign detection [127]. 3D-PAD algorithms address more complicated information involved with depth and reach higher accuracy while the devices are not cost-effective. A new countermeasure based on foreground and background motion correlation together with the optical flow is tested on PHOTO-ATTACK database and reaches an equal-error rate of 1.52% [128]. Based on wavelet, Wild et al. propose an approach that extracts texture information from the grey level co-occurrence matrix of face photos for liveness detection without installing any extra equipment [129]. Some research considering eyes blinking, head movement or dynamic frequency information as visual rhythms [130], also shows a good performance in PAD. Wen et al. study on an efficient and robust PAD algorithm based on image distortion analysis to sepa-

rate genuine and spoof faces [131]. Despite these significant progress, presentation attacks techniques are also changing rapidly. With the appearance of custom made face masks and deepfake videos trained by generative adversarial network [132], PAD meets new challenges. Recent study shows that CNN based face recognition systems are vulnerable to custom silicone masks [133] and several PAD techniques are validated on custom masks database [134].

On the other hand, spectral reflectance is an efficient indicator to detect presentation attacks due to its differences among materials. Zhang et al. propose a novel liveness detection method by analyzing multispectral reflectance based on the Lambertian model [135]. Two spectral bands 850nm and 1450nm are chosen to differentiate genuine faces and artefacts. Furthermore, Kose and Dugelay decompose the image into illumination and reflectance components using the variational retinex algorithm, then the reflectance component is reshaped as a feature vector for classification [136]. Since existing research only considers several independent spectral bands and the differences between genuine faces and artefacts in long-wavelength bands especially NIR, we propose a novel method derived from light-skin interaction and skin structure. A skin model has been built in the viewpoint of tissue optics. Subsequently, skin hyperspectral reflectance (SHSR) database was generated by Monte-Carlo simulations and a skin-network was trained. By fitting the reflectance curve over the ensemble of spectral bands of objects and analyzing the performance, we can identify if they are real skin or not.

5.2 Skin Model and Database

To accelerate this method, we consider skin as a 2-layered structure: epidermis and dermis. The definitions of both absorption and scattering coefficients are the same as shown in Chapter 3. Also, the less important pigments are ignored, such as $\beta-$carotene and bilirubin.

With help of the skin model, Monte Carlo simulations are carried out to acquire the hyperspectral reflectance. It simulates the cycle of a single photon and repeats cycles to derive light distribution profile including diffuse reflectance. 8 parameters

are randomly assigned values within the scope of Table 5.1 which is in line with
biological ranges. In total, 50000 samples are generated in SHSR database with
wavelength varying from 450nm to 700nm in about 18.58 hours.

Table 5.1: Lower bounds (LB) and upper bounds (UB) of 8 parameters

	C_m	$ratio_{ph\_eu}$	C_{w_epi}	C_{bl_der}
LB	1.3%	4.9%	10%	0.2%
UB	43%	36%	20%	7%
	S	C_{w_der}	d_{epi}	d_{der}
LB	70%	40%	0.027mm	0.6mm
UB	95%	90%	0.15mm	3mm
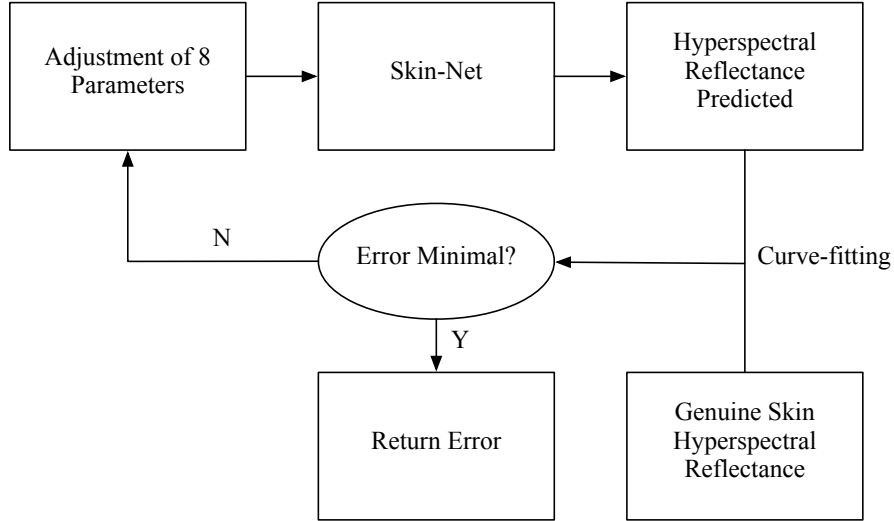
Figure 5.1: Flowchart of Skin-Net validation: fitting the hyperspectral reflectance
predicted to genuine skin

5.3   Experiments And Results

While the database has been built, we train a neural network between 8 parameters and the hyperspectral reflectance. This Skin-Net consists of two hidden layers with 45 neurons. To verify that it matches well with tissue optics, 30 hyperspectral reflectance samples of genuine skin from NSCU reflectance database[137] are validated. All 8 parameters must be assigned within the realistic range. Figure.5.1
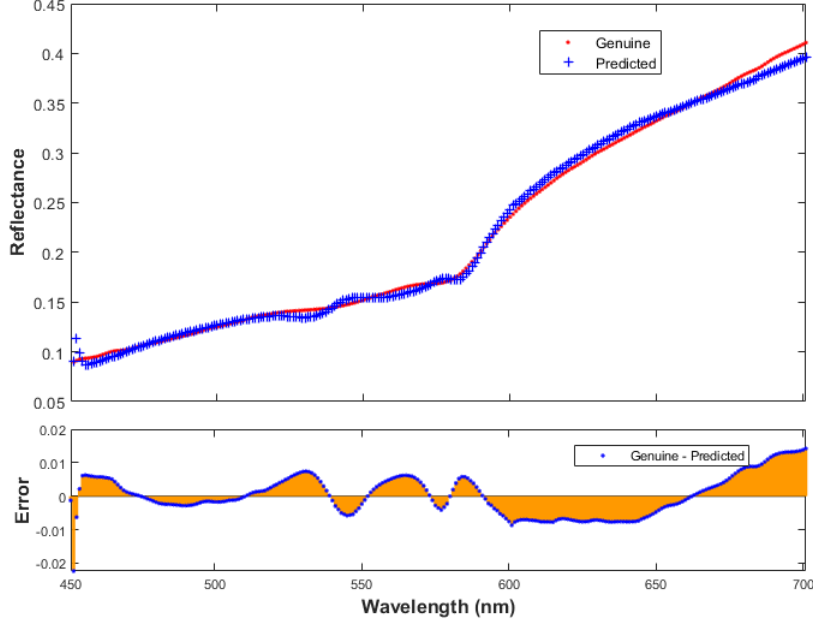
Figure 5.2: Validation of genuine skin no.2

shows the validation flowchart, and the error is computed as the mean square error (MSE):

$$MSE = \frac{\sum_{\lambda_{initial}}^{\lambda_{final}} (Pre_\lambda - Tar_\lambda)^2}{Nb_{wavelength}} \tag{5.1}$$

where Pre_λ and Tar_λ are hyperspectral reflectance predicted and targeted;$Nb_{wavelength}$ is the number of spectral bands. This curve-fitting process is executed using "fmincon" built-in interior-point algorithm in MATLAB 2018a.

The results show that Skin-Net can estimate very similar reflectance. The mean value of all 30 samples validations is $3.66e^{-05}$. In Figure.5.2, hyperspectral reflectance of genuine skin no.2 and the one predicted by Skin-Net are illustrated. These two reflectance curves are quite close among 450-700nm. Skin-Net characteristics are listed below:

- Reflectance predicted only concerns in the visible light range

- Network is trained in database generated by Monte Carlo simulations

- Skin model is assumed to be two-layered structure
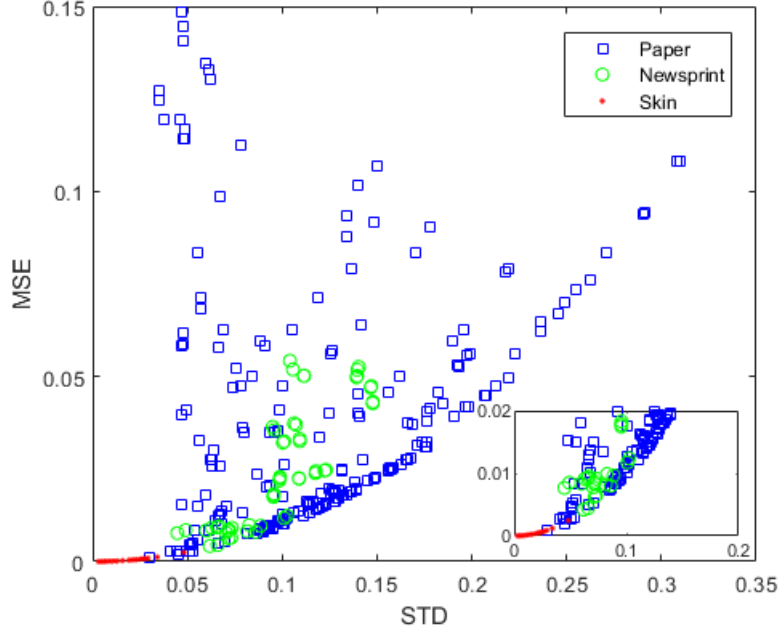
Figure 5.3: MSE and STD values of 300 samples are calculated after finishing curve-fitting process. Blue squares, green circles and red points denote paper, newsprint and skin respectively. The bottom right sub-figure is a zoom in for MSE varying from 0 to 0.02.

As we mentioned above, other materials cannot interact with light in the same way skin does. Therefore, we take Skin-Net and curve-fitting process to do liveness detection tasks. 270 hyperspectral reflectance of objects including coloured papers and newsprint which comes from the public database of the University of Eastern Finland[138] together with 30 samples of genuine skin from NSCU are classified together. All MSE and STD are computed as the basis when the curve-fitting process reaches an optimal solution. For the reason that Skin-Net has a great performance in fitting the genuine skin reflectance curve, when it refers to other materials, the results are significantly different. Here, we identify genuine skin by setting thresholds of MSE and STD. We define two categories: (a) at least one of them is less than the threshold; (b) MSE and STD are less than the thresholds at the same time. 0.001 and 0.05 are separately assigned to MSE and STD. Table 5.2 reveals the classification results. For category (a), skin objects are all classified in the

right group, while 24 objects (near 8.9%) are wrongly accepted. And we find that even in a more strict situation, there is a paper object accepted. Figure.5.3 shows the STD-MSE distribution of 300 samples. Compared to the existing research, the spectral band 930nm has shown the lowest error rate: 6% and 8.5% attack presentation classification error rate (APCER), 3% and 0% bona-fide presentation attack classification error rate (BPCER) with the classification method LBP-SVM and BSIF-SVM [139]. Our results still need to be improved. By analyzing the fitting hyperspectral reflectance of the paper object accepted, we decide to focus on the spectral bands 500-600nm. As shown in Figure.5.4, the main differences occur from 500nm to 600nm. The wavelength scope for calculating MSE is changed, and "fmincon" is applied once again to get new results.

Table 5.2: Classification results in two categories

MSE $\leq$ 0.001 or STD $\leq$ 0.05	**Acceptance**	**Rejection**
Non-skin	24	246
Skin	30	0
MSE $\leq$ 0.001 and STD $\leq$ 0.05	**Acceptance**	**Rejection**
Non-skin	1	269
Skin	28	2

The mean value of all 30 skin samples validations has decreased to $3.51e^{-06}$. In contrast, MSE of non-skin samples augments. Because one important pigment of skin, hemoglobin, has a unique curve of the absorption coefficients from 500nm to 600nm. It is similar to "W" in shape, which is called "W" pattern [21]. After applying this new wavelength range, both the APCER and the BCER reach 0%.

Limited to the spectra database, it needs more hyperspectral images data to validate. To our best knowledge, there isn't yet a public database about hyperspectral face images. We found a set of hyperspectral face images that only concern one person from CAVE [140] as shown in Figure.5.5. These images vary from 400nm to 700nm with a step 10nm captured by a cooled CCD camera (Apogee Alta U260) under the light source CIE Standard Illuminant D65. As a start, we apply our
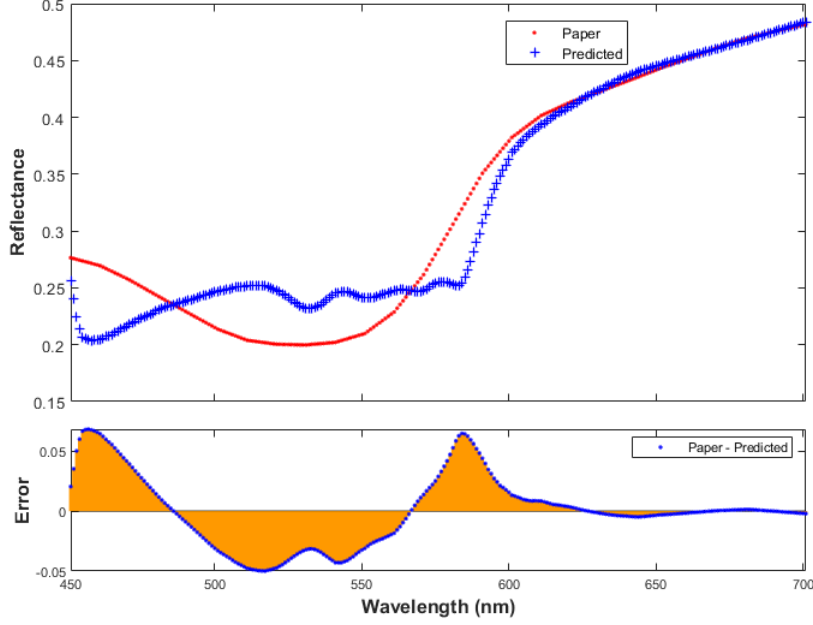
Figure 5.4: Fitting process on paper object no.59

Skin-Net to identify these images. All 31 images are in format PNG (16bit), and consists of 512*512 pixels. We denote a tensor $I_{i,j,k}$ which represent these 31 images, where i,j,k are the height (H), the width (W), and the spectra bands (S) respectively. Considering the hyperspectral reflectance, k is expanded from 31 to 301 by using the interpolation algorithm. Then, $I_{i,j,k}$ should locate on faces, in other words, i and j are restricted. Several points are randomly taken in the faces range including face photo and genuine face defined by $P_{h,w}$. The metric to validate these points is shown below:

$$MSE = \frac{\sum \sum_{h-1,w-1}^{h+1,w+1}(Ref(P_{h,w}) - Pre(P_{h,w}))^2}{9} \tag{5.2}$$

where Ref() is the hyperspectral reflectance of point $P_{h,w}$; Pre() represents the reflectance predicted by Skin-Net of point $P_{h,w}$.

That is to say, a 3*3*301 reflectance tensor is fitted by Skin-Net, and the mean square error is returned back to validate the performance. In our experiments, every 3 points are taken both in face photo and genuine face. Results are calculated in
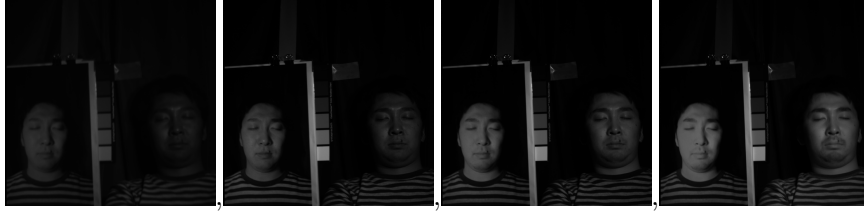
Figure 5.5: face photo and genuine face at 400nm, 500nm, 600nm, 700nm

Table 5.3: MSE results in two wavelength range

	P1	P2	P3
450-700nm	$1.80e^{-05}$	$1.40e^{-05}$	$1.37e^{-05}$
500-600nm	$2.70e^{-06}$	$1.38e^{-05}$	$3.30e^{-06}$
	P4	P5	P6
450-700nm	$1.91e^{-04}$	$1.66e^{-04}$	$1.58e^{-04}$
500-600nm	$6.31e^{-05}$	$5.43e^{-05}$	$5.17e^{-05}$

two wavelength range: 450-700nm and 500-600nm. From Table 5.3, we can find that the former three points have fewer errors than the latter three. Generally, the errors are in different orders of magnitude, like the latter three are about 10 times larger than the former three. The fact is that the former three points are taken from the genuine face, and the latter three belong to face photos. Regardless of from which sources these points are taken, the errors for range 450-700nm seem to have greater difference than range 500-600nm. This may be not only because of a larger wavelength range adopted, but also the degree of skin pigmented. This means that the degree of skin pigmented influences fitting results. For skin lightly-pigmented, the melanin volume fraction varies between 1.3% and 3%, and the effect of blood to skin appearance becomes more significant. Thus, it is better to choose the range 500-600nm where the absorption coefficient of hemoglobin changes rapidly. As for skin darkly-pigmented, due to the large melanin volume fraction and its smooth change over the spectra, it's necessary to adopt a larger wavelength range.

5.4 Conclusions

Our research proposes an auxiliary method for PAD by analyzing the hyperspectral reflectance. We firstly trained a network Skin-Net with a spectra database generated by Monte Carlo simulations. Unlike the Lambertian model, Monte Carlo simulations are closer to reality. Then, Skin-Net is applied to detect if the spectra belong to the skin or not with the help of curve-fitting. Two spectra ranges are studied for better performance and robustness. Based on tissue optics and biological facts of skin, it's much efficient to detect artefacts. Due to lack of hyperspectral face image database, we only check this method on hyperspectral photos of one person. The results between face photos and genuine face are quite different. That would be used as an indicator to detect presentation attacks. We also discuss the wavelength range selection. Our proposed method has the potential to develop, and more hyperspectral face images will be collected with a snap-scan VNIR range system integrating a linescan HSI sensor (IMEC CMV2K LS150+VNIR) and an image sensor (CMOSIS CMV2000). With more images data to validate, we'll apply our method to face recognition system for supporting PAD.

Conclusion and Perspectives

Contents

6.1   Conclusion

In this thesis, we concentrate on human skin characterization and analysis based on diffuse reflectance. We have built a detailed skin model composed of three sublayers: the epidermis, the dermis and the subcutis, including physiological parameters. Based on the skin model, we have made a quantitative analysis of skin and its reflectance. Firstly, we implement Monte Carlo simulations in Python and speed it up by using an array variable to store the values of trigonometric function and reduce the trigonometric operations. Then, a GPU-based techniques is applied for further acceleration. It takes around 37 s to obtain a reflectance spectrum in the visible light range using GPU-base Monte Carlo simulations. A large database is generated with help of Monte Carlo simulations and then used for training the forward neural network, which maps physiological parameters to reflectance spectra. Then we can fast produce a reflectance spectrum from physiological parameters in around 19.4 ms using this forward neural network. The effects on reflectance spectra of all parameters are evaluated. And we find that generally the volume fraction of melanin is inversely proportional to the reflectance. The volume fraction of blood and oxygen saturation are highly related to the "W" pattern in the reflectance curve. These effects match the absorption coefficient of skin pigments, which proves that

this forward neural network can explain well the light-skin interaction like Monte Carlo simulations. Moreover, the forward neural network is then applied to extract skin parameters with help of the curve-fitting process. We first validate the extraction performance with the synthetic data and then the measured data from NIST. All validations are carried out in three groups: lightly pigmented skin type, moderately pigmented skin type and darkly pigmented skin type. For melanin, blood and oxygen saturation, the average relative absolute prediction errors are 1.36%, 8.55% and 3.03% respectively compared to Monte Carlo simulations. Note that we conduct experiments in two skin models: two-layered and three-layered. Finally, validations with the measured data also give acceptable results with the curve-fitting performances (defined by RMSE) are less than around 10%. And by comparing the curve-fitting performances for both two-layered and three-layered skin models, we choose the extraction results with less RMSE. The experiments turn out that the forward neural network combined with proposed skin models is not only accurate but also robust. However, for those pigments, such as bilirubin, which have less effects on skin reflectance. It is hard to give a precise estimation using only the visible light range. The potential solution is the selection of the wavelength range. Finding the range where the absorption coefficient of bilirubin is much different from other pigments or has its own pattern will be studied in future work.

Besides the forward model, the inverse model is also adopted to extract melanin content. The difference between them is the direction of mapping. The inputs of the forward model are skin parameters, and the outputs are skin reflectance, however, the inverse model reverse them. Based on previous research, we find that the inverse neural network suffers from high estimation errors and small databases. We have generated 50000 skin reflectance spectra for training. And two dimensionality reduction techniques: low variance filter (LVF) and principal components analysis (PCA) are used for speeding up the training time from nearly one hour to only ten minutes. And PCA works better than LVF. Lastly, the inverse neural network are compared to random forest and support vector regressions in estimating melanin content. We find that the inverse neural network has extremely high speed around 12 ms for one extraction process, which is a great improvement, while the accuracy

maintains almost the same. However, the inverse neural network is not intuitive and not robust. A noise signal in the measured data may cause inaccurate estimations. Methods to find the outliers need to be applied in future work.

On the other hand, our proposed skin models can be also used for skin and non-skin classification to detect presentation attacks in the visible light range. This application is based on the assumption that the direction of incident light doesn't affect the steady-state diffuse reflectance profile of skin, which can be seen in previous research[141, 142]. Two metrics RMSE and STD of fitting performance are used to identify if it is skin or non-skin. We mainly deal with the diffuse reflectance spectra from NSCU but not images due to lack of hyperspectral skin image databases. By selecting the appropriate wavelength range, both attack presentation classification error rate (APCER) and bonna-fide presentation attack classification error rate (BPCER) reach 0% in our testing database. It still needs more databases, preferably image databases for verification.

6.2   Perspectives

As perspectives, we plan to improve our skin model by adding separate upper and deep blood plexus. In tissue, blood is not evenly distributed, but rather confined to vessels. This fact affects the reflectance spectra considerably, and is often referred to as the vessel packaging effect[143]. Without accounting for the vessel packaging effect, the estimations of the oxygen saturation and the blood concentration may be incorrect, so the inclusion of it in the presented method should be considered. Moreover, the metric to evaluate the fitting process can be updated to some other forms, like Jeffrey divergence, etc. As for skin and non-skin classification, our proposed method needs to execute the reflectance curve-fitting process for every pixel in the hyperspectral image, and it costs so much time that it is not available for real time applications. We also design another framework that is a classification network trained by a large amount of reflectance spectra with skin and non-skin labels. Those skin labeled data is generated by Monte Carlo simulations and non-skin labeled data is from the public database of the University of Eastern Finland[138]. And the de-

tection results is shown in Figure.6.1. We plan to collect more hyperspectral face images for better validation.

(a) Face image from CAVE

(b) After detection
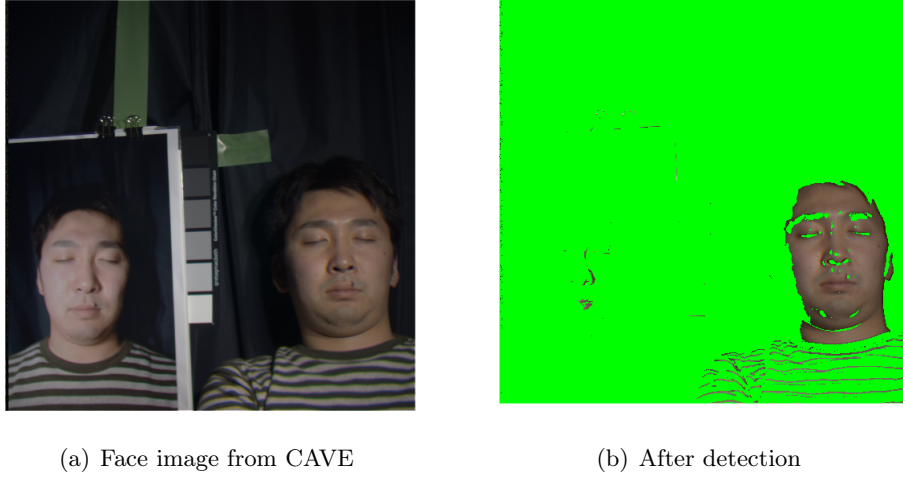
Figure 6.1: Detection results for a face image from CAVE.

Bibliography

[1] T. B. Fitzpatrick, "Soleil et peau," *J Med Esthet*, vol. 2, pp. 33–34, 1975. 1

[2] ——, "Ultraviolet-induced pigmentary changes: benefits and hazards," in *Therapeutic photomedicine.* Karger Publishers, 1986, vol. 15, pp. 25–38. 1

[3] W. A. Haviland, H. E. Prins, D. Walrath, and B. McBride, *The essence of anthropology.* Cengage Learning, 2012. 2

[4] H. Nilsson and G. E. Nilsson, "Monte carlo simulations of light interaction with blood vessels in human skin in the red-wavelength region," in *Optical Diagnostics of Biological Fluids III*, vol. 3252. International Society for Optics and Photonics, 1998, pp. 44–53. 3

[5] L. L. Randeberg, A. Winnem, R. Haaverstad, and L. O. Svaasand, "Performance of diffusion theory vs. monte carlo methods," in *European Conference on Biomedical Optics.* Optical Society of America, 2005, p. ThB3. 3

[6] M. Jasiński, "Modelling of light and human skin interaction using kubelka-munk theory," *Scientific Research of the Institute of Mathematics and Computer Science*, vol. 10, no. 1, pp. 71–81, 2011. 3

[7] L. Zhang, Z. Wang, and M. Zhou, "Determination of the optical coefficients of biological tissue by neural network," *Journal of Modern Optics*, vol. 57, no. 13, pp. 1163–1170, 2010. 3, 85

[8] K. S. Saladin, "Anatomy & physiology: the unity of form and function," 2004. 7

[9] B. Amirlak, L. Shahabi, S. Javaheri, F. Talavera, W. Stadelmann *et al.*, "Skin anatomy," *Medscape Ref*, vol. 1, 2013. 7

[10] J. Kanitakis, "Anatomy, histology and immunohistochemistry of normal human skin," *European journal of dermatology*, vol. 12, no. 4, pp. 390–401, 2002. 7

[11] T. Lister, P. A. Wright, and P. H. Chappell, "Optical properties of human skin," *Journal of biomedical optics*, vol. 17, no. 9, p. 090901, 2012. 8

[12] Y. Masuda, Y. Ogura, Y. Inagaki, T. Yasui, and Y. Aizu, "Analysis of the influence of collagen fibres in the dermis on skin optical reflectance by monte carlo simulation in a nine-layered skin model," *Skin Research and Technology*, vol. 24, no. 2, pp. 248–255, 2018. 8

[13] J. McGrath, R. Eady, and F. Pope, "Anatomy and organization of human skin," *Rookâs textbook of dermatology*, vol. 1, pp. 3–2, 2004. 8

[14] G. V. Baranoski and A. Krishnaswamy, *Light and skin interactions: simulations for computer graphics applications.* Morgan Kaufmann, 2010. 10, 11, 14, 91

[15] T. Vos, C. Allen, M. Arora, R. M. Barber, Z. A. Bhutta, A. Brown, A. Carter, D. C. Casey, F. J. Charlson, A. Z. Chen *et al.*, "Global, regional, and national incidence, prevalence, and years lived with disability for 310 diseases and injuries, 1990–2015: a systematic analysis for the global burden of disease study 2015," *The lancet*, vol. 388, no. 10053, pp. 1545–1602, 2016. 10, 84

[16] H. Wang, M. Naghavi, C. Allen, R. M. Barber, Z. A. Bhutta, A. Carter, D. C. Casey, F. J. Charlson, A. Z. Chen, M. M. Coates *et al.*, "Global, regional, and national life expectancy, all-cause mortality, and cause-specific mortality for 249 causes of death, 1980–2015: a systematic analysis for the global burden of disease study 2015," *The lancet*, vol. 388, no. 10053, pp. 1459–1544, 2016. 10

[17] S. Nafisi and H. I. Maibach, "Skin penetration of nanoparticles," in *Emerging nanotechnologies in immunology.* Elsevier, 2018, pp. 47–88. 11

[18] W. Pawlina and M. H. Ross, *Histology: a text and atlas: with correlated cell and molecular biology.* Lippincott Williams & Wilkins, 2018. 11

Bibliography

---

[19] R. Oliver, H. Barker, A. Cooke, and R. Grant, "Dermal collagen implants," *Biomaterials*, vol. 3, no. 1, pp. 38–40, 1982. 12

[20] L. Hutchins, "Identification and classification," 2013. 12

[21] W. Chen, M. Ardabilian, A. Zine, and H. Zahouani, "Reflectance spectra based skin and non-skin classification," in *2015 IEEE International Conference on Image Processing (ICIP)*. IEEE, 2015, pp. 755–759. 12, 91, 103

[22] P. Harris, S. Nagy, and N. Vardaxis, *Mosby's Dictionary of Medicine, Nursing and Health Professions-Australian & New Zealand Edition-eBook*. Elsevier Health Sciences, 2014. 12

[23] S. M. Jain, K. Pandey, A. Lahoti, and P. K. Rao, "Evaluation of skin and subcutaneous tissue thickness at insulin injection sites in indian, insulin naïve, type-2 diabetic adult population," *Indian journal of endocrinology and metabolism*, vol. 17, no. 5, p. 864, 2013. 13

[24] K. L. Diegel, D. M. Danilenko, and Z. W. Wojcinski, "The integumentary system," in *Fundamentals of Toxicologic Pathology*. Elsevier, 2018, pp. 791–822. 13

[25] K. Saladin, "Human anatomy. rex bookstore," 2005. 13

[26] H. L. Brannon, "Subcutaneous tissue: The innermost layer of skin," [EB/OL], https://www.verywellhealth.com/subcutaneous-tissue-1068882 Accessed July 15, 2020. 13

[27] W. R. McCluney, *Introduction to radiometry and photometry*. Artech House, 2014. 14

[28] G. Laufer, *Introduction to optics and lasers in engineering*. Cambridge University Press, 1996. 14

[29] H. Bradt, *Astronomy methods: A physical approach to astronomical observations*. Cambridge University Press, 2004. 14

[30] L. Ohannesian and A. Streeter, *Handbook of pharmaceutical analysis*. CRC Press, 2001. 14

[31] V. Ahluwalia and M. Goyal, *A Textbook of Organic Chemistry*. Alpha Science Int'l Ltd., 2000. 14

[32] G. N. Lewis, "The conservation of photons," *Nature*, vol. 118, no. 2981, pp. 874–875, 1926. 14

[33] E. Hecht and A. Zajac, "Optics, chapter 9," *Addison-Wesley*, vol. 3, pp. 384–441, 2002. 14

[34] P. Bouguer, *Essai d'optique sur la gradation de la lumière*. chez Claude Jombert, ruë S. Jacques, au coin de la ruë des Mathurins, à l â¦, 1729. 15

[35] J. H. Lambert, *Photometria sive de mensura et gradibus luminis, colorum et umbrae*. Klett, 1760. 15

[36] A. Beer, "Bestimmung der absorption des rothen lichts in farbigen flussigkeiten," *Ann. Physik*, vol. 162, pp. 78–88, 1852. 16

[37] L. Rayleigh, "X. on the electromagnetic theory of light," *The London, Edinburgh, and Dublin Philosophical Magazine and Journal of Science*, vol. 12, no. 73, pp. 81–101, 1881. 16

[38] ——, "Xxxiv. on the transmission of light through an atmosphere containing small particles in suspension, and on the origin of the blue of the sky," *The London, Edinburgh, and Dublin Philosophical Magazine and Journal of Science*, vol. 47, no. 287, pp. 375–384, 1899. 16

[39] J. H. Seinfeld and S. N. Pandis, *Atmospheric chemistry and physics: from air pollution to climate change*. John Wiley & Sons, 2016. 16

[40] C. F. Bohren and D. R. Huffman, *Absorption and scattering of light by small particles*. John Wiley & Sons, 2008. 17

[41] M. H. Nayfeh, *Fundamentals and Applications of Nano Silicon in Plasmonics and Fullerines: Current and Future Trends*. Elsevier, 2018. 17

Bibliography

[42] J. R. Gordon and J. C. Brieva, "Unilateral dermatoheliosis," *New England Journal of Medicine*, vol. 366, no. 16, p. e25, 2012. 18

[43] W. Tobiska and A. Nusinov, "Iso 21348-process for determining solar irradiances," *cosp*, vol. 36, p. 2621, 2006. 18

[44] H. Törmä, B. Berne, and A. Vahlquist, "Uv irradiation and topical vitamin a modulate retinol esterification in hairless mouse epidermis." *Acta dermato-venereologica*, vol. 68, no. 4, pp. 291–299, 1988. 18

[45] R. Duan, J. Zhang, X. Du, X. Yao, and K. Konno, "Properties of collagen from skin, scale and bone of carp (cyprinus carpio)," *Food chemistry*, vol. 112, no. 3, pp. 702–706, 2009. 20

[46] J. Schmitt and G. Kumar, "Turbulent nature of refractive-index variations in biological tissue," *Optics letters*, vol. 21, no. 16, pp. 1310–1312, 1996. 21

[47] M. Xu and R. R. Alfano, "Fractal mechanisms of light scattering in biological tissue and cells," *Optics letters*, vol. 30, no. 22, pp. 3051–3053, 2005. 21

[48] J. D. Rogers, İ. R. Çapoğlu, and V. Backman, "Nonscalar elastic light scattering from continuous random media in the born approximation," *Optics letters*, vol. 34, no. 12, pp. 1891–1893, 2009. 21

[49] J. Yi and V. Backman, "Imaging a full set of optical scattering properties of biological tissue by inverse spectroscopic optical coherence tomography," *Optics letters*, vol. 37, no. 21, pp. 4443–4445, 2012. 21

[50] S. Chandrasekhar, *Radiative transfer*. Courier Corporation, 2013. 23

[51] J. Lenoble, "Radiative transfer in scattering and absorbing atmospheres," 1990. 23

[52] L. Tsang, J. A. Kong, and R. T. Shin, "Theory of microwave remote sensing," 1985. 24

[53] F. T. Ulaby, R. K. Moore, and A. K. Fung, "Microwave remote sensing: Active and passive. volume 3-from theory to applications," 1986. 24

[54] P. Kubelka, "Ein beitrag zur optik der farbanstriche (contribution to the optic of paint)," *Zeitschrift fur technische Physik*, vol. 12, pp. 593–601, 1931. 25

[55] R. McDonald *et al.*, *Colour physics for industry*, 1997. 25

[56] G. Wyszecki and W. S. Stiles, *Color science.* Wiley New York, 1982, vol. 8. 26

[57] A. R. Choudhury, "Instrumental colourant formulation in principles of colour and appearance measurement," *Visual Measurement of Colour, Colour Comparison and Management*, vol. 2, pp. 117–146, 2015. 27

[58] J. H. Nobbs, "Kubelkaâmunk theory and the prediction of reflectance," *Review of Progress in Coloration and Related Topics*, vol. 15, no. 1, pp. 66–75, 1985. 27

[59] C. T. Sandoval, "Generalized kubelka-munk theory-a derivation and extension from radiative transfer," Ph.D. dissertation, UC Merced, 2016. 27

[60] G. Kortüm, *Reflectance spectroscopy: principles, methods, applications.* Springer Science & Business Media, 2012. 31

[61] W. Egan, *Optical properties of inhomogeneous materials: applications to geology, astronomy chemistry, and engineering.* Elsevier, 2012. 32

[62] F. E. Nicodemus, "Directional reflectance and emissivity of an opaque surface," *Applied optics*, vol. 4, no. 7, pp. 767–775, 1965. 32

[63] G. Eason, A. Veitch, R. Nisbet, and F. Turnbull, "The theory of the backscattering of light by blood," *Journal of Physics D: Applied Physics*, vol. 11, no. 10, p. 1463, 1978. 33

[64] T. J. Farrell, M. S. Patterson, and B. Wilson, "A diffusion theory model of spatially resolved, steady-state diffuse reflectance for the noninvasive determination of tissue optical properties in vivo," *Medical physics*, vol. 19, no. 4, pp. 879–888, 1992. 33

Bibliography

[65] H. W. Jensen, S. R. Marschner, M. Levoy, and P. Hanrahan, "A practical model for subsurface light transport," in *Proceedings of the 28th annual conference on Computer graphics and interactive techniques*, 2001, pp. 511–518. 34

[66] C. Donner and H. W. Jensen, "Light diffusion in multi-layered translucent materials," *ACM Transactions on Graphics (ToG)*, vol. 24, no. 3, pp. 1032–1039, 2005. 34

[67] N. Metropolis, "The beginning," *Los Alamos Science*, vol. 15, pp. 125–130, 1987. 37

[68] D. P. Kroese, T. Brereton, T. Taimre, and Z. I. Botev, "Why the monte carlo method is so important today," *Wiley Interdisciplinary Reviews: Computational Statistics*, vol. 6, no. 6, pp. 386–392, 2014. 37

[69] L. Wang, S. L. Jacques, and L. Zheng, "Mcmlâmonte carlo modeling of light transport in multi-layered tissues," *Computer methods and programs in biomedicine*, vol. 47, no. 2, pp. 131–146, 1995. 37, 57, 58, 59, 84

[70] M. Born and E. Wolf, *Principles of optics: electromagnetic theory of propagation, interference and diffraction of light*. Elsevier, 2013. 38

[71] L. G. Henyey and J. L. Greenstein, "Diffuse radiation in the galaxy," *The Astrophysical Journal*, vol. 93, pp. 70–83, 1941. 41

[72] M. F. Modest, *Radiative heat transfer*. Academic press, 2013. 41

[73] M. Van Gemert, S. L. Jacques, H. Sterenborg, and W. Star, "Skin optics," *IEEE Transactions on biomedical engineering*, vol. 36, no. 12, pp. 1146–1154, 1989. 41

[74] Q. Fang and D. A. Boas, "Monte carlo simulation of photon migration in 3d turbid media accelerated by graphics processing units," *Optics express*, vol. 17, no. 22, pp. 20 178–20 190, 2009. 43

[75] J. Pichette, W. Charle, and A. Lambrechts, "Fast and compact internal scanning cmos-based hyperspectral camera: the snapscan," in *Photonic Instru-*

mentation Engineering IV, vol. 10110. International Society for Optics and Photonics, 2017, p. 1011014. 45

[76] J. M. Palmer and B. G. Grant, "The art of radiometry." SPIE, 2009. 46

[77] J. J. Tomes and C. E. Finlayson, "Low cost 3d-printing used in an undergraduate project: an integrating sphere for measurement of photoluminescence quantum yield," *European Journal of Physics*, vol. 37, no. 5, p. 055501, 2016. 46

[78] A. Mazzoli, R. Munaretto, and L. Scalise, "Preliminary results on the use of a noninvasive instrument for the evaluation of the depth of pigmented skin lesions: numerical simulations and experimental measurements," *Lasers in medical science*, vol. 25, no. 3, pp. 403–410, 2010. 50

[79] M. Mehrübeoğlu, N. Kehtarnavaz, G. Marquez, M. Duvic, and L. V. Wang, "Skin lesion classification using oblique-incidence diffuse reflectance spectroscopic imaging," *applied optics*, vol. 41, no. 1, pp. 182–192, 2002. 50

[80] E. V. Salomatina, B. Jiang, J. Novak, and A. N. Yaroslavsky, "Optical properties of normal and cancerous human skin in the visible and near-infrared spectral range," *Journal of biomedical optics*, vol. 11, no. 6, p. 064026, 2006. 50

[81] V. Wallace, D. Crawford, P. Mortimer, R. Ott, and J. Bamber, "Spectrophotometric assessment of pigmented skin lesions: methods and feature selection for evaluation of diagnostic performance," *Physics in Medicine & Biology*, vol. 45, no. 3, p. 735, 2000. 50

[82] S. L. Jacques, "Origins of tissue optical properties in the uva, visible, and nir regions," *OSA TOPS on advances in optical imaging and photon migration*, vol. 2, pp. 364–369, 1996. 50, 53, 56

[83] I. Fredriksson, M. Larsson, and T. Strömberg, "Inverse monte carlo method in a multilayered tissue model for diffuse reflectance spectroscopy," *Journal of biomedical optics*, vol. 17, no. 4, p. 047004, 2012. 50, 85

[84] M. Sharma, R. Hennessy, M. K. Markey, and J. W. Tunnell, "Verification of a two-layer inverse monte carlo absorption model using multiple source-detector separation diffuse reflectance spectroscopy," *Biomedical optics express*, vol. 5, no. 1, pp. 40–53, 2014. 50

[85] E. Alerstam, T. Svensson, and S. Andersson-Engels, "Parallel computing with graphics processing units for high-speed monte carlo simulation of photon migration," *Journal of biomedical optics*, vol. 13, no. 6, p. 060504, 2008. 50

[86] K. Furutsu, "Diffusion equation derived from space-time transport equation," *JOSA*, vol. 70, no. 4, pp. 360–366, 1980. 50

[87] E. Zherebtsov, V. Dremin, A. Popov, A. Doronin, D. Kurakina, M. Kirillin, I. Meglinski, and A. Bykov, "Hyperspectral imaging of human skin aided by artificial neural networks," *Biomedical optics express*, vol. 10, no. 7, pp. 3545–3559, 2019. 50

[88] P. Naglič, L. Vidovič, M. Milanič, L. L. Randeberg, and B. Majaron, "Suitability of diffusion approximation for an inverse analysis of diffuse reflectance spectra from human skin in vivo," *OSA Continuum*, vol. 2, no. 3, pp. 905–922, 2019. 51, 80, 85

[89] I. V. Meglinski and S. J. Matcher, "Quantitative assessment of skin layers absorption and skin reflectance spectra simulation in the visible and near-infrared spectral regions," *Physiological measurement*, vol. 23, no. 4, p. 741, 2002. 51

[90] S. Vyas, A. Banerjee, and P. Burlina, "Estimating physiological skin parameters from hyperspectral signatures," *Journal of biomedical optics*, vol. 18, no. 5, p. 057008, 2013. 51

[91] L. Pilon, A. Bhowmik, R.-L. Heng, and D. Yudovsky, "Simple and accurate expressions for diffuse reflectance of semi-infinite and two-layer absorbing and scattering media: erratum," *Applied optics*, vol. 54, no. 19, pp. 6116–6117, 2015. 51

[92] R. Reif, O. A'Amar, and I. J. Bigio, "Analytical model of light reflectance for extraction of the optical properties in small volumes of turbid media," *Applied optics*, vol. 46, no. 29, pp. 7317–7328, 2007. 51

[93] D. Yudovsky and L. Pilon, "Rapid and accurate estimation of blood saturation, melanin content, and epidermis thickness from spectral diffuse reflectance," *Applied optics*, vol. 49, no. 10, pp. 1707–1719, 2010. 51

[94] S. A. Lisenko, M. M. Kugeiko, V. A. Firago, and A. N. Sobchuk, "Analytical model of diffuse reflectance spectrum of skin tissue," *Quantum Electronics*, vol. 44, no. 1, p. 69, 2014. 51

[95] G. Zonios, A. Dimou, I. Bassukas, D. Galaris, A. Tsolakidis, and E. Kaxiras, "Melanin absorption spectroscopy: new method for noninvasive skin investigation and melanoma detection," *Journal of biomedical optics*, vol. 13, no. 1, p. 014017, 2008. 51

[96] D. Yudovsky, J. Q. M. Nguyen, and A. J. Durkin, "In vivo spatial frequency domain spectroscopy of two layer media," *Journal of biomedical optics*, vol. 17, no. 10, p. 107006, 2012. 51

[97] D. Yudovsky and A. J. Durkin, "Spatial frequency domain spectroscopy of two layer media," *Journal of biomedical optics*, vol. 16, no. 10, p. 107005, 2011. 51

[98] S.-Y. Tsui, C.-Y. Wang, T.-H. Huang, and K.-B. Sung, "Modelling spatially-resolved diffuse reflectance spectra of a multi-layered skin model by artificial neural networks trained with monte carlo simulations," *Biomedical optics express*, vol. 9, no. 4, pp. 1531–1544, 2018. 51, 60, 86

[99] C.-Y. Wang, T.-C. Kao, Y.-F. Chen, W.-W. Su, H.-J. Shen, and K.-B. Sung, "Validation of an inverse fitting method of diffuse reflectance spectroscopy to quantify multi-layered skin optical properties," in *Photonics*, vol. 6, no. 2. Multidisciplinary Digital Publishing Institute, 2019, p. 61. 51, 85

Bibliography

[100] T. Maeda, N. Arakawa, M. Takahashi, and Y. Aizu, "Monte carlo simulation of spectral reflectance using a multilayered skin tissue model," *Optical review*, vol. 17, no. 3, pp. 223–229, 2010. 52

[101] R. R. Anderson, J. A. Parrish *et al.*, "The optics of human skin." *Journal of investigative dermatology*, vol. 77, no. 1, pp. 13–19, 1981. 52, 53

[102] M. Doi and S. Tominaga, "Spectral estimation of human skin color using the kubelka-munk theory," in *Color Imaging VIII: Processing, Hardcopy, and Applications*, vol. 5008. International Society for Optics and Photonics, 2003, pp. 221–228. 52, 53, 56

[103] I. Meglinsky and S. Matcher, "Modelling the sampling volume for skin blood oxygenation measurements," *Medical and Biological Engineering and Computing*, vol. 39, no. 1, pp. 44–50, 2001. 52, 53, 56

[104] S. Prahl, "Optical absorption of hemoglobin," [EB/OL], https://omlc.org/spectra/hemoglobin/ Accessed July 15, 2020. 53

[105] S. Jacques and S. Prahl, "Assorted spectra," [EB/OL], https://omlc.org/spectra/index.html Accessed July 15, 2020. 54

[106] S. L. Jacques, "Optical properties of biological tissues: a review," *Physics in Medicine & Biology*, vol. 58, no. 11, pp. R37–61, 2013. 55

[107] D. Parsad, K. Wakamatsu, A. Kanwar, B. Kumar, and S. Ito, "Eumelanin and phaeomelanin contents of depigmented and repigmented skin in vitiligo patients," *British Journal of Dermatology*, vol. 149, no. 3, pp. 624–626, 2003. 56, 91

[108] R. Flewelling, "Noninvasive optical monitoring, in âthe biomedical engineering handbook,â jd bronzino, ed," 2000. 56

[109] E. Angelopoulou, "Understanding the color of human skin," in *Human vision and electronic imaging VI*, vol. 4299. International Society for Optics and Photonics, 2001, pp. 243–251. 56

121

[110] H. C. Van de Hulst, *Multiple light scattering: tables, formulas, and applications.* Elsevier, 2012. 57, 58

[111] S. A. Prahl, "A monte carlo model of light propagation in tissue," in *Dosimetry of laser radiation in medicine and biology*, vol. 10305. International Society for Optics and Photonics, 1989, p. 1030509. 57, 58

[112] C. M. Gardner and A. J. Welch, "Improvements in the accuracy and statistical variance of the monte carlo simulation of light distribution in tissue," in *Laser-Tissue Interaction III*, vol. 1646. International Society for Optics and Photonics, 1992, pp. 400–409. 59

[113] C. C. Cooksey, D. W. Allen, and B. K. Tsai, "Reference data set of human skin reflectance," *J. Res. Nat. Inst. Standards Technol.*, vol. 122, pp. 1–5, 2017. 59, 77, 94

[114] C. Ash, M. Dubec, K. Donne, and T. Bashford, "Effect of wavelength and beam width on penetration in light-tissue interaction using computational methods," *Lasers in medical science*, vol. 32, no. 8, pp. 1909–1918, 2017. 80

[115] R. Habel, M. Kudenov, and M. Wimmer, "Practical spectral photography," in *Computer graphics forum*, vol. 31, no. 2pt2. Wiley Online Library, 2012, pp. 449–458. 84

[116] H. R. Kang, "Computational color technology (spie press monograph vol. pm159)." SPIE-International Society for Optical Engineering, 2006. 84

[117] R. Splinter and B. A. Hooper, *An introduction to biomedical optics.* Taylor & Francis, 2006. 84

[118] S. Vyas, H. Van Nguyen, P. Burlina, A. Banerjee, L. Garza, and R. Chellappa, "Computational modeling of skin reflectance spectra for biological parameter estimation through machine learning," in *Algorithms and Technologies for Multispectral, Hyperspectral, and Ultraspectral Imagery XVIII*, vol. 8390. International Society for Optics and Photonics, 2012, p. 83901B. 85

[119] S. Yan, R. Yao, X. Intes, and Q. Fang, "Accelerating monte carlo modeling of structured-light-based diffuse optical imaging via âphoton sharingâ," *Optics Letters*, vol. 45, no. 10, pp. 2842–2845, 2020. 85

[120] S. L. Jacques, R. D. Glickman, and J. A. Schwartz, "Internal absorption coefficient and threshold for pulsed laser disruption of melanosomes isolated from retinal pigment epithelium," in *Laser-Tissue Interaction VII*, vol. 2681. International Society for Optics and Photonics, 1996, pp. 468–477. 86

[121] E. Angelopoulou, "The reflectance spectrum of human skin," *Technical Reports (CIS)*, p. 584, 1999. 91

[122] S. G. Bhele and V. Mankar, "A review paper on face recognition techniques," *International Journal of Advanced Research in Computer Engineering & Technology (IJARCET)*, vol. 1, no. 8, pp. 339–346, 2012. 98

[123] F. Schroff, D. Kalenichenko, and J. Philbin, "Facenet: A unified embedding for face recognition and clustering," in *Proceedings of the IEEE conference on computer vision and pattern recognition*, 2015, pp. 815–823. 98

[124] O. M. Parkhi, A. Vedaldi, A. Zisserman *et al.*, "Deep face recognition." in *bmvc*, vol. 1, no. 3, 2015, p. 6. 98

[125] X. Wu, R. He, Z. Sun, and T. Tan, "A light cnn for deep face representation with noisy labels," *IEEE Transactions on Information Forensics and Security*, vol. 13, no. 11, pp. 2884–2896, 2018. 98

[126] R. Ramachandra and C. Busch, "Presentation attack detection methods for face recognition systems: A comprehensive survey," *ACM Computing Surveys (CSUR)*, vol. 50, no. 1, p. 8, 2017. 98

[127] O. Kähm and N. Damer, "2d face liveness detection: An overview," in *2012 BIOSIG-Proceedings of the International Conference of Biometrics Special Interest Group (BIOSIG)*. IEEE, 2012, pp. 1–12. 98

[128] A. Anjos, M. M. Chakka, and S. Marcel, "Motion-based counter-measures to photo attacks in face recognition," *IET biometrics*, vol. 3, no. 3, pp. 147–158, 2013. 98

[129] P. Wild, P. Radu, L. Chen, and J. Ferryman, "Robust multimodal face and fingerprint fusion in the presence of spoofing attacks," *Pattern Recognition*, vol. 50, pp. 17–25, 2016. 98

[130] A. Pinto, W. R. Schwartz, H. Pedrini, and A. de Rezende Rocha, "Using visual rhythms for detecting video-based facial spoof attacks," *IEEE Transactions on Information Forensics and Security*, vol. 10, no. 5, pp. 1025–1038, 2015. 98

[131] D. Wen, H. Han, and A. K. Jain, "Face spoof detection with image distortion analysis," *IEEE Transactions on Information Forensics and Security*, vol. 10, no. 4, pp. 746–761, 2015. 99

[132] P. Korshunov and S. Marcel, "Deepfakes: a new threat to face recognition? assessment and detection," *arXiv preprint arXiv:1812.08685*, 2018. 99

[133] S. Bhattacharjee, A. Mohammadi, and S. Marcel, "Spoofing deep face recognition with custom silicone masks," in *2018 IEEE 9th International Conference on Biometrics Theory, Applications and Systems (BTAS)*. IEEE, 2018, pp. 1–7. 99

[134] R. Ramachandra, S. Venkatesh, K. B. Raja, S. Bhattacharjee, P. Wasnik, S. Marcel, and C. Busch, "Custom silicone face masks: Vulnerability of commercial face recognition systems & presentation attack detection," in *2019 7th International Workshop on Biometrics and Forensics (IWBF)*. IEEE, 2019, pp. 1–6. 99

[135] Z. Zhang, D. Yi, Z. Lei, S. Z. Li *et al.*, "Face liveness detection by learning multispectral reflectance distributions." in *FG*, 2011, pp. 436–441. 99

[136] N. Kose and J.-L. Dugelay, "Reflectance analysis based countermeasure technique to detect face mask attacks," in *2013 18th International Conference on Digital Signal Processing (DSP)*. IEEE, 2013, pp. 1–6. 99

Bibliography

[137] M. J. Vrhel, R. Gershon, and L. S. Iwan, "Measurement and analysis of object reflectance spectra," *Color Research & Application*, vol. 19, no. 1, pp. 4–9, 1994. 100

[138] "Spectral database," https://www3.uef.fi/en/web/spectral/, accessed June 20, 2019. 102, 109

[139] R. Raghavendra, K. B. Raja, S. Venkatesh, F. A. Cheikh, and C. Busch, "On the vulnerability of extended multispectral face recognition systems towards presentation attacks," in *2017 IEEE International Conference on Identity, Security and Behavior Analysis (ISBA)*. IEEE, 2017, pp. 1–8. 103

[140] F. Yasuma, T. Mitsunaga, D. Iso, and S. K. Nayar, "Generalized assorted pixel camera: postcapture control of resolution, dynamic range, and spectrum," *IEEE transactions on image processing*, vol. 19, no. 9, pp. 2241–2253, 2010. 103

[141] H. Li, C. Zhang, and X. Feng, "Monte carlo simulation of light scattering in tissue for the design of skin-like optical devices," *Biomedical optics express*, vol. 10, no. 2, pp. 868–878, 2019. 109

[142] S. Song, Y. Kobayashi, and M. G. Fujie, "Monte-carlo simulation of light propagation considering characteristic of near-infrared led and evaluation on tissue phantom," *Procedia CIRP*, vol. 5, pp. 25–30, 2013. 109

[143] R. Van Veen, W. Verkruysse, and H. Sterenborg, "Diffuse-reflectance spectroscopy from 500 to 1060 nm by correction for inhomogeneously distributed absorbers," *Optics letters*, vol. 27, no. 4, pp. 246–248, 2002. 109

Bibliography